**Development of Analytical Systems for Detection of Biomarkers and Neurotoxic Exposure**

by

Lang Zhou

A dissertation submitted to the Graduate Faculty of
Auburn University
in partial fulfillment of the
requirements for the Degree of
Doctor of Philosophy

Auburn, Alabama
May 4, 2019

Keywords: Spectroelectrochemistry, Surface Plasmon Resonance, Fluorescence, Platelet-Derived Growth Factor, Tricresyl Phosphate



Approved by

Bryan Chin, Chair, Professor of Materials Engineering
Aleksandr Simonian, Co-chair, Professor of Materials Engineering
Dong-Joo Kim, Professor of Materials Engineering
Pengyu Chen, Assistant Professor of Materials Engineering
Christopher Easley, Professor of Chemistry and Biochemistry
Curtis Shannon, Professor of Chemistry and Biochemistry

Abstract

Exposure to the chemical and biological compounds in environment poses a serious health threat to humanity. Timely awareness of the chemicals in environment plays a vital role in exposure assessment, damage control, and diagnosis and treatment of diseases to minimized the harm caused by the ongoing exposure. The monitoring of these compounds can be achieved by in-situ environmental detection and biomonitoring- detection of biomarkers of exposure. To achieve biomarker detection in a more efficient and reliable fashion, a Multi-Parametric/ Multimodal apparatus System (MPMS) was developed in this study. MPMS combines electrochemical measurement, Surface Plasmon Resonance (SPR), and fluorescence spectroscopy into a SPR/fluorescence spectroelectrochemical technique. It enables not only quantitation of biomarker molecules with validation from the three signals, but also monitoring of the sensor's assembly process. In addition to its use in the development of biosensors, MPMS could potentially be applied in many other areas such as drug delivery systems, coatings for biomedical implants, electrochemical photocatalysis, electroluminescence, surface enhanced chemiluminescence, etc. This will allow unprecedented understanding for those functional interfaces of interest.

As an example, the unique capabilities of the MPMS system were utilized to develop the Electrochemical Proximity Assay (ECPA) of Platelet-Derived Growth Factor (PDGF). PDGF is a potential biomarker for the exposure to asbestos, and crystalline silica. PDGF is also an important latent biomarker in diagnosis and recognition of malignant diseases such as cancers,

glioblastomas and sarcomas. Therefore, the sensitive and reliable detection of PDGF has been attracting considerable attention. In this study, ECPA, a recently developed protein recognition strategy for point-of-care test, was employed for PDGF detection due to its high detection sensitivity and design flexibility. To demonstrate and testify the capabilities of MPMS, ECPA model system was tested first. As a result, MPMS achieved not only recognition of binding components involved in ECPA model system, estimation of their thicknesses and surface coverages, but more importantly, highly reliable in-situ monitoring of dynamic changes of components involved in interfacial binding via cross-validation and confirmation from three simultaneously generated signals- SPR, fluorescence and electrochemistry. In addition, the obtained corresponding proportions among magnitudes of three signals provide crucial information for future studies on simultaneous characterization of multiple components in one step, and differentiation of non-specific binding events. Another advantage using this technique is, the excitation of fluorescence is not only confined by surface plasmons, but by photons, so the fluorescence information can be also gained as the distance of fluorophores from the surface exceeds the decay length of surface plasmons. Subsequently, we studied the ECPA of PDGF using SPR/fluorescence spectroelectrochemical technique. It was found the cations present in the buffer solution play a key role in the hybridization efficiency, the aptamer-protein interaction and the background signals. As proper number of complimentary pairs, and proper buffer used, the electrochemical signals corresponded linearly to various concentrations of PDGF. In addition, MPMS has been proven able to characterize the process of proteins' covalent binding and layer-by-layer assembly in both sequential and simultaneous fashion.

Tricresyl phosphate (TCP) is a class of neurotoxic organophosphate cholinesterase inhibitors, exposure to which may induce nausea, vomiting, diarrhea and abdominal pain. Despite of its acute toxicity, TCP has been widely used in industrial applications, including flame retardants, and plasticizers. In many commercial jet oils, TCP is blended as an anti-wear additive, which could be released into the cabin air in the case of oil leakage of aircraft hydraulic systems. The TCP in cabin air could enter passenger's body through ingestion, inhalation of aerosols, and dermal sorption, and cause the symptoms above. To timely monitor the TCP leakage, an automatic TCP sampling system was coupled with an electrochemical flow injection analysis system. TCP was absorbed and hydrolyzed by an alkaline alumina column, and subsequently washed out of the column for direct electrochemical detection. After each detection, NaOH solution was used for column regeneration.

In spite of efficient hydrolysis of TCP through alkaline catalyst, the alkaline catalyst itself is consumed constantly during reaction, so continuous addition of alkaline catalyst is in demand for in-situ monitoring of TCP in environment. This not only introduces more chemicals to environment, but also increases the reagent and cost of detection. Furthermore, the resulted extremely basic solution leads to some limitation and difficulty for the detection system. To avoid mentioned problems, we explored on the development of reagentless catalyst for TCP's hydrolysis. $Ru(OH)_3$ and $Fe(OH)_3$ were proposed to be capable of catalyzing the alcoholysis and hydrolysis of TCP at room temperature.

Acknowledgments

I would like to express my deepest appreciation to my advisors, Prof. Aleksandr Simonian and Prof. Bryan Chin. Without their generous guidance and persistent support, I couldn't realize the achievements in my PhD program at Auburn University. They are not only my advisor in academic researches, but also mentors in my life. I cherish all advices and experiences they shared to me. Also, I would like to express my gratitude to my committee members, Prof. Pengyu Chen, Prof. Dong-Joo Kim and Prof. Christopher Easley for the suggestions provided on my research with their profundity of knowledge, my sincere gratitude to Prof. Curtis Shannon for being an external reader. In addition, I would love to especially thank Prof. Jacek Wower, Dr. Yuanyuan Zhang, Dr. Mary Arugula, I-Hsuan Chen, and Steven Moore for their generous help on my work.

Table of Contents

List of Tables

List of Figures

List of Abbreviations

| | |
|---|---|
| SPF | Surface Plasmon Fluorescence |
| SWV | Square Wave Voltammetry |
| MPMS | Multi-Parametric/ Multimodal apparatus System |
| TCP | Tricresyl Phosphate |
| ToCP | Tri-ortho-Cresyl Phosphate |
| PDGF | Platelet-Derived Growth Factor |
| IFN-γ | Interferon Gamma |
| HEPES | 4-(2-hydroxyethyl)-1-piperazineethanesulfonic acid |
| MCH | 6-Mercapto-1-hexanol |
| TCEP | Tris-(2-carboxyethyl) phosphine hydrochloride |
| ECPA | Electrochemical Proximity Assay |
| SPR | Surface plasmon resonance |
| BSA | Bull Serum Albumin |
| UV-Vis | Ultraviolet- Visible |
| GC-MS | Gas Chromatography-Mass Spectrometer |
| PBS | Phosphate buffer saline |
| LbL | Layer-by-Layer |
| MB-DNA | Methylene blue-conjugated DNA |
| Quasar-DNA | Quasar 705-conjugated DNA |

MB/Quasar-DNA Methylene blue/Quasar 705-conjugated DNA

Biotin-DNA Biotin-conjugated DNA

HPLC. High Performance Liquid Chromatography

SH-DNA Thiolated DNA

# 1. Introduction and literature review

According to the world health report (2003) of World Health Organization, each year 355,000 people worldwide are killed by unintentional poisonings. Majority of these deaths are strongly associated with excessive exposure to toxic chemicals. In many developing countries, toxic chemicals may be emitted directly from industrial processes, into air, water, soil without any treatment. According to International Labor Organization, these toxic chemicals mainly include the heavy metals, endocrine disrupting chemicals such as organophosphate insecticides, Persistent Organic Pollutants (POPs) and atmospheric pollutants such as oxides of sulphur, nitrogen[1]. Even worse, these toxic chemicals will be increasingly produced in near future. The Organisation for Economic Co-operation and Development has estimated that by the year 2020, the global output of chemical production will be 85% higher than that in 1995, and the chemical production will further shift to poor countries, increasing their related health and environmental risks[2].

Although it appears inevitable to be exposed to various toxic chemicals for individuals, unawareness of exposure aggravates the health risks for these chemicals, delays the damage control and treatment of diseases. The unawareness issue is extremely severe in developing countries. In spite of uses of only 25% of the world's pesticides, developing countries are responsible for 99% of the pesticides-associated deaths due to unawareness and regulation[3]. The exposure to toxic chemicals can be assessed by either monitoring the chemical sources in environment or measuring biological markers (Biomarkers) in human body. Therefore, we explored on system developments for both sides.

## 1.1 Neuroxin Tricresyl Phosphate

Tricresyl phosphate (TCP) is an ester of phosphoric acid and cresol. It has been used in industrial applications, including plasicizers, flame retardants and fluid additives. The commercial TCP products consist of a mixture of various cresyl isomers, in which tri-ortho-cresyl phosphate (ToCP) has been proved most neuroxic due to its irreversible damage to human's peripheral nerve and spinal cord[4], though the other isomers of non-ortho TCP has been found its role in inhibiting certain enzymes present in human beings[5]. According to AGCIH, the occupational exposure limit for ToCP is 0.1 mg/ $m^3$, based on an an 8h time-weighted average.

The peak limit of exposure is 0.3 mg/m$^3$ for 15 min. The World Health Organization stated in 1990 that a safe level of exposure to ToCP is not recommended because individuals have considerably variable sensitivity to ToCP[6].

In 1930, approximately 50,000 Americans was were paralyzed after consumption of Jamaica Ginger extract, due to the adulteration of ToCP. In 1959, over 10,000 people in morocco became paralyzed due to the adulterated ToCP in their cooking oil. Since 2002, the industry has dramatically reduced the production of ToCP. One exception is its use in engine oil, due to the excellent anti-wear property of TCP. In last decades, there are many reports that indicate potential connections between the exposure to TCP in cabin and cocktil air and symptom clusters of the crew[7]. Their exposure to ToCP is likely to result from the engine oil leakage. In the bleed air system of an aircraft, compressed heated air is cooled down as the source of cabin air. The bleed air was sent into the cabin for circulation. Engine seals function as a separator for the engine oil and bleed air. As aging, stressing or wearing happens, the engine seals are not sufficiently effecient, leading the leakage of the engine oil out of the compressor, thus entering the bleed air. In commercial engine oil products, 3% TCP was blended as an anti-wear additive. As the oil leakage occurs, TCP enters the bleed air together with other components in engine oil.

Even though TCP is only likely to enter bleed air as engine oil leakage happens, there are reports disclosing that the incidents associated with the engine oil leakage occur frequently[7]. The actual incidence rates are speculated higher than the aviation industry admits. Many of previous reports have shown the presence of TCP and ToCP in cockpit and cabin air[8].

As one kind of organophosphate, TCP inhibits cholinesterases, and can induce a delayed neurodegenerative condition known as organophosphorous-induced delayed neuropathy (OPIDN). Acute exposure induces nausea, vomiting, diarrhea and abdominal pain followed by a long asymptomatic period of up to a month. Bilateral degeneration of sensory and motor functions follows acute toxic exposure, and the chance of recovering full motor coordination is poor. Therefore, it is urgent to develop a simple, fast and accurate method for the measurement of TCP in gas.

TCPs are chemically inert, therefore, for the chemical reaction based measurement, it requires the decomposition by breakdown of its ester bonds within, and generation of chemically active molecules, cresols. This process is achieved conventionaly by alcaline-catalyzed hydrolysis. To date, we have not found reports on other catalysts which can realise the same funtion on TCP. Therefore, we explored on the development of new catalysts for TCP's hydrolysis.

### 1.2 Detection of TCP

To date, the most widely used techniques for TCP quantitation are based on molecule separation. Albertine[9] et al. used ethanol to extract TCP from lubricating oil, which was separated by gas chromatograph and detected by dual flame photometric detector. A dynamic responses were obtained for 2.12–955 ppm of p-TCP. Elizabeth[9] et al. coupled gas chromatographic and mass spectrometry to detect more than 21 arylphosphate compounds in water. Mutsuga[10] et al. utilized high-performance liquid chromatography (HPLC) and UV detector for the detection of TCP in polyvinyl chloride articles. The limit of detection reached 50 micrograms/g in samples. Denola[11] et al. monitored TCP contamination of cockpit air. The TCP was sampled through sorbent tubes, and analysed by gas chromatography with a pulsed flame photometric detector.

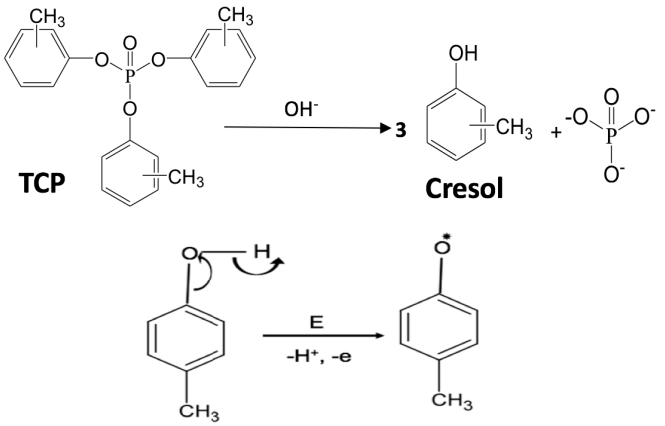


Figure 1.1 The principle of electrochemical detection of gaseous TCP

The methods mentioned above used instruments with bulky size and high cost, and requires highly-trained operators, thus are not suitable for the automatic real-time monitoring of gaseous TCP in aircraft. Even though miniature mass spectrometer has emerged[12,13], the commercially

available miniaturize mass spectroscopy detectors weigh approximately 30kg, and cost approximately $50,000[14], which is still heavy and expensive compared to many other analytical devices. In addition, ion mobility spectroscopy also has the capability of the detection of gaseous TCP with portability, high speed and simplicity, however, it has limitations on low ion separation efficiency, existance of false-positive results, and sample matrix effects[15,16]. Furthermore, its instrumental cost is not comparable to many other analytical methods, even though lower than mass spectroscopy based methods.

Electrochemical detection can avoid these drawbacks due to its features of ease of miniaturization, simple operation and low cost. TCP is electrochemically inert, while cresols are electrochemically active. Thus TCP needs to be hydrolysed via alkaline catalysts to yield cresol before electrochemically detected (Fig 1.1). Our TCP monitoring system consists of two units, TCP sampling system for its hydrolysis and flow injection system for electrochemical detection.

### 1.2 Functional interfaces

Funtional interfaces are heterogenous interfaces with certain functions such as molecular recognition, separation, and catalysis, signal transduction, computing and etc. The realization of these functions is mostly accociated with molecular interactions between abiotic surfaces and functional biomolecules such as proteins, DNA, aptamers, etc.

For instance, the specific recognition of target biomolecules can take advantage of the high affinity between target biomolecules with their antibodies or aptamers. In real-time monitoring or reusable biosensing, the kinetics and thermodynamics of the binding process on the functional interfaces are critical. They not only determines the sensitivity and detection time of sensors, but also the efficiency of sensor regeneration, such as how fast the bioreceptor molecules can transform to its original conformation and orientation, and what fraction of them can achieve this transformation. Furthermore, the assembly of the functional interface requires proper allocation, orientation, and conformation of individual biomolecular recognition elements, to achieve optimal activity, binding affinity and long-term stability.

Therfore, understanding their interactions plays a vital role in development of functional biointerfaces. Studying molecular interactions on functional interfaces is challenging. Because the physical and chemical properties of molecules at the biointerfaces can be drastically different from those in the bulk due to the surface segregation of the low surface energy component. The complexity and heterogeneity of the molecules to be bound increase the diffuculty for the investigation. Meanwhile, the molecular immobilization on the solid substrate and weak affinities renders additional risk of altering the binding dynamics. With growing interest in functional interfaces, it has become increasingly important to test these characteristics, and define chemical structures, topology, spatial distributions and orientation of functional structures on the surface in a quantitative manner.

### 1.3 Characterization techniques for functional interfaces

The development of advanced analytical techniques to study the interfacial properties and to characterize the biomolecular interactions has been the focus of high priority research for many decades. X-ray photoelectron spectroscopy, Auger electron spectroscopy, scanning electron microscope, etc. are routinely used to characterize the structural and functional features of the interactions and allocation to the surface. The development of advanced analytical techniques to study the interfacial properties and to characterize the biomolecular interactions has been the focus of high priority research for many decades. X-ray photoelectron spectroscopy[17–22], Auger electron spectroscopy[23,24], scanning electron microscope[25,26], etc. are routinely used to characterize the structural and functional features of the interactions and allocation to the surface[27]. Advanced spectroelectrochemical approaches to study the interfacial properties has been receiving increasing attention over the past decades. Spectroelectrochemistry can realize in-situ interface characterization via combination of electrochemistry and optical techniques. Electrochemical methods alone are often not suitable to recognize the binding events occurring on the interface and conformation changes, therefore an additional optical technique such as Surface Plasmon Resonance (SPR) is required.

### 1.4 Suface Plasmon Resonance

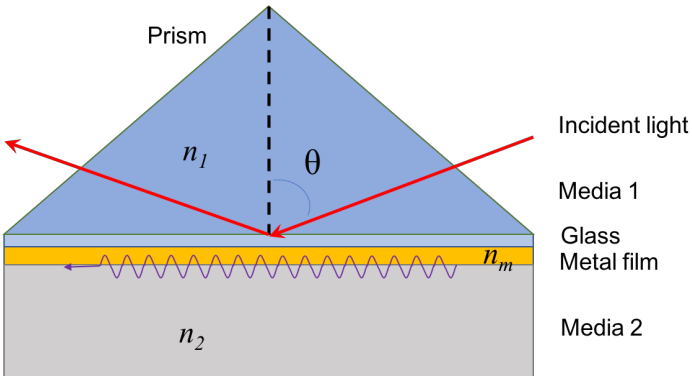


Figure 1.2 The principle of Surface Plasmon Resonance

As light transfers from a higher refractive index medium (1) to a lower refractive index medium(2), the refractive angle is higher than the incident angle θ. As θ surpasses the critical angle $\theta_c = sin^{-1}(n_2/n_1)$, the total internal reflection occurs. $n_1$ is the refractive angle of media (1), $n_2$ is the refractive angle of media (2). Meanwhile, there are evanescent waves generated on the interface of mediums. The evanescent waves travels in parallel with the interface and the amplitude of evanescent waves exponentially decay along the y direction. The decay length is $\lambda (sin^2\theta - n_2^2/n_1^2)^{-1/2} / 4\pi n_1$. Since the wave vector in x direction does not change in the interface, its magnitude $k_x$ can be described as

$$k_x = \omega \, sin(\theta) \, n_1 / c$$

where θ is the incident angle, ω is the angular frequency of incident light, c is the speed of light . The free electron gas on metal boundary can perform coherent oscillations confined at the metal-dielectric boundary. This is called surface plasmons, a surface electromagnetic wave. The wave vector of surface plasmons ($k_{SP}$) is determined by the dielectric constants of the dielectric medium and the metal film.

$$k_{SP} = \omega \, (n_2^2 n_m^2 / n_2^2 + n_m^2)^{-1/2} / c$$

where $n_m$ is the refractive index of the metal film.

The excitation of surface plasmon can be performed by the evanescent wave. This generation of surface plasmon through the evanescent wave is called surface plasmon resonance(SPR). This resonance results in the absorption of the incident light, and the sharply reduced intensity of reflected light. The condition to make this happen is that, $k_{SP}$ is consistent with $k_{x.}$ Therefore, the condition of surface plasmon resonance meets:

$$sin(\theta)\ n_1=(n_2^2 n_m^2/\ n_2^2+n_m^2)^{\ -1/2}$$

The angle of incident light which meets this condition is called SPR angle($\theta_{SPR}$), $\theta_{SPR}= sin^{-1}[(n_2^2 n_m^2/\ n_2^2+n_m^2)^{\ -1/2}/\ n_1)]$. Since $n_1$ and $n_m$ are constant. The $\theta_{SPR}$ only shifts with the change of the refractive index of media(2).

To obtain the information about molecule interactions, one type of the molecules are attached to the metal surface first. The other type of molecules are then introduced to the interface. As their interactions occur, the surface molecular density increases, the refractive index of media(2) increases as well. Thus the $\theta_{SPR}$ increases accordingly.

Surface plasmon resonance sensors take advantage of the exponentially decaying electromagnetic field at the boundary between two media to explore the change of refractive index occurring in the environment. The information of changes are contained in the toal internal reflection light. Under total internal reflection conditions, the decay length of the evanescent field is the same magnitude of the used wavelength of excitation light. For visible light, this decay length reaches within several hundred nanometers. Therefore, the changes of total internal reflection light are capable of measuring the analytes in the evanescent region. The well-known formats of the waves include waveguides, fiber-optics and surface plasmon resonance devices.

SPR, as a label free technique, is advantageous in studying the binding interactions on interfaces[28–32]. However, it has limitation on sensitivity and recognition of non-specific binding[33–36]. The coupling of SPR with electrochemistry can often improve this issue. In this way, these two techniques are able to compensate for each other. Pishko[37] et al. used a combination of electrochemistry and SPR to describe structural changes in the enzyme containing nanocomposite films on a gold surface. Simonian[38] et al. characterized

electrostatically assembled nanocomposite thin films containing redox polymers and oxidoreductases using SPR and electrochemistry. Zhang[39] et al. used SPR and amperometry for the renewal assembly and characterization of enzymatic layers at Layer-by-layer self-assembled biosensor interfaces. In spite of these well-demonstrated capabilities due to this combination, the difficulty in simultaneously tracking multicomponent dynamic events at interfaces, and identifying unknown species formed as intermediates or products, impedes its applications on interface characterization.

Label free techniques such as surface plasmon resonance (SPR) are advantageous in studying the binding interactions[28–32]. However due to high complexity, such investigations often require additional validations via fluorescence labeling techniques and/or electrochemical measurements[33–36]. Usually no single technique provides sufficient information and often only a combination of different techniques can allow real time monitoring of biomolecular interactions, their allocation and orientation on different interfaces.

### 1.5 Fluorescence and Surface Plasmon Fluorescence (SPF)

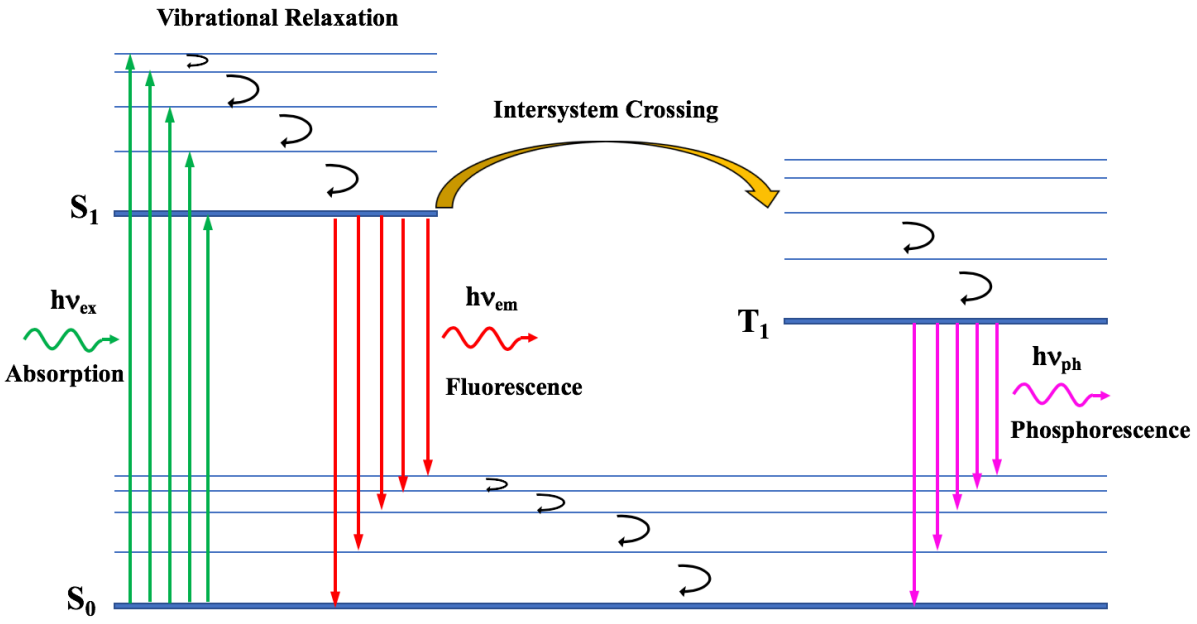


Figure 1.3 The principle of fluorescence and phosphorescence

Fluorescence is the emission of photons from molecules that undergo a transition from an electronically excited state to the ground state (Fig. 1.3). The occurrence of fluorescence experiences three spontaneous process, including excitation, excited-state lifetime and fluorescence emission. Fluorophores absorb photons with energy of $h\nu_{ex}$, upon which the ground state ($S_0$) of fluorophore molecule is excited to one of the vibrational levels of singlet excited state (states of $S_1$ and above).Within typically 1 to 10 nanoseconds, the fluorophore molecule maintains the excited state, and experiences conformational changes and interfaction with the environment. The result is the enegy dissipation through vibrational relaxation and the yield of a relaxed singlet excited state ($S_1$). The $S_1$ state finally returns to its its ground state through radiative relaxation, which is called fluorescence. The $S_1$ state can also be transformed to an excited triplet state ($T_1$) via intersystem crossing. In this case,$T_1$ achieves its radiative relaxation in the format of phosphorescence, making the molecule back to its ground state.

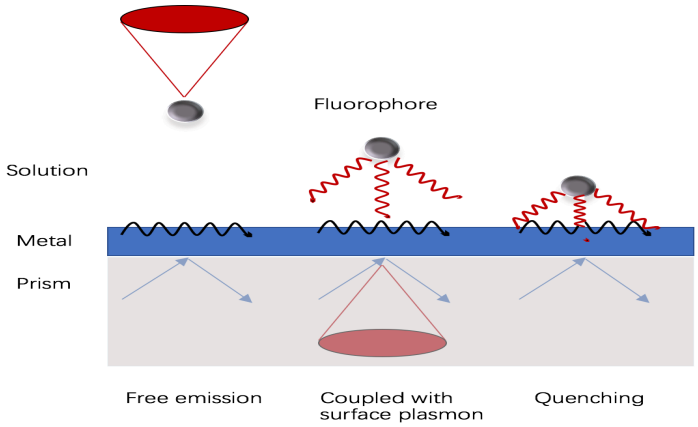


Figure 1.4 The effect of surface distance on the emission of SPF

Fluorescence has been widely applied in biological and medical researches owing to its high signal to noise ratio, high sensitivity, rapid time response as short as in the magnitude of nanosecond. One of core issues in the study of biosensors is how to improve the sensitivity for the detection of biomolecules. To achieve further improvement of fluorescence sensitivity up to the level of single molecule, a combination of fluorescence spectroscopy and SPR is necessary. SPR couples with the excitation and emission processs of fluorescence, and yields an enhancement of fluorescence intensity through the enhancement of the local electromagnetic environment. In addition, the effect of fluorescence bleaching could be reduced contributed to

the decreased lifetime of fluorophore molecules[40]. Depending on the properties of the metal and its nanoparticle, the enhancement factors from surface enhanced fluorescence differ case by case. The fluorescence obtained through the excitation of SPR is defined as Surface Plamon Fluorescence (SPF). The intensity of SPF has strong dependence on the metal-fluorophore distance as shown in Fig. 1.4[41].

In the vicinity of metals, there are interactions between the fluorophore with the metals. The evanescent field created by surface plasmon resonance can act as an excitation source of the fluorophore close to the surface. A prerequisite of this excitation is that, the fluorophores should be placed within the decay length of the evanescent field, a typical distance of which is several tens to hundreds of nanometers.

At a distance within 10 nm to the metal surface, the fluorophore is likely to dissipate the energy difference between $S_1$ and $S_0$ in the form of non-radiative decay[42,43]. Metals can also act as the media of energy transfer. The excited state of the fluorophore couples to the bands of electronic states in metal and relaxes by essentially heating up the metal slightly. At an intermediate-distance regime (~20 nm), a portion of excited photons couples with surface plasmon polaritons of metals, as their momentum matches. Subsequently, A fraction of the energy in surface plasmon polaritons will be transformed again into photons, and detected as surface plasmon fluorescence[41]. At longer separation distances (>20 nm), the energy transfer and polariton coupling are negligible, thus the fluorophore is excited by surface plasmon resonance and then has a free emission. However, as the separation distance surpasses the decay length of evanescent field, the excitation is weakened, reducing the fluorescence intensity.

The Knoll group developed surface plasmon fluorescence spectroscopy to investigate the binding of fluorescently-doped latex particles, biotinylated chromophore[41] and PCR product analysis[44], then further utilized the combination of SPR with fluorescence microscopy and spectrometry for detection of conjugated quantum dots[45]. Yokota [46] et al. investigated the real time imaging of single fluorophore-labeled protein using SPR excited fluorescence microscopy. Many efforts have been made to develop plasmonic structures which enhanced the fluorescence intensity[47], such as flat continuous films[48,49], periodically corrugated continuous films[50–52], metallic islands and nanoclusters[53–55], and nanoparticles[56–60]. For biosensing purpose, it has been

applied to detections of DNA[60–63], biomarkers[64–66],and toxins[67]. Most of these works used SPR only for the excitation of fluorescence. The SPR signal itself was not recorded or employed for the characterization of target molecules. Besides, most of the cases have been limited to or confined to the detection of one analyte-ligand binding event[68,69].

### 1.6 Combination of SPR and electrochemical spectroscopy

The combination of SPR, and electrochemical spectroscopy has been used for different characterizations. Pishko[37] et al. used a combination of electrochemistry and SPR to describe structural changes in the enzyme containing nanocomposite films on a gold surface. Simonian[38] et al. characterized electro-statically assembled nanocomposite thin films containing redox polymers and oxidoreductases using SPR and electrochemistry. Liu[70] et.al reported the simultaneous amplified SPR and electrochemical detection for biotin-labeled target DNA. Balasubramanian[71] et al. studied rational modulation of biological interfaces and the molecular assembly/disassembly processes using electrochemical desorption of surface-bound proteins and SPR. Vandenryt[72] et.al reported the integration of impedance spectroscopy and SPR for the detection of surface interactions. Zhang[39] et al. used SPR and amperometry for the renewal assembly and characterization of enzymatic layers at LbL self-assembled biosensor interfaces.

### 1.7 Combination of SPR, fluorescence and electrochemical spectroscopy

Having seen the benefits of combining two techniques above, we attempt to further push the boundary of this combination, to estabilish a system coupling these three techniques together. l The advantages of simultaneous collection from SPR, fluorescence and electrochemical spectroscopy include increased data reliability by triple validations from three signals, recognition of certain non-specific binding, capability on analysis of every single component of multicomponent complex process, potentially improved photon emission efficiency by dual excitation of SPR and electrochemistry. In addition, this multimodal system enables unprecedented studies in many other areas such as electrochemical photocatalysis, electroluminescence, surface enhanced chemiluminescence, etc. Therefore, the first major goal of this study is to develope a a Multi-Parametric/ Multimodal apparatus System (MPMS) which

integrates electrochemical measurement, SPR, and fluorescence spectroscopy into a SPR/fluorescence spectroelectrochemical technique.

### 1.8 Biomarker: Platelet-Derived Growth Factor (PDGF)

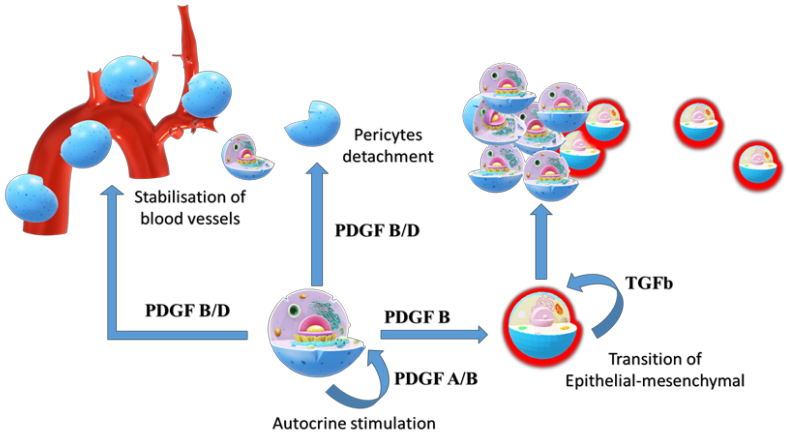


Figure 1.5 Schematics of PDGF's role in diseases[2]

Platelet-Derived Growth Factor (PDGF) is one type of growth factor that regulate cell growth and division. It is a dimeric glycoprotein that consists of two subunits of A, B, C or D isoform. PDGF-BB has also been directly implicated in malignant diseases such as cancers, glioblastomas and sarcomas, vascular disorders, such as atherosclerosis and restenosis, and fibrotic diseases such as liver fibrosis. Therefore, it has been recognized as a biomarker for the related diseases mentioned above. The PDGF-relevant cancers involved in PDGF signaling are likely to perform self-sufficient growth, angiogenesis, and metastasis[73]. PDGFs secreted by tumor cells could stimulate itself to grow and transit from epithelial cell to mesenchymal cell (Fig.1). Tumor cell-derived PDGF-B and PDGF-D will likely induce the detachment of pericytes, thus further facilitate metastasis in the case of their excessive production. They also function to stabilize the formed blood vessels, to promote the metastasis. PDGFs are also involved in the recruitment of tumor fibroblasts, which in turn produce cell factors such as HGF, CXCL12, FGF2, and FGF7 to facilitate the tumor cells' proliferation and migration. At the same time, angiogenic factors such as Vascular Endothelial Growth Factor(VEGF) are produced by fibroblasts to promote tumor angiogenesis, CCL5 is secreted to promote metastasis.

Among the malignant diseases mentioned above, glioblastomas is strongly associated with the exposure to asbestos. The asbestos exposure has become the predomintant cause of approximately 80% of pleural mesothelioma cases. According to WHO, 125 million people worldwide are occupationally exposed to asbestos [74]. The asbestos exposure can cause asbestosis, pleural effusions, pleural plaques, pleuritis, and mesothelioma. It was estimated that globally 43,000 people die due to mesothelioma each year[75]. PDGF level in malignant mesothelioma were reported significantly higher than patients from both the healthy group and the asbestos-exposed group[76].

In addition, the crystalline silica exposure has also been found associated with the change of PDGF level. Silica exposure can cause silicosis, cardiovascular diseases, tuberculosis, malignancies, autoimmune diseases and renal disorders[77]. Recent reports indicated that more than 37.9 million workers worldwide are exposed to crystalline silica dust[74]. In silica-induced lung fibrosis, PDGF-B stimulates the fibroblast proliferation, increased collagen deposition, and increased the extent of lung fibrosis[78]. Exposure of human bronchial epithelial cells to crystalline silica resulted in significant release of PDGF-BB[79]. PDGF levels were found positively correlated with the progressive development and severity of silicosis[80]. Therefore, PDGF has potential to be used as a biomarker for the exposure to asbestos and crystalline silica.

### 1.9 Detection of PDGF-BB

To date, the standard method for the detection of PDGF-BB is still enzyme-linked immunosorbent assay (ELISA) due to its high sensitivity and specificity. However, ELISA requires expert users, and dedicated instrumentation. Its opeation is time-consuming and laborious. Therefore, researchers have been developing novel strategies for PDGF detection to overcome these obstacles. Table 1. shows the dynamic ranges and limits of detection in their methods, including colorimetry, chemiluminescence, fluorescence spectroscopy, surface enhanced raman spectroscopy (SERS), biolayer interferometry and electrochemistry. The limit of detection ranges from 2.9 fM to 1.1 nM.

Many researchers have reported the normal level of PDGF-BB in human sérum, and compared it with that of various diseases. In fulminant hepatic failure patients, serum levels of

PDGF-BB (2.05 ±1.57 μg/L) was lower than acute hepatitis patients and controls (4.52 ±2.42 μg/L and 8.51 ±5.50 μg/L)[81]. Patients with mild acute pancreatitis (4.0 ± 0.61 μg/L) and those

Table 1. Comparison of PDGF-BB assay from literatures

| Methodology | Detection Range | Limit of Detection | References |
|---|---|---|---|
| Colorimetry | 2~80 nM | 1.1 nM | [82] |
| Colorimetry | 0.2~8.1 nM | N/A | [83] |
| Colorimetry | 0.01~3.16 pM | 2.9 fM | [84] |
| Chemiluminescence | 0.06~6 nM | 60 pM | [85] |
| SERS | 0.001~0.05 nM | 0.5 pM | [86] |
| SERS | 1~10000 pM | 0.42 pM | [87] |
| Fluorescence | 0.8~2000 fM | N/A | [88] |
| Fluorescence | 50 pm~44 nM | 0.8 pM | [89] |
| Fluorescence | 0.167~1.167 nM | 167 pM | [90] |
| Biolayer interferometry | 0.02~40 nM | 3.2 pM | [91] |
| Electrochemistry | 0.1~1000 pM | 52 fM | [92] |
| Elctrochemistry | 0.0001–1 nM | 30 fM | [93] |
| Electrochemistry | 0.017~1660 nM | 8.3 pM | [94] |

with walled-off pancreatic necrosis (1.60 ± 0.31 μg/L) had significantly lower serum levels of PDGF-BB compared to healthy subjects (6.2 ± 0.76 μg/L), while chronic pancreatitis (12 ± 1.3 μg/L) was associated with higher serum levels of PDGF-BB (6.2 ± 0.76 μg/L)[95]. The serum levels of PDGF-BB in male children with autism (5.624 ± 1.65 μg/L) were significantly higher than those of normal control subjects (4.76 ± 1.52 μg/L)[96]. The PDGF levels of myelofibrosis patients (6.2 ± 2.0 μg/L in plasma; 7.8 μg/L ± 2.4 μg/L in urine) and essential thrombocythemia patients (5.5 ± 1.5 μg /L in plasma; 11.4 ± 2.2 μg /L in urine) signficantly surpassed the level in normal volunteers (0.6 to 2.3 μg/L in plasma and 1.4 to 3.3 μg/L in urine)[91].It is clear to see the average normal level of PDGF-BB in human serum ranges from 1.5 to 8.5 μg/L (60~340 pM).

### 1.10 Electrochemical Proximity Assay (ECPA)

Recently, electrochemical proximity assay (ECPA) was developed as a novel simple, sensitive and flexible strategy for protein quantitation[97–101]. Upon the binding of two probes to the protein target, the proximity effect approaches an electrochemically active label, methylene blue (MB) close to a gold electrode, generating an electrochemical signal. ECPA was shown to be capable of sensitive detection of insulin, thrombin and prostate specific antigen [97–99]. This method is extremely flexible and can be utilized on a wide variety of protein recognition, thus promising to be applicable in point-of-care protein quantitation. Since ECPA was only recently developed, there is a need to explore the mechanisms of action and dynamics of its sensor preparation and target recognition. In order to demonstrate the ability of MPMS on ECPA, a simplified ECPA experiment was performed in this study, i.e. instead of the complex composed of two probes and target protein, a single DNA strand was used as the bridge between Thiolated DNA (SH-DNA) and Methylene Blue/Quasar conjugated DNA (MB/Quasar-DNA).

Due to the advantages shown above, we attempted to explore on ECPA of proteins using our MPMS system, to further study its mechanism during sensor preparation and protein recognition. As a protein target, PDGF-BB is suitable for the ECPA study, because its dimeric structure allows a pair of its aptamers to bind with a single PDGF-BB molecule.

### 1.11 Interferon Gamma (IFN-γ)

Interferon-gamma (IFN-γ) is a significant cytokine that possesses antiviral, antiproliferative, differentiation inducing, and immuno-regulatory properties. The recognition of IFN-γ plays an important role in understanding the function of immune cells in the immune response. The current commercial methods for detection of IFN-γ is still ELISA. As a viable alternatives, aptamer-based detection strategies for IFN-γ provides higher robustness so the biosensors are tolerant for repeated regeneration while maintaining their properties well, and amenability to various chemical modifications and inclusion of surface binding or sensing moieties[102,103].

Revzin's group has developed an aptamer beacon for the detection of IFN-γ, which takes advantage of fluorescence resonance energy transfer (FRET)[103]. Compared to several reported strategies for the detection of IFN-γ, such as electrochemical, mechanical, piezoelectric measurement, FRET is more suitable to convert the aptamer into real-time optical biosensors. We applied this strategy on MPMS, in order to explore on its mechanism and visilize this real-time process.

Taking advantage of aptamer-based strategy and fluorescence detection, MPMS was used to characterize IFN-γ, by combination of SPR and surface plasmon fluorescence. The IFN-γ aptamer labeled with fluorophore Quasar 705 was first immobilized to gold sensor by streptavidin/avidin affinity. Subsequently, it hybridized with IFN-gamma aptamer labeled with quencher, and immobilized on gold surface. Owing to quenching effect, fluorescence intensity is expected relatively low. In the presence of IFN-γ, the probe interacted with IFN-gamma, and the aptamer dissociated from the surface. Lack of its quencher, the fluorophore on probe received recovery.

# 2. Development of multi-parametric/multimodal apparatus for interface characterization

## 2.1 Introduction

The setup of MPMS system is shown in Fig 2.1. The BioNavis SPR instrument is coupled with an external laser at the same angle position relative to the prism. At a specific angle, the light beams from both the built-in and external laser strike the gold sensor surface, generating SPR. Consequently, this excites the fluorophore on the surface to produce Surface Plasmon Fluorescence (SPF), while the light from the built-in laser is reflected into the SPR detector. The emitted photons are collected by a bifurcated fiber bundle. Another approach for the fluorescence detection is based upon photon excitation. This utilizes one leg of the bifurcated fiber bundle to transmit exciting light, and the other to collect photon excited fluorescence from the fluorophore on surface. For electrochemical measurements, the gold sensor functions as the working electrode, and is a part of a three-electrode system together with the coupled Ag/AgCl(s) wire as reference electrode and the platinum wire as counter electrode. All electrodes, the tubing, and the fiber bundle mentioned above are coupled into a 3D printed flowcell.

## 2.2 Part list

BioNavis SPR 210A-L (Tampere, Finland),
Self-made 3D-printed flow cell
660 nm fiber coupled laser (Optogear, Lombard, Illinois)
Ocean Optics SF2000 (Dunedin, Florida)
Andor Shamrock 193i spectrograph/ idus 420A CCD camera (Belfast, United Kingdom)
CH Instruments Model 700E series (Bee Cave, Texas)
Bifurcated fiber bundle (BF19Y2HS02, Thorlabs, Newton, New Jersey)
Φ900 μM optical fiber
Bridge optical fiber (FG200UCC, Ø 200μm, Thorlabs, Newton, New Jersey)
Ag/AgCl(s) wire (taken out from Basi MF-2052 Ag/AgCl feference electrode)

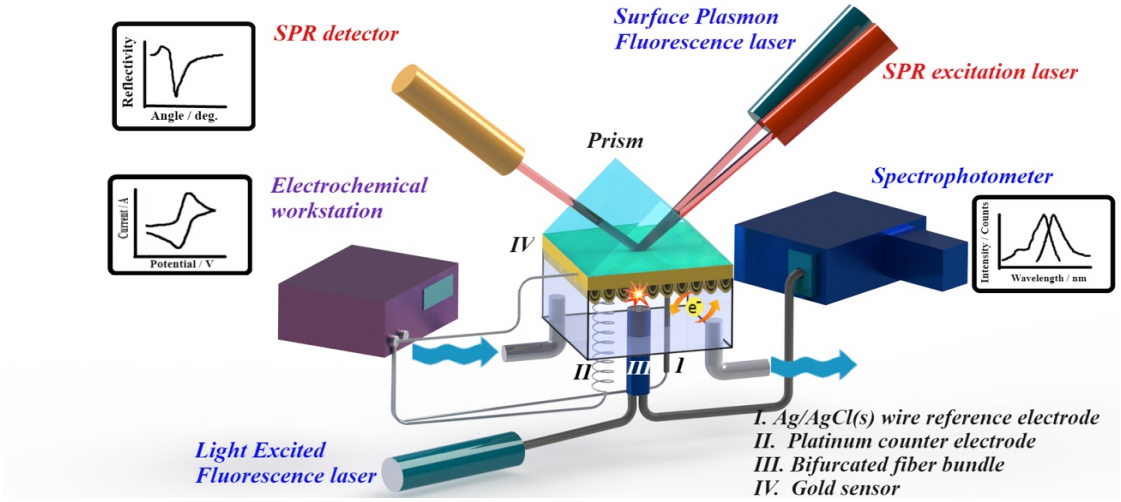


Figure 2.1 Schematic of Multi-Parametric and Multimodal Spectroscopy (MPMS) system.
It enables simultaneous and non-interfering measurements of SPR, three electrode electrochemical and fluorescence analysis on dye immobilized surfaces using a flowcell with external laser light source coupled directly to an independent spectrophotometer.

Pt wire(Ø 0.5mm, length 3cm)

Connector for working electrode (Bionavis, Tampere, Finland)

Customized gasket (Seal Group, Inc, Brookhaven, Mississippi, K11878, Compound:6375, size: 0.354*0.039 inches)

Tubing (PEEK Tubing Orange 1/32" OD x .020" ID, IDEX Health & Science LLC, Oak Harbor, Washington)

FC/PC to SMA mating sleeve (Thorlabs, Newton, New Jersey)

Peristaltic pump (Ismatec REGLO Digital 4-Ch 8-R Var-Speed Pump; 0.003 to 31 mL/min, 115V; Cole-Parmer LLC, Chicago, Illinois)

### 2.3 Manufacture and assembly of the flowcell

The body of flowcell (the purple part in Fig 2.1) was manufactured by 3D-printing. The design of the flow cell, with size of 1.22*1.07*0.56 inches is shown as Figure 2.2. The 3D printing is accomplished by Stratasys Ltd. using 3D printer Dimension Elite (Stratasys, Edina, Minnesota). The material used for printing is ULTEM 9085. As printing finished, the surface

treatment of epoxy coating and sealing was performed on the part. A gasket of 0.354*0.039 inches is customized to fit the size of groove in the flowcell. Dow Corning 3140 RTV Coating was used as an adhesive to fix the tubing (at the inlet and outlet), Ag/AgCl(s) wire, Pt wire, bifurcated fiber bundle and connector for working electrode.

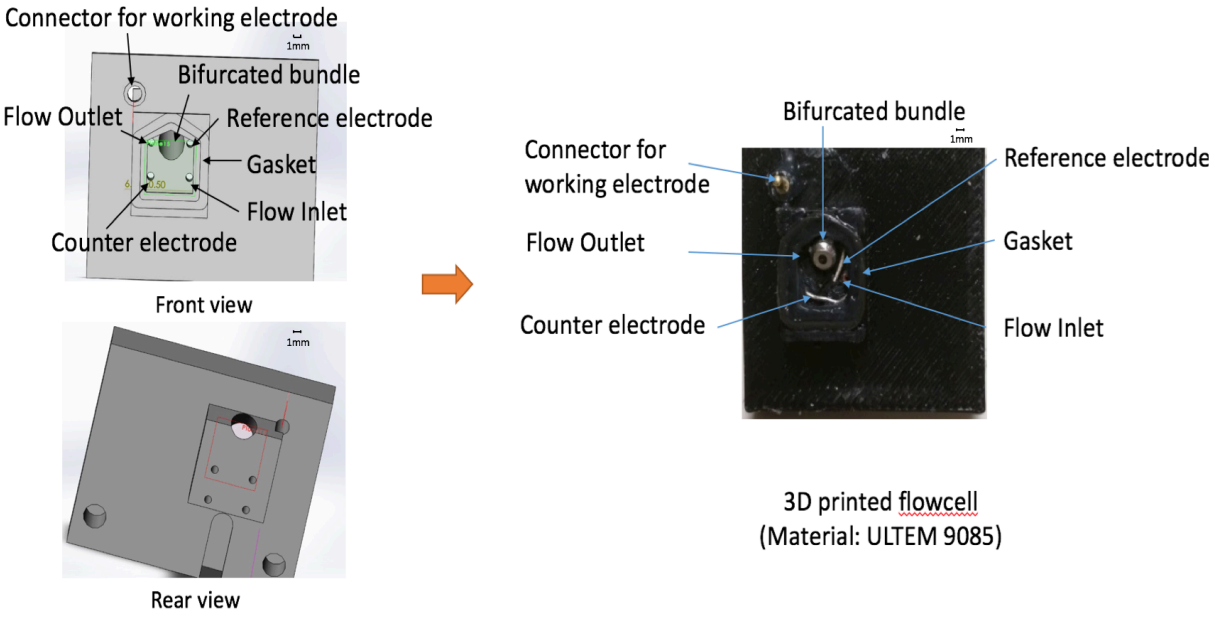


Figure 2.2. Design of the flowcell and its assembly with other parts

In the Fluorescence/SPR characterization, a different flowcell was used as shown in Fig 2.3. An optical fiber (Φ=900 μM) replaced the bifurcated fiber bundle to collect photon information. The other end of this fiber was linked to the Ocean Optics SF2000.

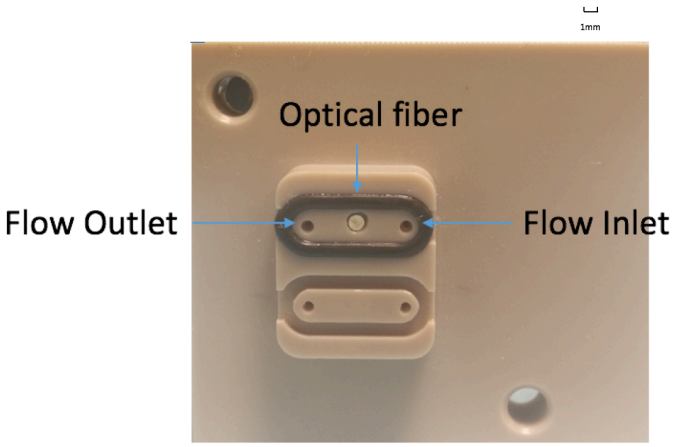


Figure 2.3 the configuration of SPR/SPF flowcell

## 2.4 Assembly of MPMS system

As shown in Fig.1, one leg of the bifurcated fiber bundle was connected to the FC/PC female adapter on the laser source via the bridge optical fiber, and a FC/PC to SMA mating sleeve. The other leg of the bifurcated fiber was connected to the SMA female adapter on Andor Shamrock 193i spectrograph. The Ag/AgCl(s) wire was connected to a reference electrode clip, Pt wire was connected to a counter electrode clip, the connector for working electrode was connected a working electrode clip, all of which were linked to CH Instruments Model 700E series for electrochemical measurement. The outlet tubing was connected with the Peristaltic pump, while the inlet tubing was connected with the sample solution.

## 2.5 Operation Parameter

Laser power: 5 or 60 mW in the parallel mode, 3.6 or 60 mW in the sequential mode

Fluorescence integration time: 10.22 s in the parallel mode, 3s in the sequential mode

High-speed Acquisition was used in simultaneous detection mode. Spectrum graph was used in sequential mode. Electric dark correction was performed in both modes to compensate for changes in baseline offset over time.

SPR angle resolution :1/4 second; scan mode: continuous; scan range in the parallel mode: SPR angle± 2.25° (66.75°~71.25°)

Square Wave Voltammetry potential range: -0.45V~0V; amplitude: 50 mV; frequency: 75 Hz; voltage increment: 0.001V

Flow rate: 30μL/min

# 3. SPR/SPF characterization of protein immobilization and interferon gamma aptamer-based detection

## 3.1 Introduction

Despite variety of detection methodologies documented in literature, understanding the adsorption formats for the detection of binding events between the biomolecules and the solid surfaces with ligands is a critical topic in fields of biomedical, sensing, food and environmental studies[104–106]. It also becomes increasingly important to characterize the chemical structures and biomolecules on surfaces in a quantitative fashion, and to test their proper allocation orientation, conformation, activities, and stability[107–109]. Surface Plasmon resonance (SPR) is a powerful tool that has been widely used, since the setup of BIAcore in the fields surface chemistry research and studies for monitoring the biological activity occurring on the surface. To enhance the applicability of SPR for multiple detection modules Knoll et.al combined the technique with fluorescence spectroscopy for detection of quantum dot conjugated[45]. Although several other reports have been published on surface plasmon enhanced fluorescence spectroscopy, most of the cases have been limited to or confined to the detection of one analyte-ligand binding event[68].

To demonstrate the capability of MPMS, we designed two different approaches based on layer by layer (LbL) and covalent binding techniques for immobilization of fluor dye labeled moieties to better understand the feasibility of integration of SPR and fluorescence. Our group has previously demonstrated LbL method for fabrication of electrochemical sensor electrodes and confirmed with SPR the stepwise assembly of the bionanostructures[39,110]. In this work, with external laser source combined into SPR instrument the resonant excitation of the evanescent field can be used to excite the fluorophore that have been immobilized on to the gold surface. We used two simple well-developed immobilization techniques LbL and covalent binding for detection of surface fluorophore and applied SPR and fluorescence detections strategies. Upon binding, the SPR should generate signal upon assembly of each step with simultaneous surface fluorescence signal only upon assembly of the labeled moiety. Based on BioNavis SPR Navi 200-L (Tampere, Finland), a novel flowcell coupled with optical fiber for fluorescence measurement was designed (shown in fig 3.1).

Interferon Gamma (IFN-γ) is a critical cytokine for human's immunity against viral, bacterial infections. Its overexpression is associated with autoinflammatory and autoimmune diseases. To improve the performance of biosensors for IFN-γ, aptamers have been applied to capture the target molecule, in which the signal was transduced by the emission of fluorescence from the fluorophore attached on the aptamers[111]. In the study, this sensing process was studied by simultaneous SPR and Surface Plasmon Fluorescence.

## 3.2 Materials and Methods

### 3.2.1 Materials

The reagents used in this research were: 4-(2-hydroxyethyl)-1-piperazineethanesulfonic acid (HEPES) (99.5%) was purchased from Alfa Aesar. Ammonium hydroxide (volumetric, standard 5.0N solution in water), Poly (ethyleneimine) solution (PEI, 50% (w/v) in water), Cysteamine (~95%), sodium phosphate dibasic (≥98.5%), glutaraldehyde(50% aqueous solution), N-(3-Dimethylaminopropyl)-Nlaminopropyl)-Nm Alfa Aesar. Ammonium hydroxide (volumetric, standard 5.0N solution in water), Poly (ethyleneimine) solution (PEI), was purchased from Fisher Scientific (Fari Lawn, NJ). Bovine serum albumin (BSA, lyophilized powder) was purchased from Hyclone (South Logan, UT). Tide Fluor is from AAT Bioquest (Sunnyvale, CA). Sodium perchlorate anhydrous (ACS, 98.0-102.0%) and Alcohol anhydrous (ACS, ≥99%) were purchased from VWR International (LLC Radnor, PA). IFN-γ is purchased from R&D Systems (Minneapolis, MN).

### 3.2.2 Instruments

Based on the commercial instrument SPR NAVI™ 200-L (Tampere, Finland), a new flow cell coupled with optic fiber with a diameter of 900μm was manufactured (Fig 3.1). Through the integration of the internal SPR light source and external laser, both light beams can strike at the surface of gold sensor creating surface plasmon resonance. The light beam from internal SPR light source is reflected into the SPR detector, generating the signal of reflectivity intensity, while the surface plasmon waves created by external laser resonantly excites the fluorophores.

Their emitted photons can be monitored by the fiber optics in the flowcell, and detected by Ocean Optics SF2000 fluorescence spectrophotometer.

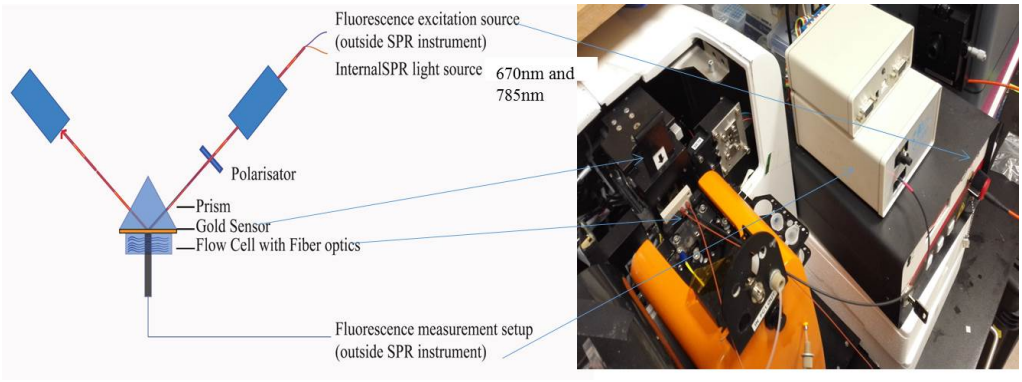


Figure 3.1 Schematic and experimental set up for MPMS

BioNavis SPR Navi 200-L (Tampere, Finland) was provided with modulated laser source at 785 nm and 670 nm and angular scan range between 38°-78.5°. The solution in the experiments was injected by external peristaltic pump, Ismatec® REGLO Digital 4-Ch Var-Speed Pump at flow rate of 30µL/min, and the flow cell was equipped with 1µL inner volume. A custom angle range was set at the range of 58° to 75° with angle resolution of 1/4 in a second, and scan interval times of around 16s. Optic gear laser device with wavelength 660nm was purchased from optic gear.

### 3.2.3 Preparation of SPR sensor slide

Gold slides (50nm) were purchased from BioNavis, Tampere, Finland and used in this study. After cleaning with the boiling solution composed of 1:1:5 hydrogen peroxide-ammonia-water for 10 min, the sensor slide was placed into the sensor holder and inserted into the instrument for detection.

### 3.2.4 Conjugation of BSA and Tide Fluor 6WS

BSA was conjugated with Tide Fluor 6WS by allowing 0.18mM BSA and 1.8mM Tide Fluor 6WS, 1.8mM EDC in 0.1M, pH4.7 MES buffer to react for 2h at room temperature. Figure 3.2 shows the schematics of the covalent binding of BSA tagged fluorophore onto the gold surface of the SPR sensor. The mixture was subjected to ultrafiltration with Amicon Ultracel-50K (Merck Millipore, Tullagreen, Germany) and further diluted with 10mM pH 7.5 HEPES buffer to obtain the final concentration of 0.9mM.

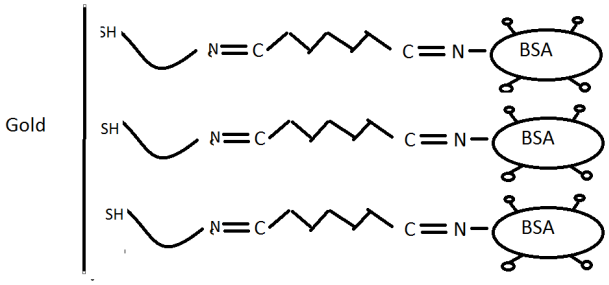


Figure 3.2 Schematic illustration of covalent binding of BSA tagged fluor

### 3.2.5 Assembly of oppositely charged species and dye immobilization by LbL approach

After the rinsing of sensor slide, the gold surface was negatively charged. Ten mg/L positively charged PEI dissolved in 0.1M pH 7.5 PBS and 0.9 mM negatively charged tide fluor 6-labeled BSA dissolved in 0.1M pH 7.5 PBS were injected alternately into the flowcell. The alternately charged species were allowed to bind in layer by layer fashion with buffer rinsing in between the injections to remove excess unbound materials.

### 3.2.6 Covalent immobilization of Tide Fluor 6-BSA

Cysteamine (1mM) was prepared and injected into the flowcell for thiol immobilization with surface amine groups. After stable signal was obtained 0.5% gluteraldehyde to that can act as cross linker was injected Finally 0.9mM Tide Fluor 6WS-labeled BSA solution were prepared and injected into the flowcell that can bind covalently to the cross linker. All the solutions above were prepared in 10mM HEPES (pH7.5)

### 3.2.7 Effect of incident angle on reflectivity and fluorescence

After the binding of Tide Fluor 6-BSA and washing process, the SPR scanning was conducted under the incident angles from 40° to 78.5°, from which the relationship between reflectivity and incident angle was obtained. Subsequently, the incident angle was set at certain angle between 40° to 78.5°, under which the surface fluorescence signal was collected with integration time of 1s.

### 3.2.8 Asynchronous and simultaneous detection of SPR and fluorescence

In asynchronous detection, the injection of solution was carried out with the monitoring of SPR response, i.e. the change of refractive angle. After the dye labeled component was bound to the surface, SPR measurement was stopped and fluorescence detection was initiated with integration time of 1s or 10s at certain incident angle (70 or 75°). In the simultaneous detection, the angle scan range was set between 69°-73.5° and the integration time for fluorescence measurement was set as 12.4s (which is measured as the time for experiencing a period of scanning).The obtained fluorescence intensity vs. time and reflectivity vs. time were plotted in one figure.

### 3.2.9 Measurement of IFN-γ

The sequence of IFN-γ aptamer is, 5'd Quasar 705-AGTAGCTTGGGGTTGGTTGT-GTTGGGTGTTGTGT -Biotin 3', the sequence of IFN-γ probe is, 5' d GATCTACTCC-AAGCTACCAGATC-BHQ-3 3' for its probe. IFN-γ aptamer and probe were reconstituted in IDTE buffer and diluted to desired concentration by Duplex buffer. 4 μg/ml Alexa-488 conjugated IFN-γ aptamer and 12 μg/ml probe attached with Iowa dark quencher were mixed at room temperature, heated to 95°C and then annealed at room temperature for 15min. The formed duplex was ready to challenge the gold surface. Prior to the assembly of the duplex, 0.25 mg/L streptavidin in DI water was pre-coated on sensors until the SPR signal reached saturation. Then the duplex solution was introduced into the sensor. 20min later, Duplex buffer was injected for 5min of washing. 1.2 mg/L IFN-γ was subsequently used to challenge the duplex-coated surface for 15min, prior to the washing using Duplex buffer. SPR signal was used to monitor this entire

process, while Surface Plasmon Fluorescence was compared before and after binding of IFN-γ solution.

### 3.3 Results and Discussion

#### 3.3.1 MPMS using covalent approach

Fig 3.3a demonstrated the covalent binding of the surface amine groups of cysteamine to gluteraldehyde cross linker and further binding the dye labeled BSA. Cysteamine, gluteraldehyde and dye labeled BSA displayed a net increase of refractive angle as high as 0.15°, 0.025° and 0.3° respectively. As the control group, the unlabeled BSA solution was used in the final step of binding, while the other procedure with dye labeled (experiment group). The result showed no difference of fluorescence intensity before and after the surface covalent binding of unlabeled BSA at the incident angle of 70°. Therefore the change in fluorescence intensity obtained was zero. On the other hand, in the experiment group shown Fig 3.3b, after injection of dye labeled DNA solution, the fluorescence exhibited a 650 counts increase of fluorescence intensity at the wavelength of 698nm, which is coincident with the emission spectrum of Tide Fluor 6.

This illustrates the ability of MPMS in qualitative demonstration of covalent binding. To confirm the mechanism of surface fluorescence obtained, the effect of incident angle on the reflectivity and fluorescence intensity was investigated as shown in Fig 3.3c. From the figure, it was obvious to see that the maximum fluorescence intensity appears at 70 degree, which is exactly the refractive angle in the surface plasmon resonance. This result proves that the fluorescence was predominantly excited by resonantly excited surface plasmon waves[68]. Because the dip in reflectivity indicates the angle at which the wavevector of the incident light matches that of the surface plasmon polariton of the metal. At this surface plasmon resonance angle, majority of the energy of the incident light is converted into surface plasmon excitation, leading significant enhancement of the electromagnetic field at the metal-fluorophore interface, and corresponding enhanced excitation of fluorophore and the maximum of fluorescence intensity. Fig 3.3d showed the simultaneous detection of SPR and surface fluorescence for this process. It could be observed from the SPR curve that, all the components are covalently bound to the surface alternately. The intensity after washing step resulted in 400 counts/s higher intensity than

before injection, which is a significant increase. This result proves the successful simultaneous detection of SPR and fluorescence, which gave nonbiased view of every stepwise of covalent binding and recognition of labeled fluorescence dye.

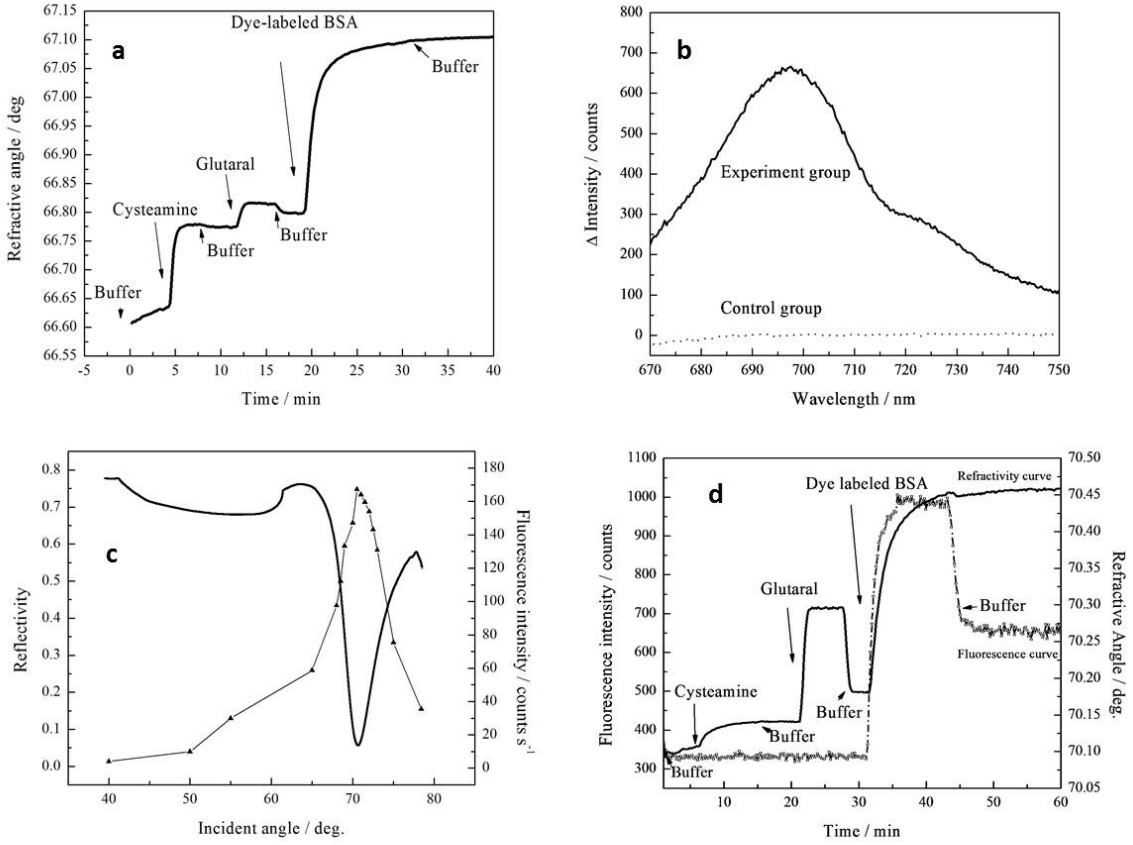


Figure 3.3 a) Dynamics of the stepwise formation of covalent binding by SPR b) emission spectrum of bound Tide Fluor 6 labeled BSA after subtraction of the emission spectrum of buffer c) the effect of incident angle on the reflectivity ( square ) and fluorescence intensity (triangle) d) simultaneous detection of SPR and fluorescence signal in the formation of covalent binding

### 3.3.2 MPMS using LbL assembly

In Fig 3.4a) the schematic of the process of layer-by-layer assembly was characterized. After rinsing with boiling solution comprised of hydrogen peroxide-ammonia-water, the gold surface attained negative charge, and the positively charged PEI and negatively charged dye-labeled BSA were deposited on the surface alternately. As shown in Fig 3.4b, the deposition of

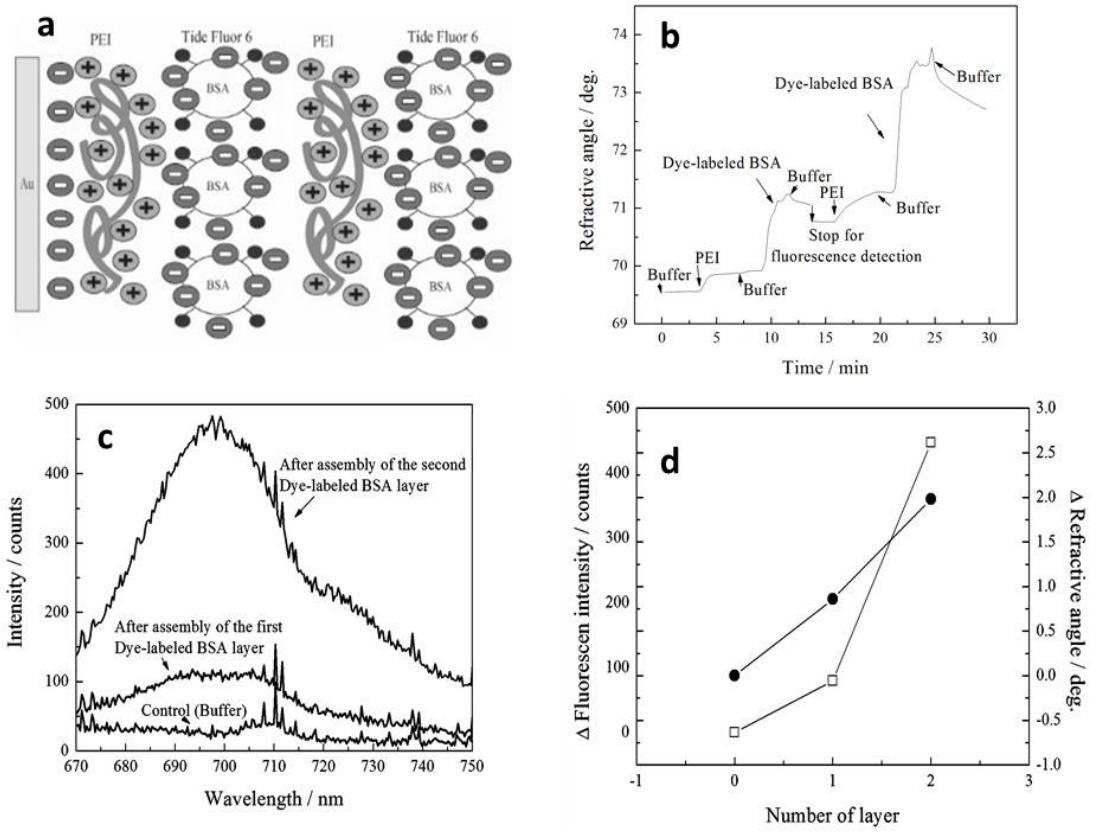


Figure 3.4 a) Schematic diagram of covalent binding b) Dynamics of the stepwise formation of layer-by-layer assembly by SPR c) emission spectrum in the formation of layer-by-layer assembly d) the effect of incident angle on the reflectivity and fluorescence intensity d) Change of refractive angle (circle) and fluorescence intensity (square) upon deposition of different layers

each step showed increase in refractive angle. The net refractive angle of the second layer of dye-labeled BSA increased twice compared to the first layer. While the fluorescence intensity showed the same trend but with intensity 4-5 times more than the first layer as show in Fig 3.4c~d. This might result from the uniform incident angle set in the experiment. The incident angle was chosen as 75° in this case. It was also observed that as the self-assembly was fabricated on the surface, the refractive angle changed significantly, unlike the small change in covalent approach, which explains the reason that led to observe lower fluorescence intensity value than its maximum which can be seen from the deviation of the data point (first layer)from its real value. However, we observed that the relative fluorescence intensity change coincides well with the refractive angle change obtained from SPR. To solve this problem, we will change

the incident angle according to the shift of refractive angle. In conclusion, with integration of SPR and fluorescence spectroscopy, MPMS system has proved able to characterize the dynamics of covalent binding and layer-by-layer assembly techniques. The asynchronous and simultaneous detection of SPR and fluorescence have been achieved. SPR signal gave a non-biased view of all steps of assembly, while fluorescence gave us the power to label and monitor specific portions. We anticipate that combining the SPR and fluorescence spectroscopy, the MPMS system will supply us the fundamental understanding of the dynamics in the formation of ECPA with an unprecedented level, which can overcome several key limitations of current, widely-used surface characterization technology. In future work, the detector for fluorescence measurement needs to be improved with higher sensitivity, and electrodes need to be coupled into the flowcell for electrochemical detection.

### 3.3.3 Detection of IFN-γ

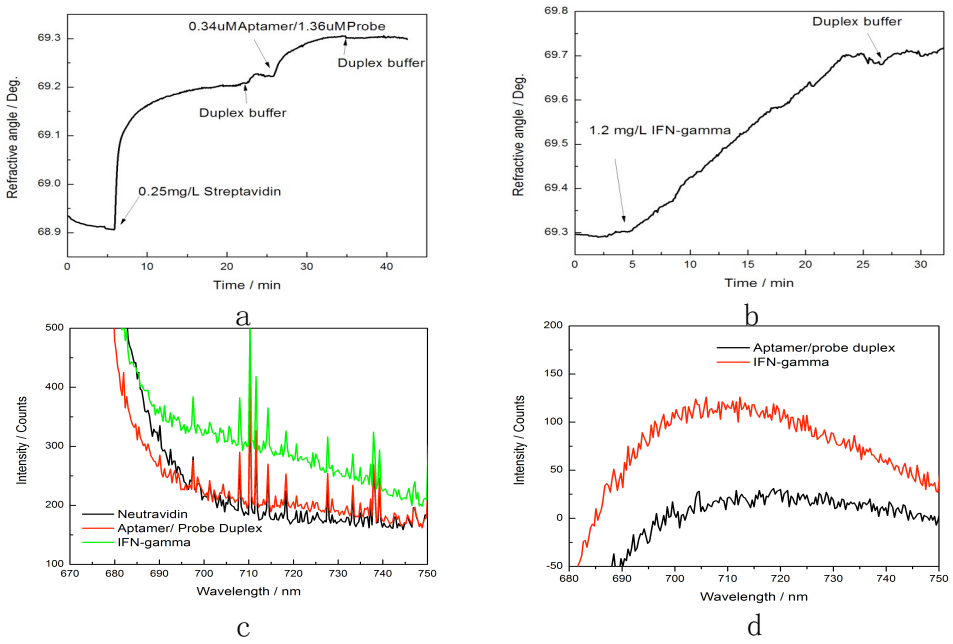


Figure 3.5 a) SPR response of the binding of Neutravidin and Aptamer/Probe duplex b) SPR response of the binding of IFN-γ c) fluorescence response d) emission spectrum after background subtraction

As the fluorophore attached aptamer and quencher attached probe were tethered on the sensor, a low fluorescence intensity was expected due to the quenching effect between the

labeled molecules. As introduction of IFN-γ solution, the conformation of aptamer was changed to bind IFN-γ, releasing the quencher attached probe at the same time. Without the quencher approached, the fluorophore attached aptamer had its fluorescence intensity recovered. The degree of recovery indicates the amount of IFN-γ in samples.

As shown in Fig 3.5a, the SPR result showed the increase due to each component, indicating the success of binding as well as the amount bound on surface. In particular, as IFN-γ was injected, probe molecule drifted away from surface while IFN-γ bound on surface. Because IFN-γ has a larger molecular weight, the overall SPR response is increase of SPR angle, indicating the growth of IFN-γ on sensor was linear(Fig 3.5b). The fluorescent signal showed that just as the expectation, the binding of IFN-γ recovered the fluorescence intensity as much as two times(Fig 3.5c~d).

The results above demonstrated the dual mode of SPR/SPF in MPMS enables characterizing covalent binding, layer-by-layer assembly in an asynchronous and simultaneous fashion. Using dual mode of SPR/SPF in MPMS, the sensing process of aptasensor of IFN-γ has been characterized. The fluorescence enhancement was accompanied by the increase of SPR angle, which validated the simultaneous occurrence protein/aptamer interaction and aptamer/probe dehybridization processes.

# 4. Simultaneous SPR/Fluorescence Spectroelectrochemical In-Situ Monitoring of Dynamic Changes on Functional Interfaces: A Study of Electrochemical Proximity Assay Model System

## 4.1 Introduction

Understanding the interactions existing between abiotic surfaces and functional biomolecules such as proteins, DNA, aptamers, etc. plays a vital role in development of functional biointerfaces for sensing, drug delivery, biomedical implants, antifouling layers, etc[112,113]. For example, the development of biosensors requires proper allocation, orientation, and conformation of individual biomolecular recognition elements, to achieve optimal activity, binding affinity and long-term stability[114–117]. However, studying interfaces is challenging because of the complexity and heterogeneity of the molecules to be bound, the immobilization/positioning method on the solid substrate and weaker affinities that render additional risk of altering the binding dynamics[118,119]. Advanced spectroelectrochemical approaches to study the interfacial properties has been receiving increasing attention over the past decades. Spectroelectrochemistry can realize in-situ interface characterization via combination of electrochemistry and optical techniques. Electrochemical methods alone are often not suitable to recognize the binding events occurring on the interface and conformation changes, therefore an additional optical technique such as surface Plasmon Resonance (SPR) is required. SPR, as a label free technique, is advantageous in studying the binding interactions on interfaces[28–32]. However, it has limitation on sensitivity, detection of small molecules and recognition of non-specific binding[33–36]. Additionally, due to the limit of evanescent field decay length, SPR is only sensitive to the refractive index changes within a distance of several hundred nanometers from gold surface. Electrochemical techniques have their advantages in simplicity, low cost, and miniaturized apparatus. However, for many biomolecules, there are no direct electron transfer happening at the electrode, so indirect electron transfer through label molecules is required, which increases the complexity and expense of detection. At the same time, the capacitive currents generated along with faradaic currents result in signal interference. Furthermore, electrochemical methods have difficulty in identifying unknown species formed as intermediates or products. The coupling of SPR with electrochemistry are often favorable for

their mutual compensation of these limitations. In spite of these well-demonstrated capabilities due to this combination, the demand for further improvement of sensitivity, and the difficulty in simultaneously tracking multicomponent dynamic events at interfaces, impedes its applications on interface characterization. To further enhance its ability in interface characterization, here we combined electrochemistry with two optical techniques- SPR and fluorescence. Fluorescence associated methods have been proven capable of reaching extraordinary sensitivity. Using different fluorescence labels, multi-components can be tracked simultaneously. To achieve sensitivity up to the level of single molecules, SPR was combined with fluorescence spectroscopy to stimulate the excitation of fluorophores and yield an enhancement of emission processes through the enhancement of the local electromagnetic environment. At the same time, the excitation of fluorescence via SPR reduces the effect of fluorescence bleaching due to the decreased lifetime of fluorophore molecules[40].

In spite of different combinations between SPR, electrochemistry and fluorescence for a variety of applications, the studies that have employed all three techniques in the same platform are rare. To the best of our knowledge, only one spectroelectrochemical system has been reported capable of recording all three signals by the Knoll's group[120,121].Nevertheless, it should be noted that not all of these three techniques were shown to be employed parallelly in their studies. The advantages of parallel signal collection of SPR, fluorescence and electrochemistry include increased data reliability by triple validations from three signals, recognition of certain non-specific binding, capability on analysis of every single component of multicomponent complex process, potentially improved photon emission efficiency by dual excitation of SPR and electrochemistry. In addition, this multimodal system enables unprecedented studies in many other areas such as electrochemical photocatalysis, electroluminescence, surface enhanced chemiluminescence, etc. For above reasons, we designed a Multi-Parametric/Multimodal Spectroscopy analytical system (MPMS), which couples SPR, fluorescence and electrochemical measurements based surface characterization spectroscopy into one analytical unit. A major difference of our system with the Knoll's is the usage of bifurcated optic fiber in the flow cell, which allows the detection of not only surface plasmon excited fluorescence, but also photon excited fluorescence. An important advantage doing so is, the fluorescence information can be

also gained as the distance of fluorophores from the surface exceeds the decay length of surface plasmons, which fails the excitation of fluorescence.

To test the performance and demonstrate the above mentioned, we studied electrochemical proximity assay (ECPA) model system as a proof of concept. ECPA is a recently developed strategy for protein quantitation of biomarkers such as thrombin and insulin[98,122]. Due to its simplicity, high sensitivity and flexibility, ECPA has great potential to replace the traditional enzyme-linked immunoabsorbent assay (ELISA), and be applicable in point-of-care protein quantitation. The principle is, the binding of two probes to their target protein brings an electrochemically active molecule, such as Methylene Blue, into close proximity with the electrode surface, which subsequently displays a proportional enhancement of current level to the amount of target protein. ECPA was shown to be capable of sensitive detection of insulin and thrombin. However, the only signal readout of ECPA occurs at the stage of MB binding, which means it is impossible to investigate directly the assembly process and the interactions between components. Using MPMS, this purpose could be well realized by synergistic usage of the three surface characterization techniques. In this work, the ECPA model system was studied to demonstrate SPR/Fluorescence spectroelectrochemical characterization capabilities. In ECPA model system, the complex formed by two probes and target protein in ECPA is replaced by a single DNA strand (DNA loop) as the bridge to form a loop structure (Fig. 2). ECPA model system simplifies the ECPA process via the saving of protein binding steps, thus allows an easier demonstration of MPMS achieved in both sequential and parallel manner, while it remains the main features of ECPA. Throughout simultaneous application of SPR, fluorescence and electrochemical detection, it was used not only to recognize binding components involved in ECPA model system, estimate their thicknesses and surface coverages, but also to comprehensively characterized real-time dynamic changes in interfacial binding and assemblies.

## 4.2 Experimental section

### 4.2.1 Reagents and Materials

Sodium perchlorate anhydrous (ACS, 98.0-102.0%) and Alcohol anhydrous (ACS, ≥99%) were purchased from VWR International (LLC Radnor, PA). 4-(2-hydroxyethyl)-1-

piperazineethanesulfonic acid (HEPES) (99.5%) was purchased from Alfa Aesar. 6-Mercapto-1-hexanol (MCH, ≥97%) was purchased from Santa Cruz Biotechnology (Dallas, Texas). Tris-(2-carboxyethyl) phosphine hydrochloride (TCEP) was from Sigma-Aldrich (St. Louis, MO). Methylene blue-conjugated DNA (MB-DNA), Quasar 705-conjugated DNA (Quasar-DNA), Methylene blue/Quasar 705-conjugated DNA (MB/Quasar-DNA), Biotin-conjugated DNA (Biotin-DNA) were purchased from Biosearch Technologies (Novato, California), and purified by HPLC. Thiolated DNA (SH-DNA) and DNA loop were purchased from Integrated DNA Technologies (Coralville, Iowa), and purified by HPLC. Sequences of DNA strands mentioned above are shown in Table 2 (listed 5' to 3'). Ultrapure water used in all experiments was purified by Millipore Direct-Q water purification system (resistivity >18 MΩ·cm-2).

### 4.2.2 Assembly of ECPA model system

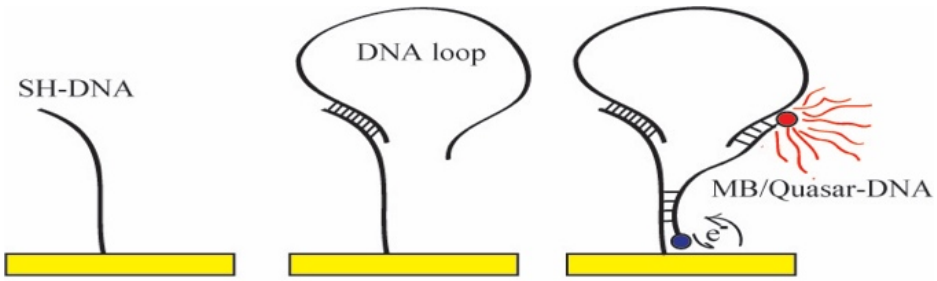


Figure 4.1 Schematics of the assembly of ECPA model system. DNA loop hybridizes with SH-DNA, which has formed a self-assembled monolayer on the gold surface. MB/Quasar-DNA tagged by methylene blue (blue) at 3' and Quasar 705 at 5' subsequently hybridizes with SH-DNA and DNA loop simultaneously, forming a loop structure.

A new gold sensor slide (50nm Au, BioNavis, Tampere, Finland) was cleaned for the initial use in boiling solution composed of 1:1:5 hydrogen peroxide-ammonia-water for 10 min,

**Table 2**. DNA sequences used for development of MPMS

| Name | DNA sequence, listed 5' to 3' |
|---|---|
| SH-DNA | ThioMC6-D/GCA TGG TAT TTT TCG TTC GTT AGG GTT CAA ATC CGC G |
| DNA Loop | TAG GAA AAG GAG GAG GGT GGC CCA CTT AAA CCT CAA TCC ACC CAC TTA AAC CTC<br>AAT CCA CGC GGA UUU GAA CCC UAA CG |
| MB-DNA | CCA CCC TCC TCC TTT TCC TAT CTC TCC CTC GTC ACC AUG C/ MB |
| Quasar-DNA | Quasar 705/CCA CCC TCC TCC TTT TCC TAT CTC TCC CTC GTC ACC AUG C |
| Biotin-DNA | CCA CCC TCC TCC TTT TCC TAT CTC TCC CTC GTC ACC AUG C/ Biotin |
| MB/Quasar-DNA | Quasar 705/CCA CCC TCC TCC TTT TCC TAT CTC TCC CTC GTC ACC AUG C/MB |
| Control sequence A | GAT CTA CTC CAA GCT ACC AGA TC |
| Control sequence B | TAC TCA GGG CAC TGC AAG CAA TTG TGG TCC CAA TGG GCT GAG TAT TTT TTT TTT TTT TTT TTT TTT TTT TTT TTT CGC GGA UUU GAA CCC UAA CG |

followed by another 10 min of sonication in water. For regeneration, the same sensor slide was cleaned by acidic piranha solution containing 30 ml 95~98% sulfuric acid and 10 ml 30% hydrogen peroxide for 5min, and 10 min of sonication in ultrapure water. Followed by the thorough cleaning of sensor surface, the sensor is placed into a sensor holder and inserted into the MPMS system for ECPA components assembly. 24 µL of 200 µM SH-DNA was mixed with 48 µL of 10 mM TCEP, and followed by 90 min of incubation in the dark at room temperature to reduce the disulfide bonds. The mixture was then diluted to a total volume of 800 µL by HEPES / $NaClO_4$ buffer (10mM HEPES, 0.5 M NaClO4, pH 7.5) with a final concentration of 6 µM. A loop structure was subsequently formed by sequential injection of 6 µM SH-DNA, 3 mM MCH, 0.5 µM DNA loop, and 0.1 µM labeled DNA (Fig. 4.1). The labeled DNA here represents

Quasar-DNA in fluorescence/SPR characterization, MB-DNA in SPR/electrochemical characterization, MB/Quasar-DNA in SPR/ fluorescence spectroelectrochemical characterization, and Biotin-DNA in the control experiment.

### 4.2.3 Fluorescence/SPR characterization

#### 4.2.3.1 Sequential characterization

A laser power of 60mW and integration time of 3s were used. After baseline stabilization with HEPES / $NaClO_4$ buffer, a sequential injection of SH-DNA, DNA loop, and Quasar-DNA in HEPES / $NaClO_4$ buffer with concentrations mentioned above were performed. The injection of each component was sustained until SPR angle reached constant. The HEPES / $NaClO_4$ buffer was subsequently injected for removing unbound molecules. The SPR curve shows the alteration of SPR angle as the response of stepwise molecular binding as shown in Fig.3a. The thickness and surface coverage of each component in ECPA model system was calculated using Eq. 1 as the method described previously[123,124]:

$$d = \left(\frac{l_d}{2}\right)\frac{(n_{eff} - n_b)}{(n_a - n_b)} \qquad \text{(Eq. 1)}$$

where d is the thickness of the measured component, the characteristic decay length ($l_d$) is 109nm[125], the difference between effective refractive index ($n_{eff}$) and refractive index of the buffer ($n_b$) are converted from the measured SPR angle by dividing the SPR angle shift by the sensitivity factor[125], 121.5 deg/RIU. The refractive index of DNA($n_a$)[126] is 1.46. The refractive index of the buffer($n_b$) is measured as 1.35. The surface coverage was obtained from the product of the thickness d calculated as above and density of DNA[127], 1.63 $g \cdot cm^{-3}$.

#### 4.2.3.2 Parallel characterization

SPF was excited at the laser power of 12.5 mW, the angle scan range was SPR angle± 2.25° (66.75°~71.25°) and the integration time for fluorescence measurement was 12.4s (which was equal to the time for one cycle of SPR angular scan). Other experimental conditions followed as mentioned in sequential mode.

### 4.2.4 SPR/Electrochemical characterization

Square Wave Voltammetry (SWV) was performed at different time point during the period of SPR measurement. The parameters used are potential range -0.45V~0V, amplitude 50 mV, frequency 75 Hz, and voltage increment of 0.001V.

### 4.2.5 SPR/ Fluorescence spectroelectrochemical characterization

#### 4.2.5.1 Sequential characterization

SPR, fluorescence and electrochemical signal were obtained in a sequential manner. SPR continuously monitored the binding event on gold surface. The angular mode was employed during SPR measurement. The scan range of angles was set between 58° and 75° with angle resolution of 1/4 second. The interval time of scan was approximately 16s. As SPR measurement was stopped, the incident light beam was set to the SPR angle determined by SPR measurement, the external laser was switched on at 60 mW, the spectrophotometer was launched to obtain the emission spectrum from 339 nm to 1022nm. The SPF was obtained at the integration time of 1s. Subsequently, fluorescence detection was initiated by connecting the external laser with one leg of the bifurcated fiber bundle. The laser power was 3.6 mW. The integration time of fluorescence was 3s. The electrochemical measurement followed the termination of laser irradiation. The electrochemical parameters followed the above procedure.

#### 4.2.5.2 Parallel characterization

SPF was excited at the laser power of 5 mW, the angle scan range and the integration time were the same as shown in Fluorescence/SPR characterization. The fiber optic spectrophotometer (SF2000, Ocean Optics) used in above was replaced by a spectrograph (Shamrock 193i, Andor) and a CCD camera (idus 420A, Andor). The conditions of SPR and electrochemical measurement followed the above.

## 4.3 Results and discussion

### 4.3.1 Fluorescence/SPR characterization

The combination of SPR and fluorescence, was utilized for the characterization of ECPA model system in both sequential and parallel manner. The sequential characterization is achieved by recognizing the output difference prior to and after the binding event, while the parallel mode records dynamic changes of signal to indicate the kinetics of binding molecules.

#### 4.3.1.1 Sequential characterization

The interface binding for SH-DNA, MCH, DNA loop and Quasar-DNA resulted in SPR angle increase as much as 0.15°, 0.06°, 0.08°, 0.08° (Fig 4.2a), successively, which indicated the formation of loop structure as expected. The thickness of SH-DNA, MCH, DNA loop and Quasar-DNA is estimated as 0.61, 0.24, 0.32, 0.33nm, the surface coverage of which is estimated as 96, 37, 50, 51ng·cm$^{-2}$ respectively, according to Eq.1. A remarkable gap observed in the curve shown in Fig.3a was due to the pause of SPR detection, and the launch of an emission scan for fluorescence detection. The fluorophore Quasar 705 attached to the DNA sequence displayed the maximum emission wavelength at 705nm (data not shown). As shown in Fig 4.2b, the emission peak was not detected until the Quasar-DNA was introduced and bound to the interface. Of note, in the middle of Quasar-DNA's binding event, the emission intensity reached 1492 counts; as the subsequent buffer washing finished, this value dropped to 629 counts. Since SPR angle showed no difference between these two steps, the decrease of SPF did not result from the dissociation of the bound molecules from the surface during buffer washing. Instead, this phenomenon demonstrates that not only bound fluorescence molecules but also the unbound molecules in the solution can be detected at the same time.

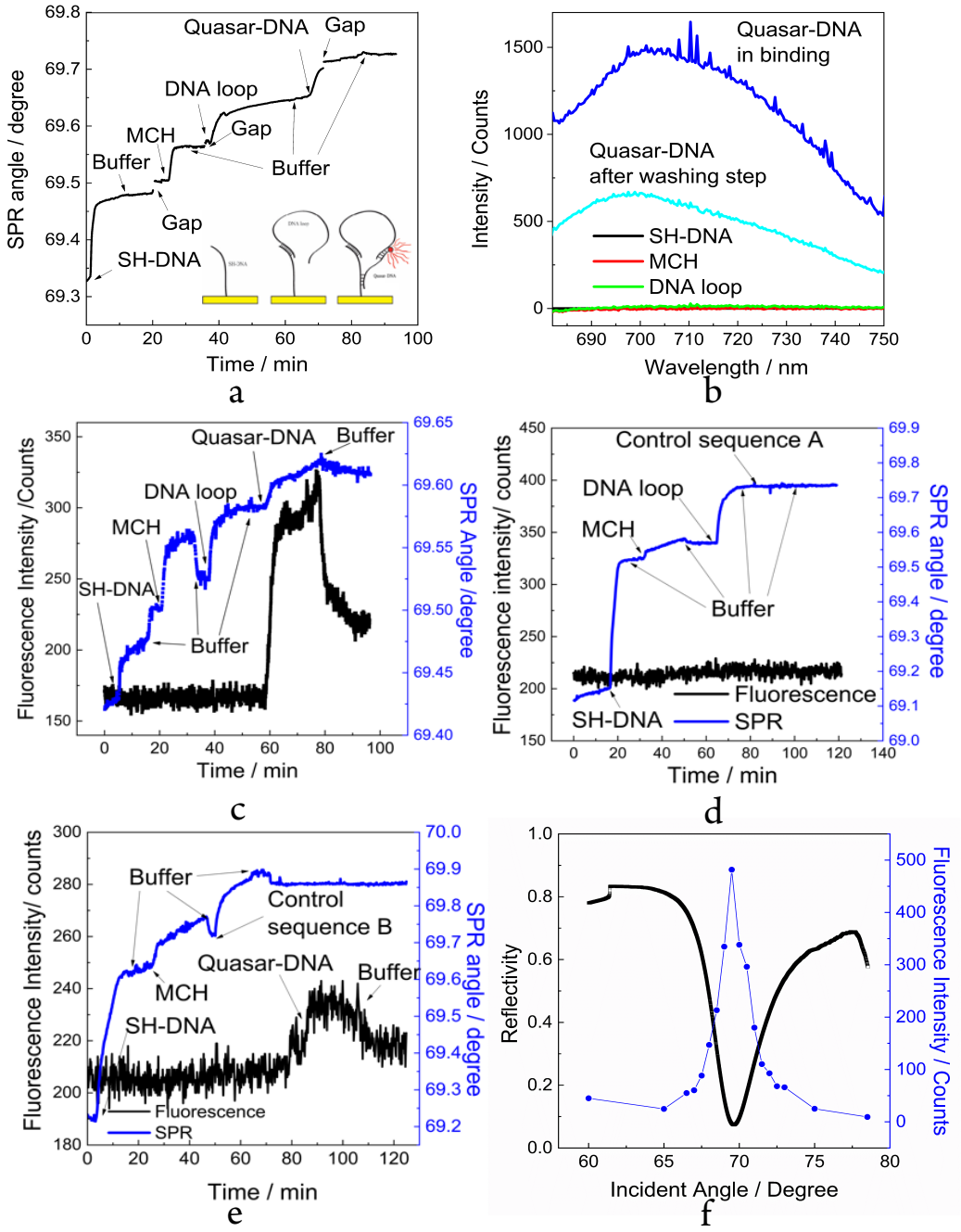


Figure 4.2 Fluorescence/SPR characterization of ECPA model system. a) SPR signal monitoring the assembly of each component b) SPF emission spectrum monitoring the binding behavior of only Quasar-DNA in the sequential mode. c) SPR/SPF simultaneously monitoring the dynamic changes of each component in the parallel mode (SPR response in blue, fluorescence response in black). d) SPR/SPF control test 1: Quasar-DNA was replaced by the control sequence A. e) SPR/SPF control test 2: DNA loop was replaced by the control sequence B. f) the change of SPR reflectivity and SPF intensity with the incident angle, investigated for the validation of fluorescence excitation mechanism.

#### 4.3.1.2 Parallel characterization

The kinetic curves from both signals are shown in Fig 4.2c. The fluorescence intensity and SPR angle synchronously change in response to the assembly of Quasar-DNA. The intensity of SPF at 705nm remained at the background level prior to the introduction of Quasar-DNA, and subsequently increased significantly after its introduction. According to both responses, the initial association rate for Quasar-DNA is 2.0 $ng \cdot cm^{-2} \cdot min^{-1}$, the fluorescence increasing rate is 4.5 $counts \cdot min^{-1}$. The subsequent buffer washing resulted in a significant intensity loss as much as 222 counts, approximately half of the total, while the SPR curve showed no significant decrease, namely, no disassociation of molecules occurred at the same time. This result further validated the observation of both bound and unbound fluorescence molecules. After buffer washing step, the fluorescence intensity is still 55 counts higher than that before the introduction of Quasar-DNA. The net increase of SPR angle, 0.03° corresponds to a surface coverage of 38.4 $ng \cdot cm^{-2}$ for Quasar-DNA. Meanwhile, since the sudden SPR angle drop resulted from the removal of Quasar-DNA solution, the ratio between bound and unbound Quasar-DNA was estimated as 4.75:1 within the distance range of evanescent field. As control, Quasar-DNA was replaced by a non-complementary DNA- control sequence A. As the control sequence A was introduced, both SPR angle and fluorescence intensity remained constant (Fig 4.2d), which indicated the specificity of the assay through its comparison to the last result. To further demonstrate the unbound Quasar-DNA could be detected in MPMS, another control experiment was conducted by replacing the DNA loop with a non-complementary DNA- control sequence B, and reducing the complementary bases on SH-DNA from 7(GCATGAA) to 5 (GCATG) for Quasar-DNA (to reduce the undesired interaction between SH-DNA and Quasar-DNA). This non-complementary DNA could hybridize with SH-DNA, yet not with Quasar-DNA. As 100 nM Quasar-DNA was introduced (Fig 4.2e) onto the control sequence B fabricated sensor, SPR angle did not display any shift while fluorescence increased 20 counts. As the subsequent buffer injection pushed the Quasar-DNA solution out of flowcell, the fluorescence intensity recovered to the level prior to Quasar-DNA injection. Therefore, the unbound fluorescence component is proven detectable in our MPMS system. In order to confirm the role of SPR in the excitation of SPF, the effect of incident angle on the fluorescence intensity was investigated as shown in Fig 4.2f. It is clear to find the direct relation between fluorescence intensity and incident angle. The

incident angle producing the maximum fluorescence intensity was coincident with its SPR angle (69.5°), which displayed the minimum reflectivity. This validated that the detected fluorescence was excited by SPR, instead of the photons.

### 4.3.2 SPR/Electrochemical characterization

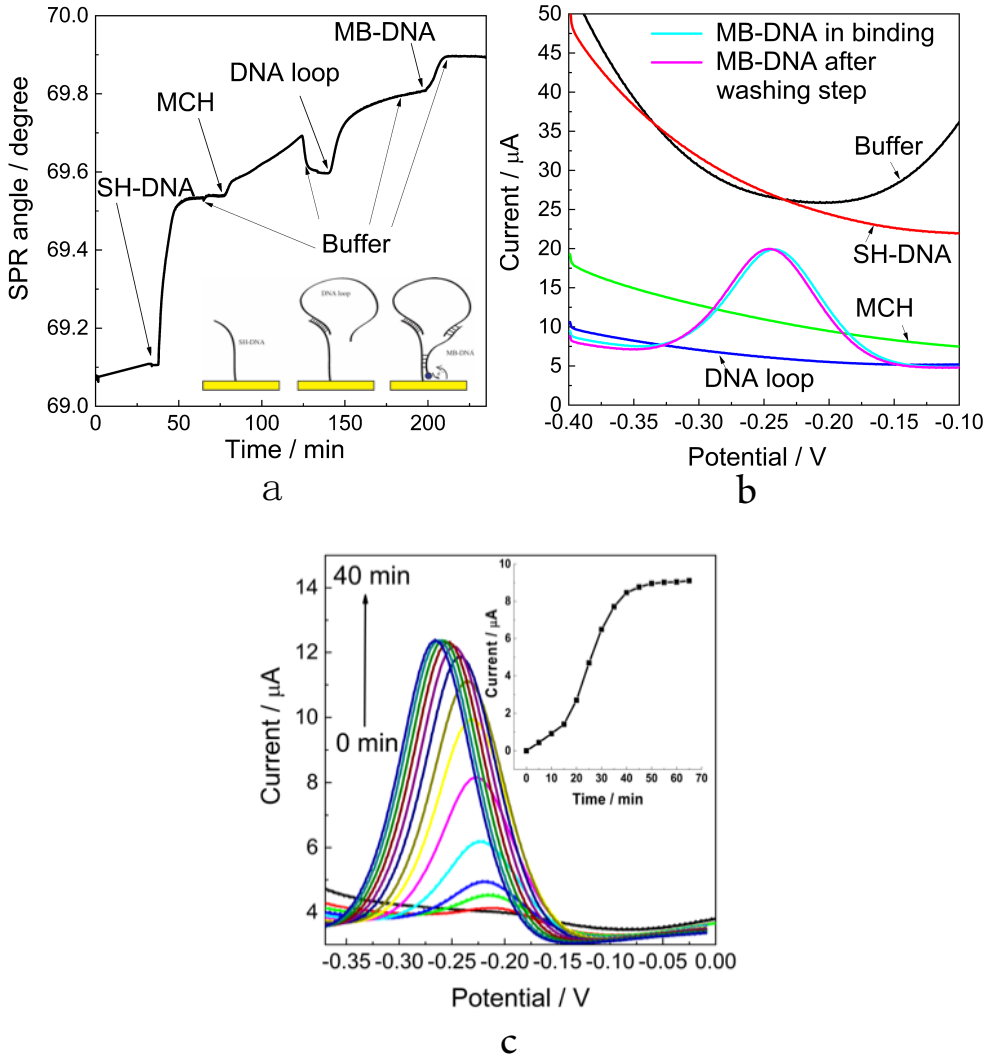


Figure 4.3 SPR/Electrochemical characterization of ECPA model system. a) SPR signal monitoring the assembly of each component. b) SWV spectrum showing the response of background current as the assembly of components and oxidation peak of MB due to the binding of MB-DNA. c) the dynamic changes of SWV spectrum in the process of MB-DNA binding

SPR and electrochemical measurement were applied parallelly to investigate the process of ECPA model system. Unlike what has been observed in SPR/Fluorescence characterization, each time of SWV scan resulted in a slight drop of SPR angle as small as 0.002~0.003 degree, which was subsequently recovered in the next minutes. As indicated in Fig 4.3a, the SPR angle increased 0.43°, 0.06°, 0.20°, 0.09° as SH-DNA, MCH, DNA loop and MB-DNA were introduced to the flow cell, successively, which indicated the thickness of 1.71, 0.23, 0.81, 0.37 nm, and the surface coverage of 279, 37, 133 and 61 ng·cm-2 respectively. The binding of SH-DNA, MCH, DNA loop resulted in the reduction of background current from 26.7 μA to 6.1 μA (Fig 4.3b). After 100 nmol/L MB-DNA was introduced, a sharp, well-defined peak was observed at -243 mV (vs. Ag/AgCl), which belongs to the oxidation peak of MB. The peak current significantly increased to 20 μA within 5 min, and completely remained stable via a 30s of buffer wash. In another experiment (Fig 4.3c), the same procedure was conducted, except the concentration of MB-DNA was reduced to 50 nmol /L from 100 nmol/L to observe the dynamic change of current peak. It is obvious to see the increase of net peak value from 0 to 9 μA as function of time in 50min. At the same time, the peak position shifted more negatively to around -260mV. This could be explained by the interaction mechanism between MB and nucleic acid varies between single- and double-stranded DNA[128,129]. MB peak obtained on double-stranded DNA modified electrode has more negative potential than that on single-stranded DNA modified electrode. Therefore, as more double-stranded DNAs formed during the assembly of MB/Quasar-DNA, the MB oxidation peak shifted more negatively.

### 4.3.3 SPR/Fluorescence spectroelectrochemical characterization

By integrating SPR, Fluorescence and Electrochemistry, the study for functional interface of ECPA model system can be also performed in a sequential and parallel fashion.

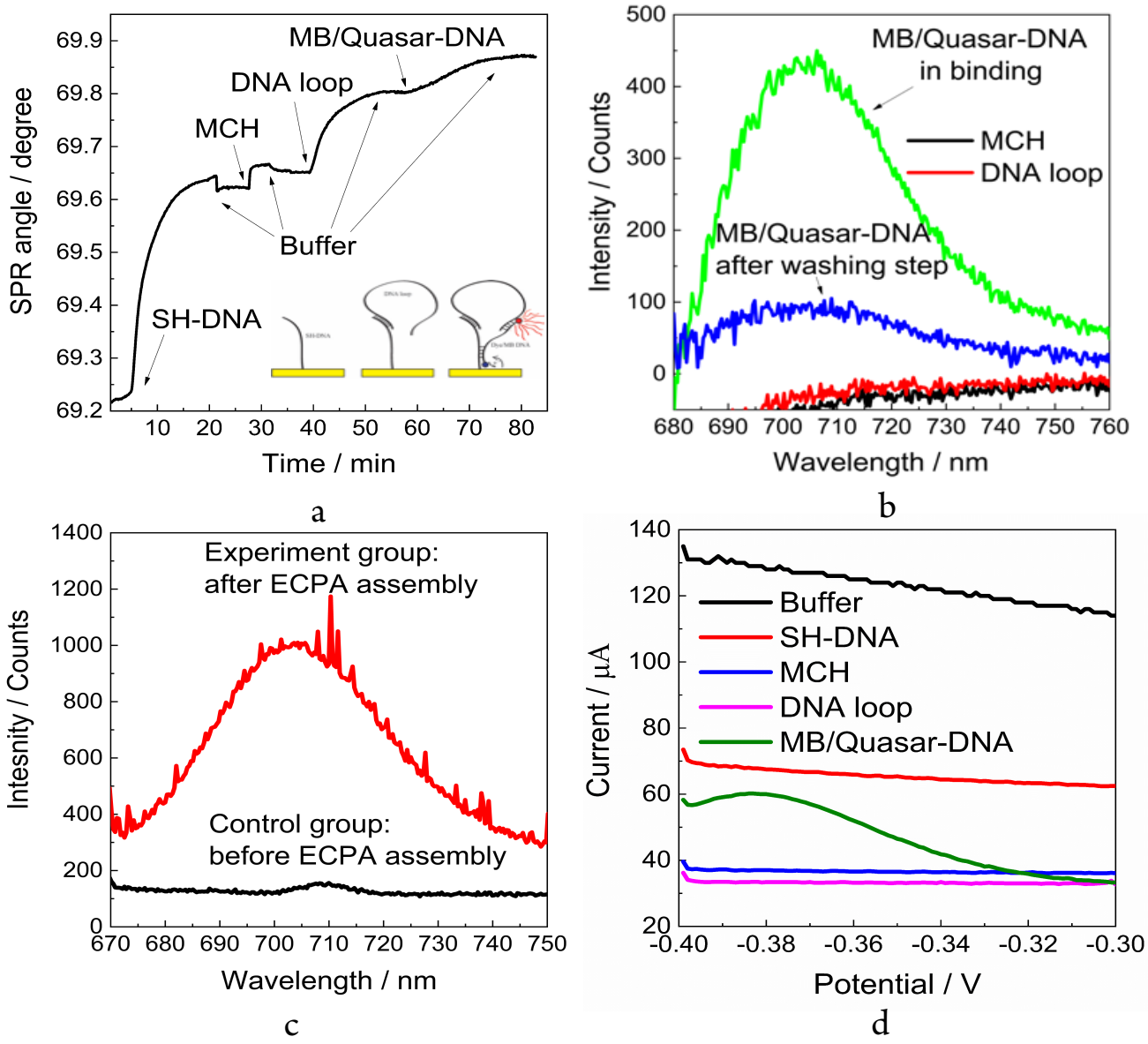


Figure 4.4 SPR/Fluorescence spectroelectrochemical characterization of ECPA model system in the sequential mode. a) SPR signal monitoring the assembly of each component. b) photon excited fluorescence emission spectrum and c) SPF emission spectrum monitoring the assembly of MB/Quasar-DNA via the fluorescence tag- Quasar 705. d) SWV spectrum monitoring the assembly of MB/Quasar-DNA via the electrochemical tag- MB.

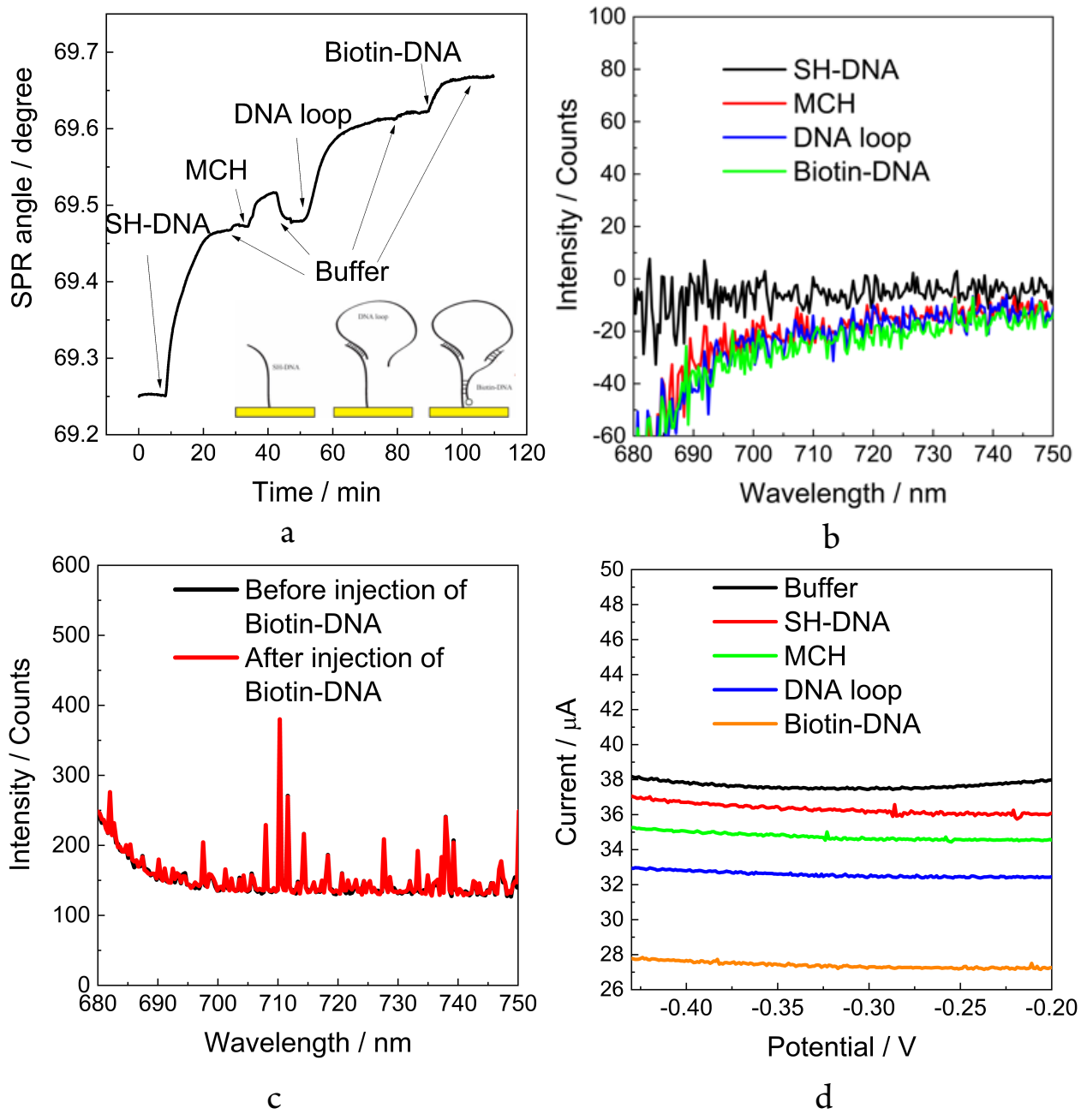


Figure 4.5 Control experiment: SPR/Fluorescence spectroelectrochemical characterization of ECPA model system in the absence of electrochemical or fluorescence label. a) SPR signal monitoring the assembly of each component. b) photon excited fluorescence emission spectrum and c) SPF emission spectrum monitoring the assembly of Biotin-DNA. d) SWV spectrum corresponding to each step of the assembly process.

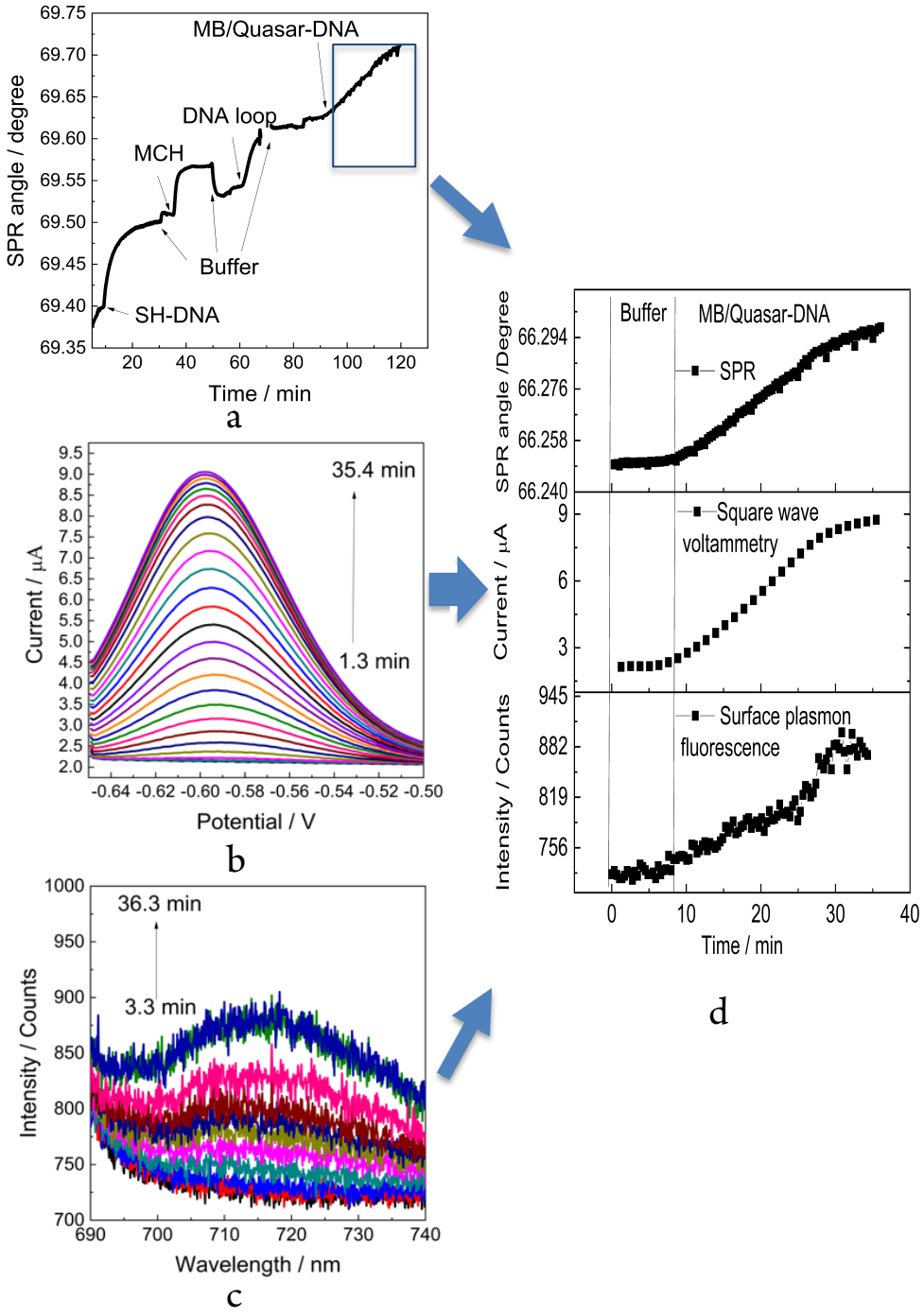


Figure 4.6 SPR/Fluorescence spectroelectrochemical characterization of dynamic binding of MB/Quasar-DNA on sensor surface in the parallel mode. a) SPR signal monitoring the process by the mass changes of MB/Quasar-DNA assembled on surface b) SWV spectrum monitoring the process by the redox of MB molecules approached to surface c) SPF spectrum monitoring the process by emitted fluorescence from Quasar 705 approached to surface. d) comparison of the dynamic curves extracted from three signals above, namely, SPR angle shifts/oxidation peaks/fluorescence intensities versus time.

#### 4.3.3.1 Sequential characterization

The SPR response showed the increase of SPR angle corresponding to each component of ECPA model system (Fig 4.4a), indicating the thickness of 1.6, 0.1, 0.6, 0.3 nm, and the surface coverage of 254, 18, 98 and 44 ng·cm-2 for SH-DNA, MCH, DNA loop, and MB/Quasar-DNA respectively. The response of photon excited fluorescence is shown as Fig 4.4b after background of buffer subtracted from the raw response of each component. No significant emission peak was observed before the injection of MB/Quasar-DNA solution. After its injection for 5 min, the fluorescence intensity reached 450 counts, which was subsequently reduced to 105 counts in washing step, owing to the removal of unbound MB/Quasar-DNA molecules. Compared with photo excited fluorescence, the SPF displayed an increase as high as 873 counts after washing step (Fig 4.4c). Therefore, SPF appeared to exhibit its superiority over photon excited fluorescence due to its enhancement effect of fluorescence. Nonetheless, photon excited fluorescence plays an irreplaceable role in the detection of fluorophores with large distance from the interfaces. Limited by the decay length of evanescence field, SPF is only applicable for the fluorophores within 109 nm (might vary to 200~300 nm on other sensor chips) of distance from the gold surface. As a complementary tool, the photon excited fluorescence is applicable for all the fluorophores, regardless of their positions. With the two complementary excitation techniques, more fluorescence experiment designs will be realized in future. After binding of MB/Quasar-DNA solution, SWV generated a stable MB oxidation peak of 26.7 μA at -0.38 V (Fig 4.4d). In contrast to previous electrochemical result, this MB oxidation peak shifted -0.12V, which could be attributed to the pseudo reference electrode integrated into the flow cell. To further verify the correspondence of observed signals to their source molecules, a control experiment was performed by replacing MB-DNA with Biotin-DNA, which has neither electrochemical nor fluorescent active moieties. The results showed SPR detected the efficient assembly of each component (Fig 4.5a), while no fluorescence emission peak (Fig 4.5b~c) or electrochemical oxidation peak (Fig 4.5d) was observed upon the binding of Biotin-DNA. Therefore, the successful parallel integration of SPR/Fluorescence/SPF/Electroche-mistry and the high specificity of electrochemical and fluorescence response for their source molecules have been proved.

#### 4.3.3.2 Parallel characterization

In this mode, either fluorescence or SPF is able to be detected. The latter was chosen here because it supplies molecular information specifically on the interface. The SPR response from Fig 4.6a indicated a similar assembly result as under the sequential mode. Fig 4.6b and 4.6c exhibited the changes of oxidation and emission peak of MB/Quasar-DNA as a function of time. The peak intensity of both signals was plotted versus observation time as shown in Fig 4.6d, which indicates that the kinetic curve of SPR angle is highly consistent with that of peak current and emission peak intensity. The linear growth of MB/Quasar-DNA was thus cross-validated by all the signals. From these kinetic curves, the increase rate for SPR, electrochemical and fluorescence signal is $3.25\times 10^{-3}$ degree/ min, 0.3 μA/min, and 5.8 counts/ min. Since these kinetic signals were indicating the same binding event of MB/Quasar-DNA, it is reasonable to relate one degree change of SPR angle to 92 μA of oxidation peak current, and 1785 counts of photons. Namely, 1 ng·cm$^{-2}$ of MB/Quasar-DNA bound on sensor caused the changes of $1.55\times 10^{-3}$ degree of SPR angle, 0.143 μA of oxidation peak and 2.76 counts of emission intensity. Our results show that the three synergistic responses obtained from the multimodal measurements of all three techniques gives a coherent validation of the binding event occurring at the interface level. With this, we demonstrate a highly reliable way to realize in-situ monitoring of dynamic changes of components involved in interfacial binding. More importantly, the obtained corresponding proportion relation among magnitudes of three signals provides us new opportunities for surface interrogations. For instance, as molecules of interest labelled with electrochemical and/or fluorescence tags, the magnitude changes of electrochemical and fluorescence signal could be converted into the corresponding SPR angle changes, which is further converted into concentration information. In this way, the dynamic changes of multi-components at interfaces can be tracked at the same time, and surface coverage and thickness of each of them is obtainable. For another instance, in the case of ECPA, as the biomarker is labeled with fluorophores, MB-DNA has methylene blue tag with it, the electrochemical signal changes indicate how many biomarker molecules are captured through specific binding. By converting this electrochemical current into corresponding fluorescence intensity, it is known how much portion of the total fluorescence comes from the specific binding, then also how much is responsible for non-specific binding.

## 4.4 Conclusions

A reliable interface study requires cross-validation and complementation from multiple techniques, however, is conventionally restricted by their sequential use. The biggest problem of the sequential use is, the inability in in-situ monitoring of dynamic changes. In this study, a SPR/Fluorescence coupled spectroelectrochemical technique was displayed that integrated two optical techniques together with electrochemical methods. This technique not only provides convenience in operation of multiple signals in single platform, but also achieves in-situ tracking of molecular dynamic changes via three techniques simultaneously. The proof-of-concept of this technique was accomplished by ECPA model system. The design is, SPR generates signals upon assembly of each component, fluorescence intensity changed only upon the assembly of fluorophore-labeled pieces, while the characteristic electrochemical signal was only detected as MB-labeled piece approached to the gold surface. The results showed that, as expected, through sequential characterization, the assembly of MB/Quasar-DNA strand resulted in synchronous increase of SPR angle, fluorescence intensity as well as characteristic peak current; through parallel characterization, the assembly kinetics of MB/Quasar-DNA were investigated and cross-validated by three techniques. From these results, the recognition of binding components, and estimation of their thicknesses and surface coverages were realized. The confirmation from three signals enhances the reliability of obtained kinetic parameters, the observed corresponding proportion relation among three signals plays a significant role in the following works, including simultaneous characterization of multi-components in one step, differentiation of non-specific binding events, etc. Additionally, this proportional relation among signals provides a way to compare the sensitivity from different techniques, thus optimize the characterization system.

# 5. Study on the Electrochemical Proximity Assay of Platelet-Derived Growth factor using MPMS

## 5.1 Introduction

Platelet-Derived Growth Factor (PDGF) plays an important role in the regulation of tumor growth and division, and has been associated with cancer and other proliferative disease states[130,131]. As a potential cancer marker, PDGF is difficult to be detected in real blood sample due to its trace amount. To improve the sensitivity of PDGF detection as well as understand the sensor's mechanisms, we aim to combine MPMS and ECPA (Fig. 1) to achieve sensitive detection of PDGF in blood, and more importantly, simultaneously use SPR, electrochemical and fluorescence measurement to characterize the process of sensor preparation and protein recognition during ECPA of PDGF. As shown in Fig. 1, SPR should generate signal upon assembly of each step, while fluorescence and electrochemical signal will only change upon binding of the methylene blue/fluorophore labeled DNA strand.

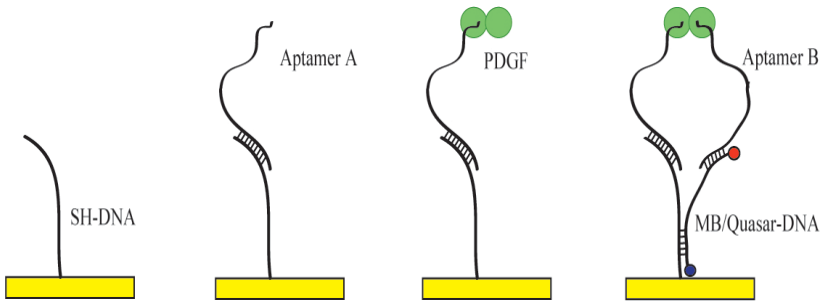


Figure 5.1 Schematic of designed ECPA for PDGF detection

## 5.2 Experimental section

### 5.2.1 Materials

The reagents used in this research were: 4-(2-hydroxyethyl)-1-piperazineethanesulfonic acid (HEPES) (99.5%) was purchased from Alfa Aesar. Sodium perchlorate anhydrous (ACS, 98.0-102.0%) and Alcohol anhydrous (ACS, ≥99%) were purchased from VWR International (LLC Radnor, PA). 6-Mercapto-1-hexanol was purchased from TCI (Boston, MA). Bovine serum albumin (BSA, lyophilized powder) was purchased from Hyclone (South Logan, UT). PDGF-BB

was from R&D Systems (Minneapolis, MN). Methylene blue/Quasar-conjugated DNA (MB/Quasar-DNA) was purchased from Biosearch Technologies (Novato, California), purified by RP-HPLC. Oligonucleotides and aptamers were purchased from Integrated DNA Technologies (Coralville, Iowa), with purity and yield confirmed by mass spectrometry and HPLC. Sequences for these DNA strands were as table.3 (listed 5' to 3').

Table 3. DNA sequences used in this study

| Name | Sequence |
|---|---|
| SH-DNA | ThioMC6-D/GCA TGG TAT TTT TCG TTC GTT AGG GTT CAA ATC CGC G |
| Aptamer A | CAG GCT ACG GCA CGT AGA GCA TCA CCA TGA TCC TG ACC CAC TTA AAC CTC AAT CCA CGC GGA TTT GAA CCC TAA CG |
| Aptamer B | TAG GAA AAG GAG GAG GGT GGC CCA CTT AAA CCT CAA TCC CAG GCT ACG GCA CGT AGA GCA TCA CCA TGA TCC TG |
| MB/Quasar-DNA | Quasar 705/CCA CCC TCC TCC TTT TCC TAT CTC TCC CTC GTC ACC AUG C/MB |

### 5.2.2 Assembly of ECPA for PDGF detection

Gold slides (50nm) were purchased from BioNavis, Tampere, Finland and used in this study. After exposure to piranha solution (30% $H_2O_2$: $H_2SO_4$=1:3, by volumn) for 2min, the sensor slide was thoroughly cleaned by pure water and dried with nitrogen, followed by placing it into the sensor holder and inserted into the instrument for detection. Prior to assembly of ECPA, 10 μL of 200 μM SH- DNA was mixed with 20 μL of 10 mM TCEP. This mixture was incubated in the dark at room temperature for 90 min to reduce the disulfide bonds, and then diluted to a total volume of 970 μL by HEPES / $NaClO_4$ buffer (10mM HEPES, 0.5 M $NaClO_4$, pH 7.5) with a final concentration of 2 μM. The DNA loop formation on the surface of the

sensor was carried by injecting 2 µM SH-DNA, 3 mM MCH, 0.5 µM Aptamer A, 8nM PDGF (or 50nM BSA), 50 nM Aptamer B & MB/Quasar DNA duplex alternately.

### 5.3 Results and discussion

#### 5.3.1 Testify the efficacy of Enzyme regeneration method

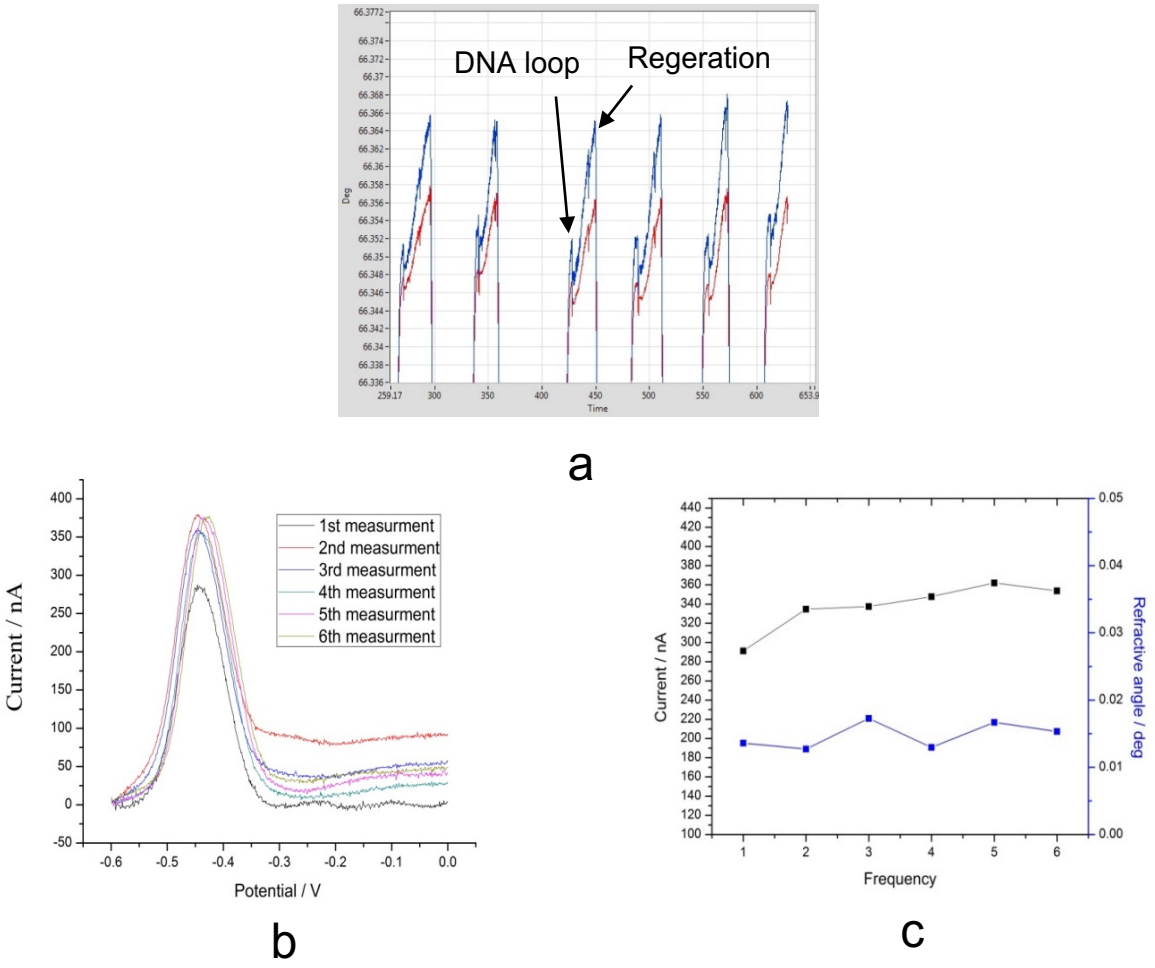


Figure 5.2 repeated detection of 50 nM DNA loop by a) SPR signal b) SWV signal c) comparison of SPR and SWV responses

In our preliminary test, it was found sensors have different effective surface areas, especially after the piranha solution treatment. Therefore, the regeneration method on the same sensor is necessary to guarantee the same surface condition for the target protein challenging. We used uracil excision mix to regenerate the ligands, good repeatability of SPR signal was

obtained for simplified ECPA. Two sensors were pretreated by piranha solution for 5min and incubated with of 2uM SH-DNA, 3mM MCH for 14h and 30min in beaker, respectively. Subsequently, the sensors were placed into SPR instrument for SPR measurement only (no square wave voltammetry involved). The injection procedure was, firstly flowed with Hepes buffer solution until the baseline reaches stable; mixture of 10nM DNA loop and 15nM reduced MB was injected for 10min, followed by buffer until the SPR signal was stable. The regeneration process was, as the temperature of flowcell was raised to 37 °C, the pre-heated (37 °C) Urasil Excision solution (20U/L) was injected for 7min, and followed by introduction of ddH2O for 5min to wash the enzyme solution away. As the temperature was reduced to 21 °C, buffer at RT was simultaneously injected until the stability of SPR signal. The procedure was repeated as above for the next detection. The SPR curve shows the refractive angle changed as function of time. The baseline was able to reach the same level after regeneration, indicating the successful regeneration using enzyme solution. Fig 5.2a~c exhibits the SPR response due to binding of loop and MB DNA mixture for Sensor 3. The binding event demonstrated a linear growth of these components on gold surface. The magnitude of every running was approximately consistent with each other within one day. For the repeated six measurements, the SPR kinetic curves are coincident with each other, and the net increase of refractive angle due to the loop and MB DNA binding was 13.3, 11.8, 13.3, 12.8, 10.6, 12.7 milidegree respectively. The standard deviation and relative standard deviation are 1 milidegree and 8.3%. The good reproducibility of the obtained results above verified the effectiveness of enzyme solution on sensor's regeneration, causing no loss of the amounts and activity of ligands during the process of at least six repeats. Currently, we are testing if other signals including fluorescence intensity and characteristic current peak are changing after enzyme regeneration.

### 5.3.2 Comparison of signals using 8 nM PDGF and control solution

SPR response (Fig 5.3a) displays increase of refractive angle upon each component, indicating successful assembly of these pieces. The thickness and surface coverage of DNA layers on the sensor surface was calculated using equations described by Naimushin et al. [132]and Jung et al.[133] based on the refractive angle change. The thickness of SH-DNA, MCH, Aptamer A and Aptamer B & MB/Quasar DNA duplex was estimated as 3, 0.38, 0.68, 0.15nm respectively. Their corresponding surface coverage on the sensor is 501, 62, 112.73, and 25.05 ng/cm$^2$. It is also worthy to note the increase of refractive angle due to PDGF is 0.15°.

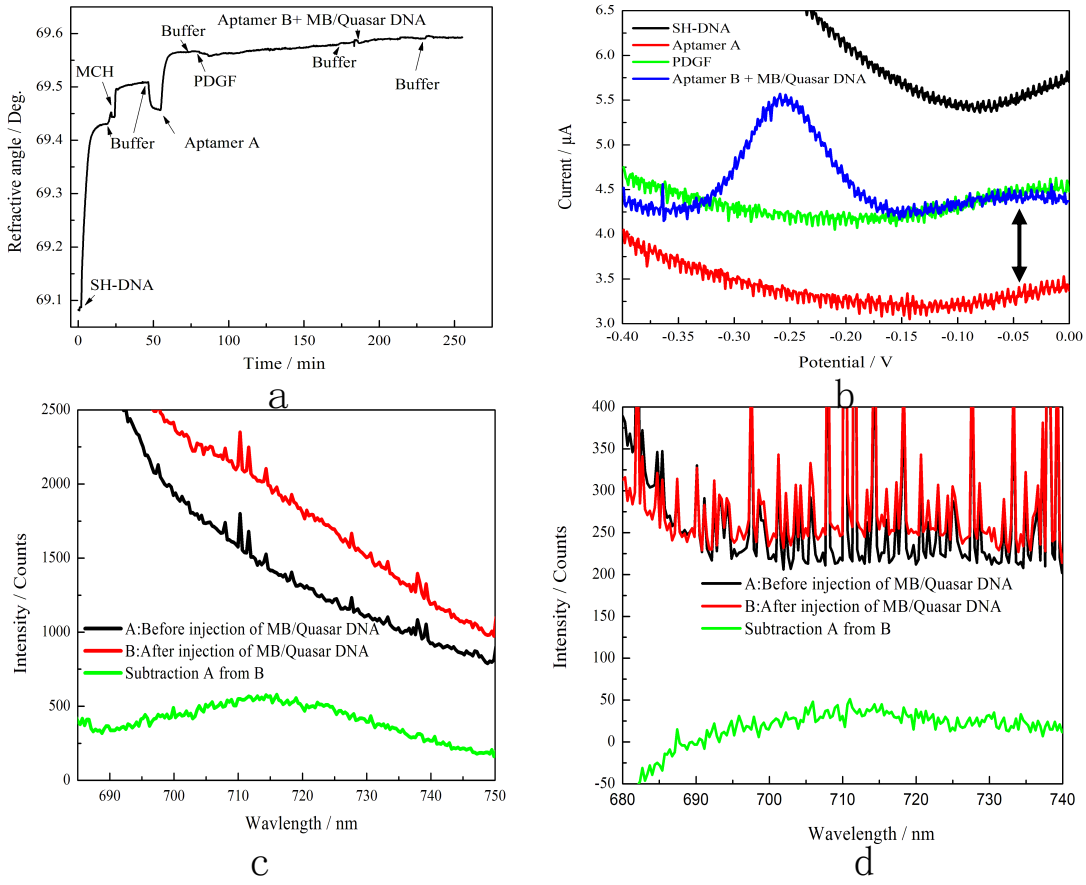


Figure 5.3 a) SPR response b) Square wave voltammetry c) fluorescence response and d) surface plasmon fluorescence response for ECPA of 8nM PDGF

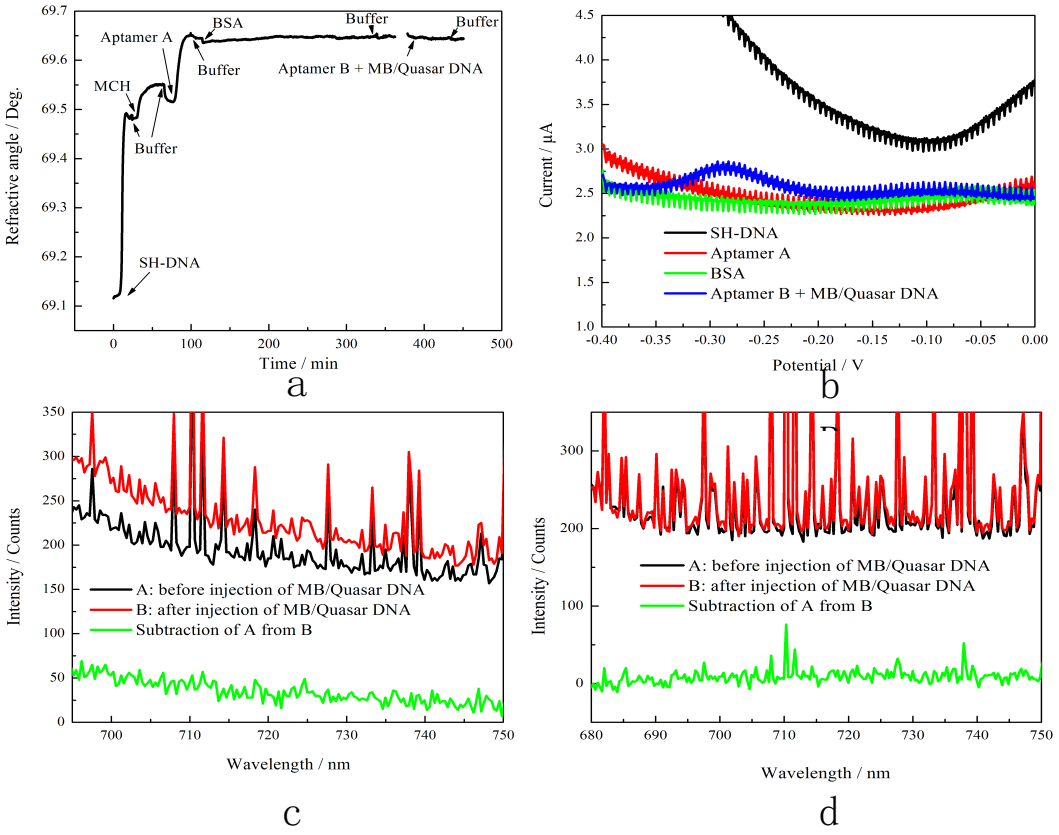


Figure 5.4 a) SPR response b) Square wave voltammetry c) fluorescence response d) surface plasmon fluorescence response for ECPA of 50nM BSA

Prior to the introduction of MB/Quasar DNA, only reduction of background current (Fig 5.3b) was observed by the assembly of each component. A MB oxidation peak as high as 1.36 μA appeared at −250 mV only in the presence of MB-DNA. The fluorescence and surface plasmon fluorescence response was shown in Fig 5.3c~d. The black curves show the emission spectra prior to PDGF assembly, the red curves show the emission spectra after its assembly. The green curves represent the difference between them, which reflects the net change of spectra. In the presence of MB/Quasar labeled DNA, a distinct MB oxidation peak appeared, and the emission peak from fluorophore was detected as high as 500 and 50 counts, by fluorescence and surface plasmon fluorescence respectively.

In contrast, 50nM BSA was used as control to challenge the assembled sensor. Through SPR curves in Fig 5.4a, the thickness of thickness of SH-DNA, MCH, Aptamer A was estimated

as 3, 0.25, 1.088nm respectively. Their corresponding surface coverage on the sensor is 501, 41.75, 180.92 ng/cm$^2$. At the same time, the increase of refractive angle

due to BSA was both zero, indicating no nonspecific binding of BSA. The fluorescence and surface plasmon fluorescence were not distinct as well (Fig 5.4c~d), that further validated no binding of target proteins. However, an oxidation peak of MB was detected as low as 0.3 μA (Fig 5.4b). This current peak might result from the undesired interaction between MB/Quasar DNA and SH-DNA in the absence of target PDGF, since these two DNA sequences have 7 complementary pairs. Even so, the peak intensity was 4.5 times lower than that in the presence of 8nM PDGF. This phenomenon could be validated by the other signals in Table.4, which all showed significant difference between control and experiment group. It is interesting to observe that, among all of the techniques, fluorescence signal generated the largest difference between control and experiment group, therefor is likely to have a highest sensitivity for PDGF detection.

Table 4. The comparison of three signals for control and experiment group

| | 8 nM PDGF | 50 nM BSA |
|---|---|---|
| SPR angle increase | 0.15 | 0 |
| Fluorescence (Counts) | 570 | 30 |
| Surface plasmon | 45 | 10 |
| SWV(μA) | 1.36 | 0.3 |

However, in our following study using SH-DNA with 5 complementary base pairs with Quasar/MB-DNA, we have failed to observe the electrochemical signal.

### 5.3.3 Effect of $Mg^{2+}$ on molecular interactions

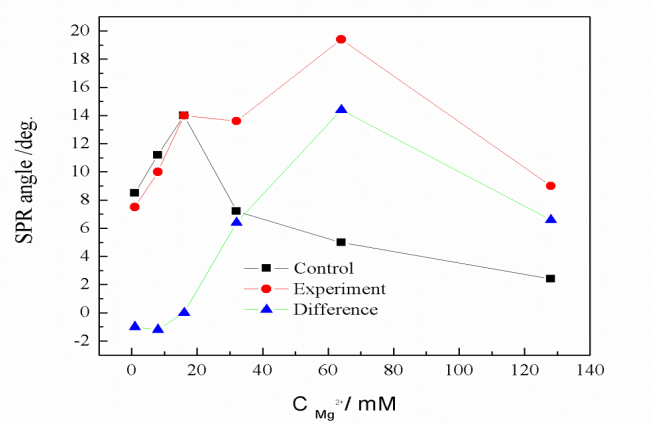


Figure 5.5 Effect of $Mg^{2+}$ on the binding association rate

Dications have been proven able to bind with nucleic acid in various sites such as, the phosphate oxygen, and N7 of guanine. Regarding the promotion of DNA hybridization, they provide higher efficiency than monocations. Therefore, here we tested on the binding association rate of 2nM PDGFs on its aptamer under different $Mg^{2+}$ concentration in buffer (Fig 5.5). In the absence of aptamers, PDGFs had non-specific binding with sensor surface, the non-specific binding rate of PDGFs increased with rising $Mg^{2+}$ concentration at the range of 0~16 mM, and decreased above 16 mM. As PDGF's aptamers were bound, the association rate of PDGFs increased with rising $Mg^{2+}$ concentration at the range of 0~64 mM, and decreased above 64 mM. As non-specific binding rate (in the absence of PDGFs) was deducted from the total binding rate (in the presence of PDGFs), the net association rate of PDGFs due to its aptamer capture was shown as green curve. The highest association rate appears at 64mM $Mg^{2+}$. Below this concentration, the increase of $Mg^{2+}$ concentration stabilized the three-way helix conformation of PDGF aptamers, allowing higher affinity. At the same time in this regime, protein solubility increases with increasing salt concentration due to low salt concenration. As the concentration of $Mg^{2+}$ surpassed 64 mM, the high salt concentration in buffer reduced the solubility of proteins, leading less efficient binding with its aptamers. These results show that an optimum concentration of $Mg^{2+}$ ion at 64mM for the detection of PDGF-BB, thus chosen in the present study.

### 5.3.6 Effect of $Na^+$ /$Mg^{2+}$ on electrochemical signal

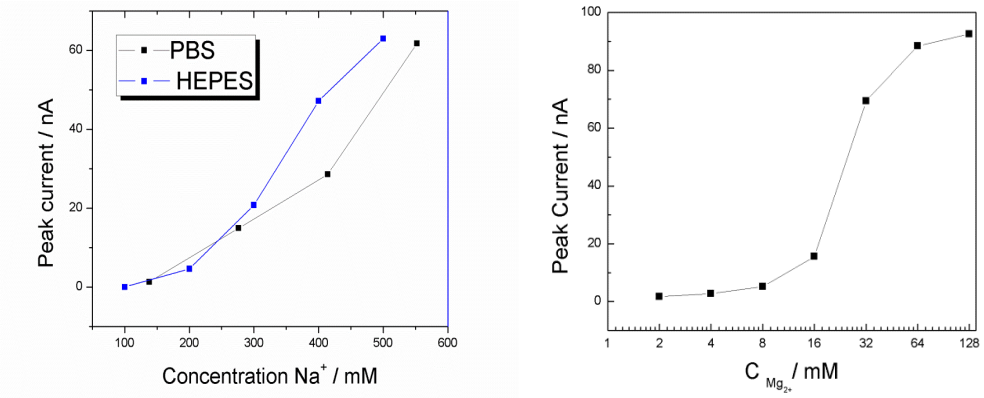


Figure 5.6 Effect of $Na^+$ /$Mg^{2+}$ on the electrochemical signal

Cations influence not only the molecular interaction, but also the hybridization of oligonucleic acids. Herein, the same sensor assembled in 25 mM DNA loop and Quasar/MB-DNA for 10 min was placed respectively in buffers containing different $Na^+$ and $Mg^{2+}$ concentrations. The obtained current peaks by SWV are shown as Fig 5.6. The peak current increased with the concentration of both $Na^+$ and $Mg^{2+}$. This indicated not all Quasar/MB-DNAs were able to form double helix structure with SH-DNA in spite that the Quasar/MB-DNAs had been brought close to gold surface via binding of DNA loop. A higher cation concentration improves the hybridization between Quasar/MB-DNA and SH-DNA, which enhanced the electrochemical signal. It is also interesting to notice the different behavior of PBS pH 7.5 and HEPES/$NaClO_4$ pH 7.5 buffer at the same concentration of $Na^+$. With the same $Na^+$ amount present in solution, HEPES/$NaClO_4$ buffer provides stronger electrochemical peaks than in PBS buffer. The current peak has a significant growth in the range between 8~64 mM $Mg^{2+}$. This enhancement involves two mechanisms. On one hand, due to the binding of $Mg^{2+}$ on DNA, the negative charges of DNA are partially neutralized so the complimentary DNA is able to approach and interact in an easier fashion. On the other hand, according to Debye–Huckel model, the thickness of electric double layer decreases as increase in the electrolyte concentration. Therefore, the electrostatic repulsion force of the interface reduces for Quasar/MB-DNA, which improves its hybridization efficiency with SH-DNA. Of note, the oxidation current of MB did

not change much after the concentration of $Mg^{2+}$ reached 64 mM, which demonstrated the saturation of hybridization between two complementary DNAs.

### 5.3.7 Effect of concentration of MB-DNA in 64mM $MgCl_2$ added PBS

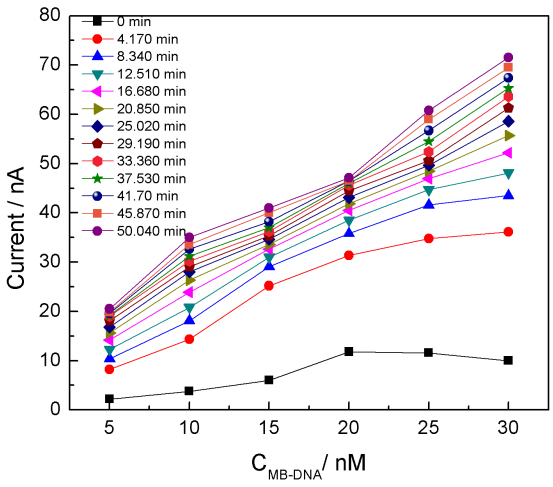


Figure 5.7 Effect of concentration of MB-DNA on the oxidation current

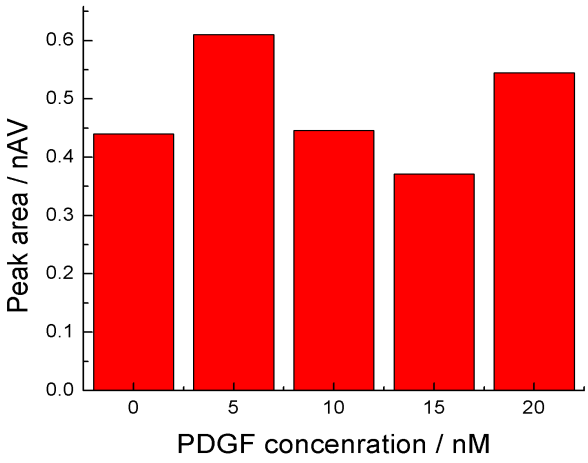


Figure 5.8 Detection of PDGF in PBS containing 64mM $MgCl_2$

In order to find the optimal concentration of MB-DNA for PDGF detection, various amounts of MB-DNA were incubated with the same electrode. The square wave voltammetry was performed every 4 min until 30min was reached. It could be seen that the the oxidation current of MB-DNA increased with the concentration of MB-DNA (Fig 5.7). No critical point

was found, thus 15 nM was selected as the average value. As the concentration of MB-DNA on the biointerface surpasses 15 nM due to the PDGF and its aptamers' binding, the oxidation current is expetected to increase, generating linear dyamic responses corresponding to the PDGF amounts captured. However, as 0~20 nM PDGF solutions were tested, no linear response was observed (Fig 5.8). Therefore, the PBS buffer containing 64mM $MgCl_2$ is not applicable for the PDGF detection. In the following experiments, PBS containing 15 mM $MgCl_2$ was tested as dilution buffer.

### 5.3.8 Evidence from gel shift test

Firstly, as PBS containing 15 mM $MgCl_2$ was used for PDGF detection. The interaction between PDGF and its aptamers was testified by gel shift test (Fig 5.10). After 45 min running of electrophoresis at 80 V, the aptamer oligonucleotides with size less than 100 bp were moving ahead of the 200 bp DNA standard. A portion of the aptamers were separated from the free aptamers due to its interaction with PDGF molecules, which reduced the

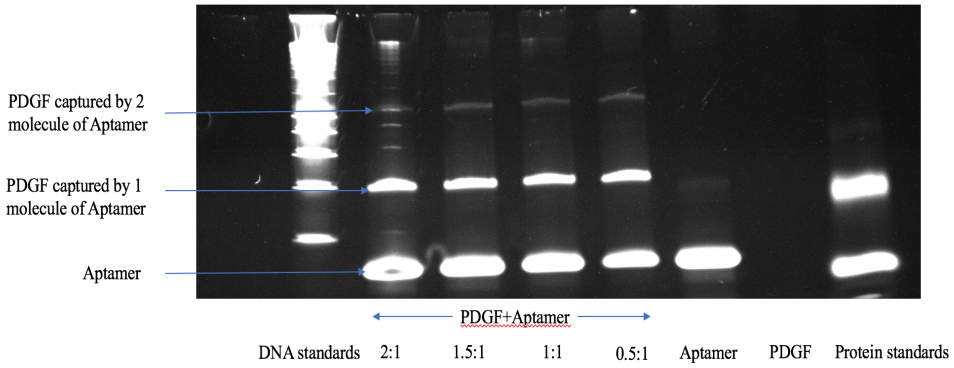


Figure 5.9 gel shift test of PDGF/aptamer interaction

mobility of the complex. Two bands were found lagging far behind the band belonging to free aptamers. It is speculated that the band closest to the free aptamer band belonge to the 1:1 PDGF/Aptamer complex, while the other band belongs to the 1:2 PDGF/Aptamer complex. The fluorescence intensity of free aptamer band was much higher than the PDGF/Aptamer complex bands, which indicated small portion of PDGF/Aptamer complex in all aptamer confirmation. The intensity of 1:2 PDGF/Aptamer complex took an even smaller portion. Interestingly, as the

ratio of PDGF and aptamer changed continuously from 0.5:1 to 2:1, there was no apparent intensity change observed for the complex. This phenomenon probably indicated that only small portion of PDGF is active to bind with two aptamers, and it tends to saturate as adequate aptamer molecule present in solution. The low binding efficiency of PDGF with two aptamers simultaneously is also consistent with previous studies. It was reported[88] approximately 1 PDGF molecule in 25 was able to bind two different aptamers.

### 5.3.9 Effect of $C_{MB\text{-}DNA}$ on background current

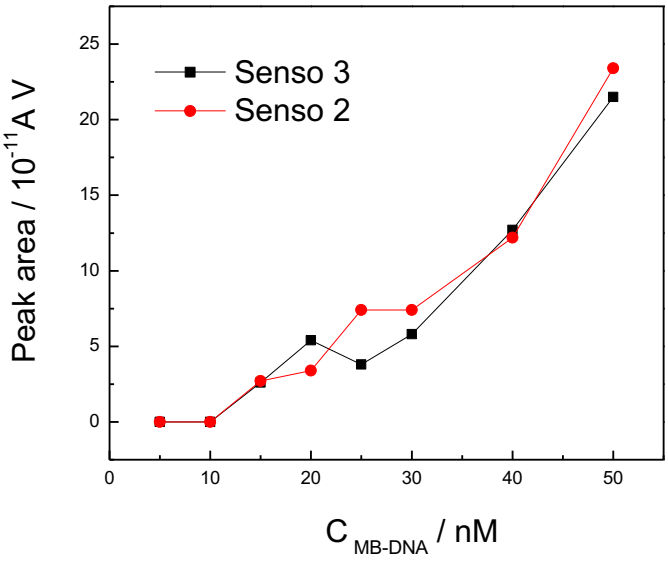


Figure 5.10 Effect of $C_{MB\text{-}DNA}$ on background current

Subsequently, as $Mg^{2+}$ concentration was determined as 15 mM, the effect of concentration of signal molecule MB-DNA was investigated as Fig 5.10. The reaction time was fixed at 10 min. It is clear to see the critical point locates at 10 nM. An apparent oxidation peak of MB appeared as the concentration of Quasar/MB-DNA surpassed 10 nM. Thus 10 nM was chosen as the concentration of Quasar/MB-DNA in the following experiments.

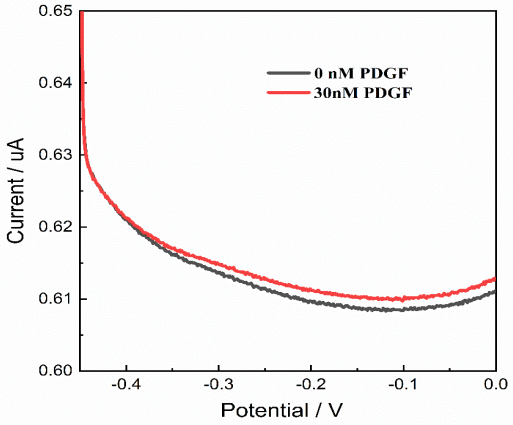


Figure 5.10 Comparison on the SWV spectrum between 0 and 30 nM PDGF in PBS containing 15 mM $MgCl_2$

Under the conditions of 10 nM MB-DNA, we compared the responses from 0 and 30 nM PDGF, no signficant difference was observed.

### 5.3.10 Results from G7 SH-DNA and PBS containing 276mM NaCl, and 2mM $MgCl_2$

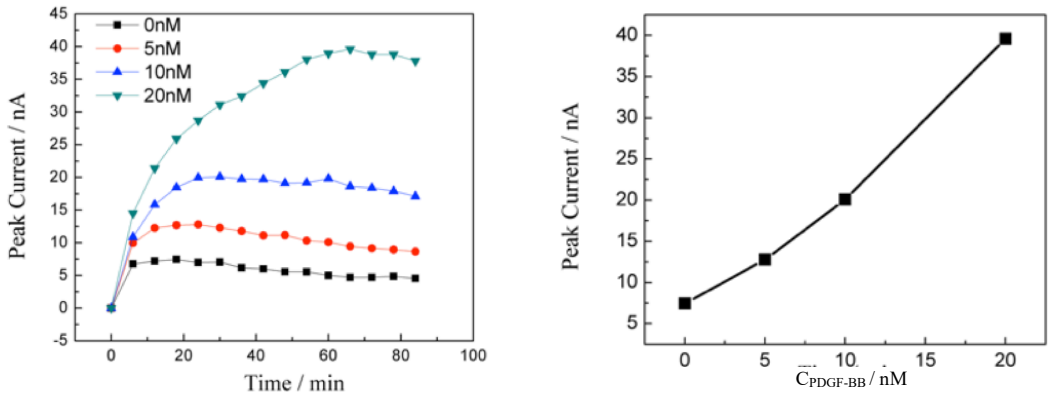


Figure 5.11 Various concentrations of PDGF displayed dynamic responses of electrochemical signals as function of a) time and b) concentrations.

Subsequently, we increased the hybridization force between MB-DNA and SH-DNA by increasing two complimentary pairs (G5->G7), and reduced the ionic strength by using 10mM PBS, 276mM NaCl, 5.4mM KCl, 2mM $MgCl_2$, pH 7.4. 20 nM Aptamer A, 20 nM Aptamer B, and 20 nM MB-DNA were mixed with various concentrations of PDGF (total volume= 2 mL) and incubated in room temperature for 1h. The mixture was then reacted with the electrode. The

square wave voltammetry was performed every 3min. Fig 5.11 shows that as the current signal reached plateaus, the concentrations of PDGFs displayed linear relation with their current intensities. It was also noticed that the time to reach plateaus was different for every concentraions. The equilibrim time increased from 3min for 0 nM PDGF to 60 min for 20 nM PDGF. This indicates a benefit of this reaction system for trace amounts of analytes, namely, less time is required for the finish point of reaction.

### 5.4 Conclusions and discussions

In conclusion, using the newly developed MPMS, SPR, electrochemistry, fluorescence, and surface plasmon fluorescence spectroscopies have been integrated to characterize the ECPA of PDGF simultaneously. These signals did not interfere each other, and achieved cross-validation of the assembly of ECPA. SPR generated signal upon assembly of each component, fluorescence and surface plasmon fluorescence only changed upon assembly of the labeled pieces, while characteristic electrochemical signal was only detected when MB-labeled DNA was assembled. With this system, the action and dynamics in the sensor preparation and protein recognition becomes ‘visualized’. In addition, MPMS has been demonstrated to have a great potential to achieve sensitive detection of PDGF. As G5 SH-DNA was used in this system, we found the cations present in the buffer solution has influence in the aspect of oligonucleotide hybridization efficiency, aptamer-protein interaction and background signals. However, in the optimized conditions, no dynamic responses were observed from different concentrations of PDGF. While G7 SH-DNA replaced G5 SH-DNA, and a lower ionic strength was used, a linear growth of the current signal was observed with the increasing concentrations of PDGF. This phenomona implies that the cations influence ECPA of PDGF in two aspects. On one hand, the binding of two aptamers with PDGF heavily depends on the concentrations of cations. In the presence of an excess of magnesium ions, a single aptamer has a high infinity with PDGF. However, this one-to-one binding inhibits further binding with the second aptamer. This is likely due to lack of flexibility of the aptamer in high cation environment. The binding between PDGF and a single aptamer changes the structures of themselves. Therefore, the second aptamer has to be more flexiable to fit into the changed binding site of PDGF. Nevertheless, the high concentrated cation stabilizes the aptamer’s structure, which restricts its structure change. Therefore, in high cation

environment, it is likely that only one aptamer is able to bind with PDGF. In low cation environment, due to the flexibility of aptamers, PDGF is able to bind with two aptamers.

On the other hand, the low cationic concentration is unfavorable for the hybridization betwenn SH-DNA and MB-DNA. Especially for G5 SH-DNA with only five pairs of complimentary bases, low cations means low effeciency of hybrization, as well as weak electrochemical signal. Therefore, G7 SH-DNA increases the hybrization force in low cationic environment, allowing the presence of electrochemical signals.

# 6. Detection of Neurotoxin Tricresyl Phosphate Using Automatic In-Situ Monitor System

## 6.1 Introduction

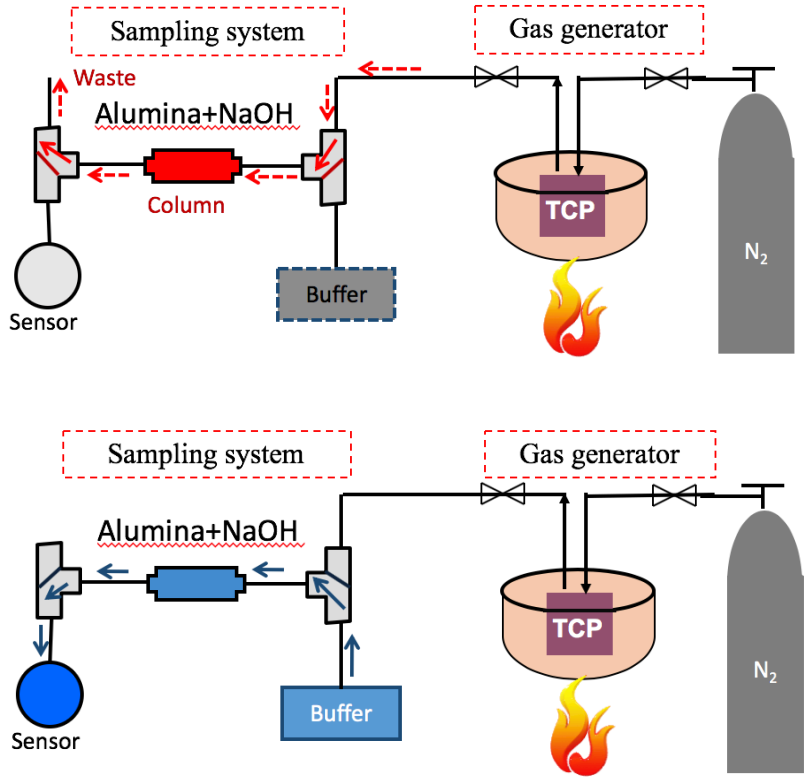


Figure 6.1 Schematic of operation of TCP detection system in the process of top) TCP sampling and bottom) eluent collection for cresol analysis

In previous researches, Dr. Xiaoyun Yang developed a system to detect tricresyl phosphate (TCP) through heterogeneous hydrolysis and electrochemical measurement (Fig 6.1). This system was computer controlled, with gaseous TCP in, and hydrolysate solution out. A disadvantage of this system is, due to the usage of disposable sampling column, the column was not able to regenerate itself. This not only introduces more chemicals to environment, but also increases the reagent and cost of detection. Futhermore, the resulted extremely basic solution leads to some limitation and difficulty for the detection system. Therefore, we explored on the development of reagentless catalyst for TCP's hydrolysis. In addition, the operational parameters are investigated for the first time in the improved system. The automatic TCP sampling system

was built as described in Ref 1[134](Fig 6.1). All gaseous TCP samples were blown through alkaline powder catalyst column, and then buffer was flushed through the column to collect the hydrolysed products. By these processes, TCP gas samples were converted to liquid samples containing corresponding concentrations of cresol, making it possible to detect TCP quantitatively by an electrochemical method. Effects of gas flow rate, alumina column type, column temperature and concentration of NaOH in regeneration process were investigated.

## 6.2 Experimental section

### 6.2.1 Reagents and solutions

p-cresol (Acros Organics, NJ, 99+%) was dissolved in PBS ($Na_2HPO_4/KH_2PO_4$ : 0.2 M/0.2 M final concentrations, pH=6.67, NaCl= 10 mM). $Na_2HPO_4$ (Fisher, NJ, 99.8%) and $KH_2PO_4$ (Fisher, NJ) were used as received. For the detection of tri-p-cresol phosphate (TCP, pfaltrz&Bauer, CT) in solution, it was dissolved in methanol and diluted by PBS, and converted by 1M NaOH by hydrolysis. For TCP gas samples, they were converted to cresol with alkaline powder catalyst. Alkaline powder was made from NaOH (Fisher, NJ) and $Al_2O_3$ (Sigma-Aldrich, MO. Aluminum oxide, activated, neutral, Brockmann). Pippet tips (USA Scientific, Inc. 20 µL beveled filter tips) was used to pack alkaline powder. p-cresol was dissolved in PBS. D.I. water used was from Millipore Direct-Q water purification system (resistivity 18 $M\Omega cm^{-2}$).

### 6.2.2. Apparatus

All amperometric experiments were performed with CH Instruments (CH1910B) Bi-Potentiopstat. Desktop computer were used to collect data. Flow injection analysis (FIA) was carried out using cell electrodes, one of which includes glassy carbon working electrode (2 mm Ø), and another of which includes stainless steel auxiliary electrode and Ag/AgCl reference electrode (BASi, IN). Coating solution was applied to produce the Ag/AgCl reference electrode before detection following instruction from company. The working electrode was polished after

usage with alumina powder (1, 0.3, and 0.05 μm in order). 10 mM NaCl was used to maintain the potential of reference electrode.

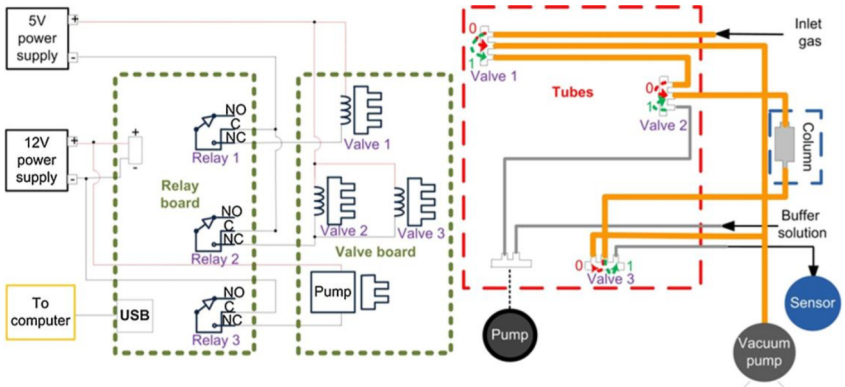


| Steps | Actions | Valves | | | Duration |
|---|---|---|---|---|---|
| | | 1 | 2 | 3 | |
| 1 | Initiation | / | / | / | |
| 2 | Gas flows in | on | / | / | 10 min. |
| 3 | Gas pumping ends | / | / | / | |
| 4 | Buffer elution starts | / | on | on | 6 min. |
| 5 | The elution solution is taken for electrochemical detection. The regeneration process starts by buffer washing | / | on | on | 5 min |

Figure 6.2 Schematic representation of automatic TCP detection system

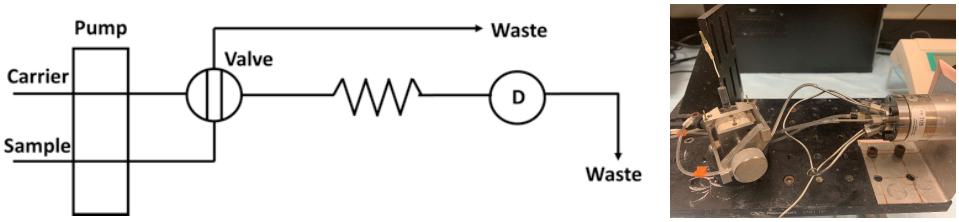


Figure 6.3 Schematic representation of flow injection electrochemical detection system

### 6.2.3 Preparation of Alkaline powder

Alkaline powder was preparing by mixing sodium hydroxide and alumina (1:10 wt) in ethanol under stirring condition for 1h until all sodium hydroxide was dissolved. The mixture was dried in a vacuum chamber. The dried powder was heated at 100 °C in oven before use. 100 mg of powder was packed into a pipette tip with filter which constituted the hydrolyzing column.

### 6.2.4 TCP gasification from methanol solution

The stock TCP solution (2 $mmol \cdot L^{-1}$) was prepared in methanol and diluted to TCP samples with concentrations of interest. 0.5 mL of TCP samples was gasified by 5 min $N_2$ blowing, followed by 5 min of $N_2$ blowing and 220 °C heating in silicon oil bath. The flow rate of $N_2$ was kept at 1.1 L/min. Gas was blown through the hydrolyzing column and converted to cresol.

### 6.2.5 Gas sample collection, conversion, and sampling into buffer solution

As shown in Fig 6.2, after collecting gas sample for 10 min, the catalyst column was flushed for 6 min. The converted TCP product was washed into solution, and finally detected by electrochemistry sensors.

### 6.2.6. Electrochemical measurement

All electrochemical experiments were made with a CH Instruments (CH1910B) Bi-Potentiostat. A standard desktop computer was used to collect data. a glassy carbon working electrode (2 mm Ø), a stainless-steel auxiliary electrode and Ag/AgCl reference electrode (BASi, IN) were used. The working electrode was polished with alumina powder (1, 0.3, and 0.05 μm in order) and rinsed with purified water. Cyclic Voltammery was performed with parameters as below, initial voltage 0V, high voltage 0.7 V, scan rate 0.1 V/s, scan interval 0.001 V, quite time 2s, sensitivity 10 μA/V.

For the amperometry monitoring of TCP, a flow injection system was used as shown in Fig 6.3. Switch injection unit (Valco Instruments Co. Inc.) was used with a 50 μL sample loading loop. The flow rate was maintained at 200 μL/min by using a single syringe pump (KD Scientific, MA).

## 6.3 Results and Discussion

### 6.3.1 Detection of p-cresol

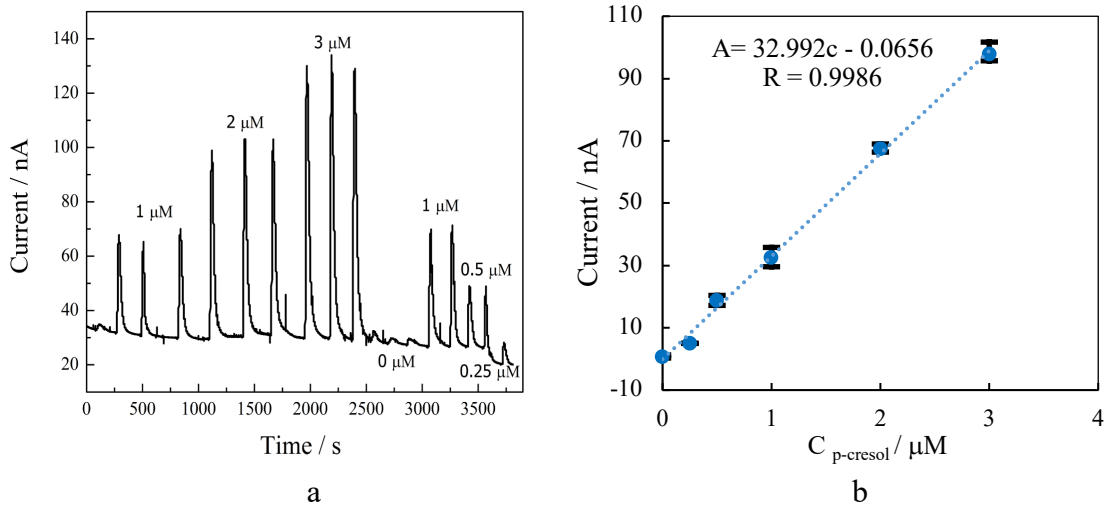


Figure 6.4 Calibration curve of cresol detection. The left figure shows the real-time amperometric response curve. The right figure shows the data after processing. Error bars show the repeatability of response.

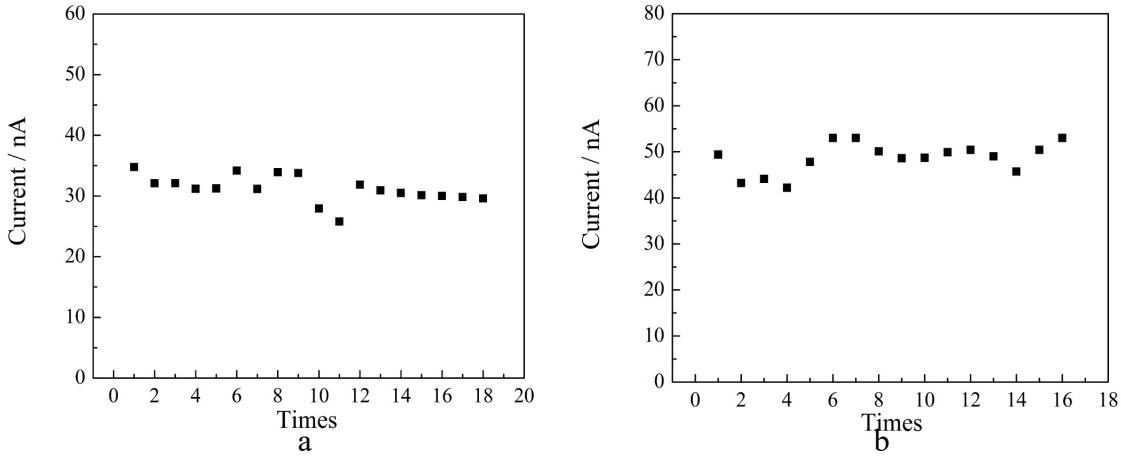


Figure 6.5 Repeatability test result of cresol detection. The left figure shows the detected current peak value of 1 μM for 18 times. The right figure shows the detected current peak value of 2 μM for 16 times.

The dynamic response for cresols is shown in Fig 6.4. Six different concentrations of cresols from 0~3 uM were introduced into the flow cell alternately. The current value increases linearly with the concentration of cresols, which shows a sensitivity of 33nA/μM. This value is

comparable to previous work. The correlation coefficient, 0.9973, shows good linearity in this range.

### 6.3.2 Repeatability test

As shown in Fig 6.5, 1μM p-cresol solution was injected into flow cell for 18 times. The average current peak is 31 nA. The standard deviation is 2.4 nA, which shows a relative standard deviation of 7.7%. The same procedure was repeated for 2 μM p-cresol for 16 times. The average current peak is 48 nA. The standard deviation is 3.3 nA, which shows a relative standard deviation of 6.9%. These results demonstrate good repeatability for the cresol detection. Combined with results in 3.1, the detection limit reached 0.2 μM according to the signal-to-noise characteristics (S/N=3).

### 6.3.3 Determination of TCP in solution

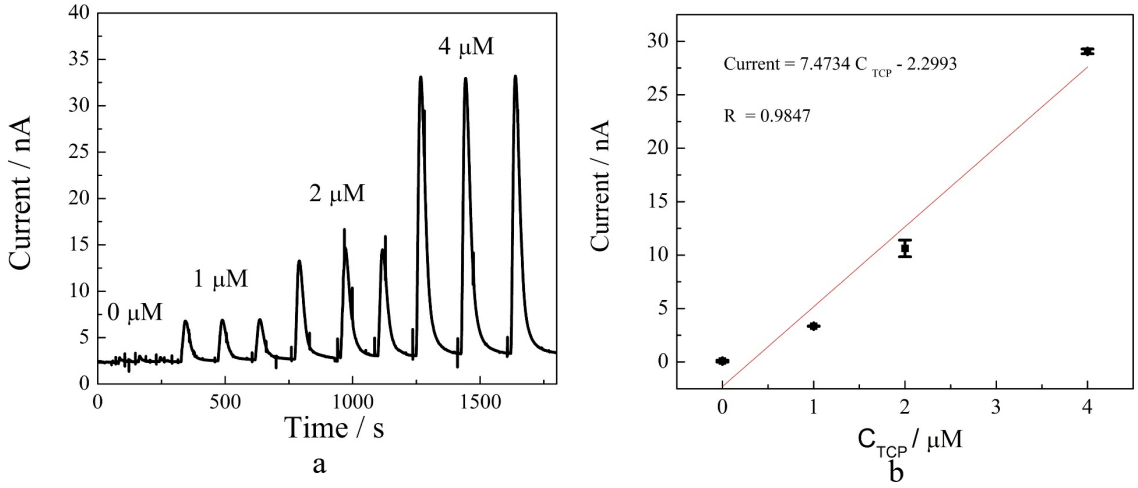


Figure 6.6 Calibration curve of TCP in solution. a ) shows the real-time amperometric response curve. b ) shows the data after processing. Error bars show the repeatability of response.

To test the capability of this system for TCP hydrolysis, TCP in solution was used as the test sample first. 50 μL TCP at the concentration of 0~0.8 mM was respectively mixed with 50uL 1M NaOH solution. After 3min of hydrolysis, 9.9 mL PBS was added into the solution to form 0~4uM TCP solutions. These solutions were directly injected into the system. The results shown in Fig 6.6 exhibit good linearity and repeatability. The current intensity increases linearly with the concentration of TCP. The sensitivity is 7.47 nA/μM. The correlation coefficient is 0.97.

### 6.3.4 Effect of elution time, dynamic response, and repeatability

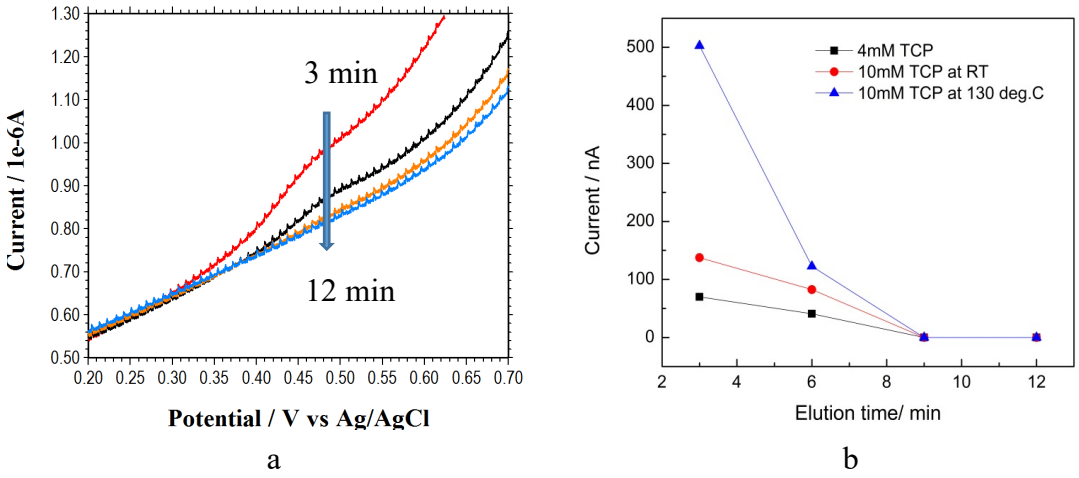


a b

Figure 6.7 a) Cyclic voltammetry response at different elution time from 3min~12min. b) Peak current at cyclic voltammetry as function of elution time.

The hydrolysis column was filled with freshly prepared neutral alumina/NaOH powders. The effect of elution time on cyclic voltammetry peaks was investigated (Figure 6.7a). A 10mM TCP sample, after gasified by $N_2$ bubbling, was flowed through the hydrolysis column for 5min. During the subsequent elution process, the eluent was collected every 3 min and a cyclic voltammetry scan was conducted. As shown in figure 6.7b, the current peak reduced as the elution time increased until the peak reached zero at 9 min. This indicates after 6min, there were no cresols washed out of the column. Therefore, the elution time was selected as 6 min to guarantee the complete wash-out of TCP.

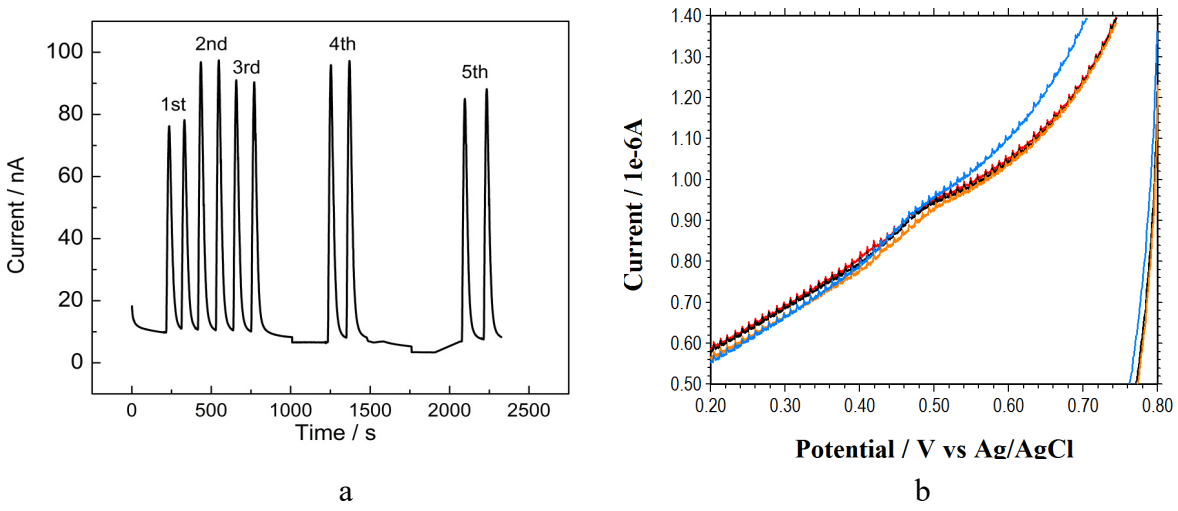


a b

Figure 6.8 a) amperometry response for repeated injections of 2mM TCP gasified samples. b) cyclic voltammetry response for repeated detections of 2mM TCP gasified samples.

Subsequently, 2mM TCP in methanol was gasified, pre-concentrated, hydrolyzed and detected. This process was repeated for 5 times. The amperometry results for these five repeats are displayed in Figure 6.8a. As seen from the figure, a large variance of current peaks was observed. Whereas, the CV response for the same l samples did not show significant difference in Figure 6.8b.

### 6.3.5. Experiments on commercial SPE column

In the following experiments, commercial SPE column was used instead of the self-made alumina material. The packed material in SPE column is neutral aluminum oxide. A new nitrogen regulator and valve were used to control the nitrogen flow rate.

All the solutions were prepared by pH 12 PBS with different concentrations. TCP was injected into hydrolysis column and expected to be hydrolyzed and subsequently detected by electrochemical system in flowcell.

To investigate elution time, 1.4uM TCP in gas was used. Elution times ranging from 3min to 12min were investigated. The results in Figure 6.9a show that the cresols were washed out completely after 6min at 0.5mL/min. We select 6min as the elution time, and measure the response of different amounts of TCP by CV and amperometry. Figures 6.0b&c show good repeatability and linearity obtained from the commercial alumina column.

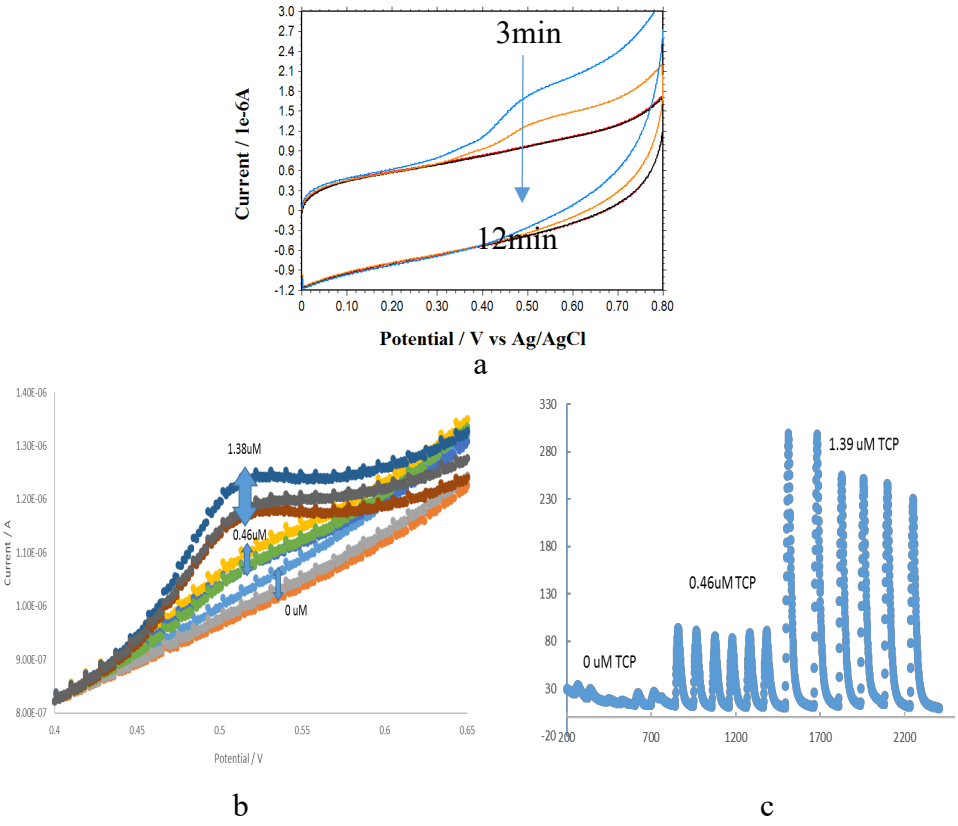


Figure 6.9 a) effect of elution time on the measurement of TCP. b) cyclic voltammetry of TCP sample in gas from 0~1.38 uM c) amperometry of TCP sample in gas from 0~1.38 uM

### 6.3.6 Effect of NaOH concentration in regeneration process

During column regeneration, various sodium hydroxide solutions were used to wash the alumina column for 5min. The eluent solutions are pH 13 PBS (0.05M). 1mM TCP in methanol was placed in the gasifier flask, and introduced into the hydrolysis column, which is expected to be hydrolyzed and subsequently detected by electrochemical system in flowcell. Cyclic voltammetry was applied in the range of 0~0.8V, the electrochemical response is shown in Figure 6.10a-b. Compared with the CV response of cresols in the pH 13 PBS solution, the

current peak obtained here was comparable to 0.2M p-cresol solution, which gave a hydrolysis efficiency of approximately 1/15.

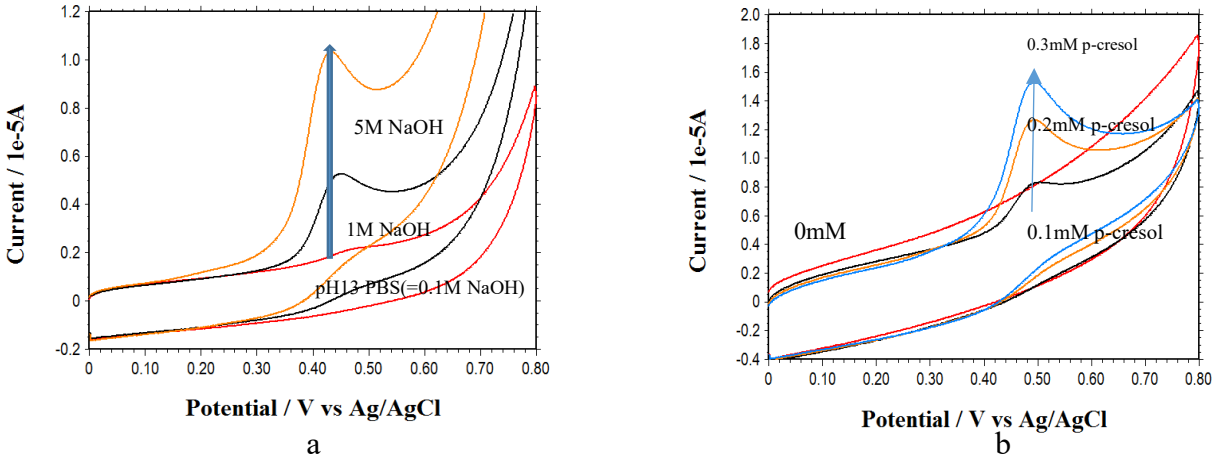


Figure 6.10 a) effect of the NaOH concentration in the regeneration process. b) CV response of p-cresol in pH 13 PBS buffer

### 6.3.7 Effect of flow rate

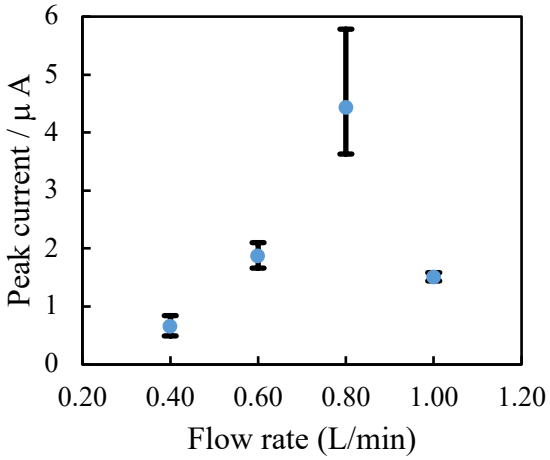


Figure 6.11 effect of flow rate on measurement of TCP in gas sample

Flow rates at 0.4~1 L/min were separately tested. The TCP concentration in methanol was 2mM. Having injected TCP into evaporation flask, the flask was placed onto the crucible heated to 230 °C for 5min. The elution was conducted by pH 13 PBS for 6min at 0.5 mL/min. The

collected solution was applied with cyclic voltammetry immediately. The column was regenerated by flushing it with 5M NaOH for 6min at 0.5 mL/min. A drying procedure was followed by using nitrogen flow of 1.1L/min for 5min at 230 °C.

The results Figure 6.11 showed that as flow rate increased from 0.4 to 0.8 L/min, the signal was enhanced. The continuous growth of flow rate reduced the peak current. 0.8 L/min was chosen as the flow rate in the following experiments.

### 6.3.8 Comparison of neutral and basic alumina column using automatic TCP detection system

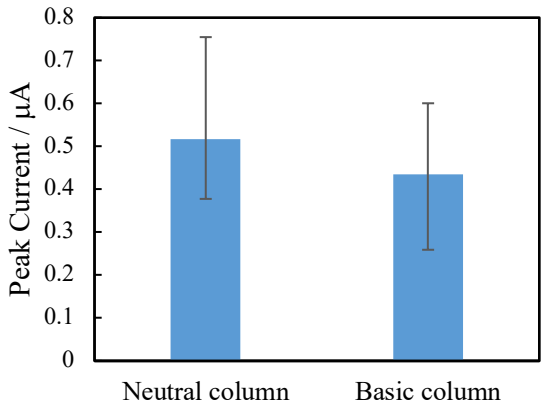


Figure 6.12 comparison of neutral and basic alumina column

The TCP detection system has been rebuilt. All the solutions were able to be injected and controlled by a LabVIEW controlled flow injection system as described in Ref.1. Neutral and basic alumina columns were used to compare the generated signals. Each column was repeated three times. The result Figure 6.12 showed the neutral column created slightly higher current peaks than basic alumina column.

### 6.3.9 Comparison of basic alumina column at room temperature and 40 °C using automatic TCP detection system

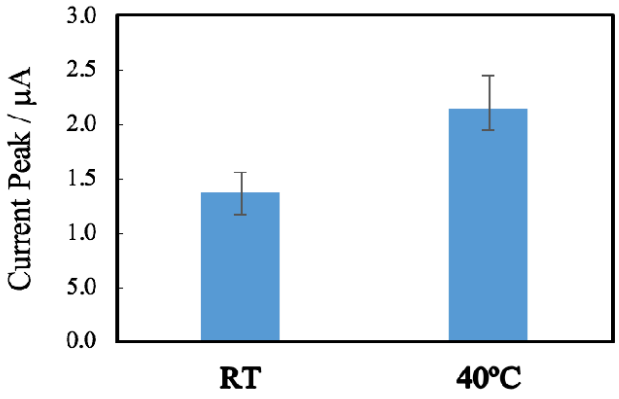


Figure 6.13 effect of column temperature

Alumina column temperature is expected to influence the adsorption and hydrolysis efficiency of TCP. To test the effect of column temperature, the column was placed at room temperature and in a water bath of 40°C. This experiment was performed in the automatic TCP detection system. The result in Figure 6.13 showed 40°C has a higher current response than RT, indicating a significant effect of the column temperature on the hydrolysis of TCP.

### 6.3.10 Calibration curve of TCPs

Under the optimal conditions, the dynamic responses of amperometry were investigated for various concentrations of TCPs. In the range of 0~1024 ppb, the oxidation current showed linear growth from 0 to 3.68 µA (Fig 6.14). The sensitivity is 3.6 nA/ ppb. The limit of detection is 216 ppb.

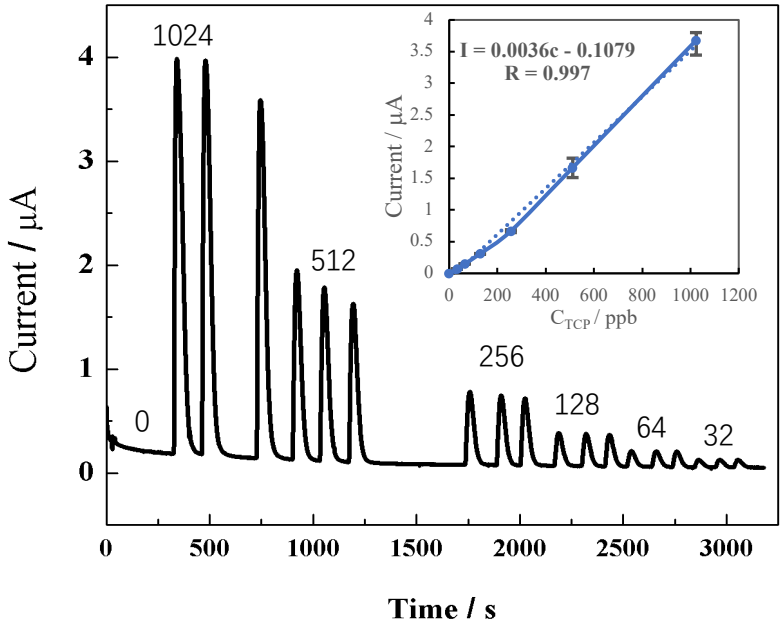


Figure 6.14 dynamic responses of various concentrations of TCPs

## 6.4 Conclusions

p-cresol and TCP in solution can be detected with good linearity and repeatability. A comparable sensitivity of 33nA/ μM with previous work was achieved for p-cresol solution. Its standard deviation is 2.4 nA. The relative standard deviation of 7.7%. A detection limit of 0.2 μM was obtained.

Automatic detection of TCP in gas has been achieved. Before each measurement, the regeneration process was required for the same alumina column. Using self-made alumina column, all the cresol products were washed out within six minutes and the amperometry result showed large variation among different measurements. As commercial alumina column was used instead, good repeatability and linearity were obtained from both amperometry and cyclic voltammetry. In addition, it was found the higher pH of the regeneration solution resulted in a stronger oxidation peak of cresols. Therefore, 5M NaOH was used as regeneration solution. The effects of gas flow rate were investigated. As flow rate increased from 0.4 to 0.8 L/min, the signal was enhanced. The continuous growth on flow rate reduced the peak current. 0.8 L/min is the optimal flow rate. The automatic TCP detection system has been built and capable of hydrolyzing TCP, generating oxidation peak of cresols. Using this system, the comparison of

neutral and basic alumina column was conducted. The neutral alumina column generated higher oxidation peaks for cresols than the basic alumina column. The effect of column temperature was obtained as well. The column at 40°C resulted in more cresols than that at room temperature. Under the optimal conditions, the oxidation current showed linear growth in the range of 0~1024 ppb TCPs. The sensitivity is 3.6 nA/ ppb. The limit of detection is 216 ppb.

# 7. Study on decomposition of TCP

## 7.1 Introduction

Organophosphates in environment poses severe threat to the health of humanity. Since their introduction into the environment in the 1950s, there have been considerable interest in eliminating and mitigating their effects[135]. Catalysts can rapidly hydrolyze organophosphates into less toxic or nontoxic compounds, so the health threat is greatly reduced. At the same time, timely awareness of these chemicals in environment plays a vital role in exposure assessment, damage control, and diagnosis and treatment of diseases to minimized the harm caused by the ongoing exposure. These organophosphate pesticides are generally inert, therefore, to detect these organophosphate pesticides and nerve agents, it usually requires the decomposition of the organophosphate compounds by breakdown of the ester bonds within, and generation of chemically active molecules. This process could be achieved also by catalysts. TCP is one of those organophosphate compounds. As is well-known, TCP itself is relatively inactive, it requires hydrolysis into phosphate ions and cresol using an alkaline catalyst before cresol generated could be detected.

Nonetheless, at the same time of catalysis of TCP hydrolysis, the alkaline catalyst is consuming itself, so continuous addition of alkaline catalyst is in demand for in-situ monitoring of TCP in environment. This not only introduces more chemicals to environment, but also increases the reagent and cost of detection. Futhermore, the resulted extremely basic solution leads to some limitation and difficulty for the detection system. Therefore, we explored on the development of reagentless catalyst for TCP's hydrolysis.

Metal oxides such as iron (III) oxides, copper (II) oxide are capable of achieving the hydrolysis of TCP reagentlessly, even though the reaction conditions require temperature above 400 ºC and heating duration as long as 1h[136]. These conditions are not practical to fulfill for a wearable sensor. Under room temperature and around neutral pH conditions, the catalyzed hydrolysis of organophosphate using metal oxides requires a couple of days[137]. These facts indicate that the realization of an absolutely reagentless detection platform is challenging.

Iron Hydroxide shows strong affinity as an adsorbent, even though no data has showed yet its ability in catalytic hydrolysis. Ruthenium hydroxide shows catalytic capability for hydration of Nitriles, aerobic oxidations of various alcohols, diols, whereas there are no reports yet on the respect of catalytic hydrolysis[138]. In the present study, we found $Ru(OH)_3$ and $Fe(OH)_3$ could achieve high efficient alcholysis and hydrolysis of TCP in the absence of additional chemicals. In addition, it shows a high potential to be used as a catalyst for the hydrolysis and alcoholysis of other organophosphates.

## 7.2 Experimental section

### 7.2.1 Reagents and solutions

p-cresol (Acros Organics, NJ, 99+%) was dissolved in methanol. For the detection of tri-p-cresol phosphate (TCP, pfaltrz&Bauer, CT) in solution, it was dissolved in methanol. Folin-Denis Reagent was purchased from Sigma-Aldrich. All D.I. water used was from a Millipore Direct-Q water purification system (resistivity 18 $M\Omega \cdot cm^{-2}$).

### 7.2.2 Electrochemical measurement

All electrochemical experiments were made with a CH Instruments (CH1910B) Bi-Potentiostat. A standard desktop computer was used to collect data. a glassy carbon working electrode (2 mm Ø), a stainless-steel auxiliary electrode and Ag/AgCl reference electrode (BASi, IN) were used. The working electrode was polished with alumina powder (1, 0.3, and 0.05 μm in order) and rinsed with purified water. Cyclic Voltammery was performed with parameters as below, initial voltage 0V, high voltage 0.7 V, scan rate 0.1 V/s, scan interval 0.001 V, quite time 2s, sensitivity 10 μA/V.

### 7.2.3 Folin-Denis reaction

100 uL sample after metal hydroxide adsorption was mixed with 2 mL $Na_2CO_3$. After reaction of 5min, 100 uL 0.5X Folin-Denis Reagent was added and reacted for 30min. The UV-VIS spectroscopy was obtained.

### 7.2.4 Preparation of metal hydroxides

0.25 mmol $CuCl_2$, $CoCl_2$, $NiCl_2$, $MnCl_2$, $RuCl_3$, and $FeCl_3$ was dissolved in 0.25mL $H_2O$ in a EP tube, 0.75 mL 1M NaOH was added into the dissolved metal ion solution. As precipitates formed immediately, the tube was centrifuged at 12,000 rpm for 10 min. The supernatant was removed and 1 mL 75% methanol/ 25% $H_2O$ was added as washing reagent. After uniform dispersion of the precipitates, the same washing procedure as above was repeated for three times. At the last time, the supernatant was collected and measured by UV-VIS spectroscopy as control group.

### 7.2.5 Catalytic alcoholysis of TCP

The thoroughly washed metal hydroxides were added by 1mL 5mM TCP dissolved in 75% methanol / 25% $H_2O$ solution. After uniformly mixing, 10 or 20 min of reaction time was allowed, and followed by 10 min of centrifugation at 12,000 rpm. The supernatant was taken out for UV-VIS characterization.

### 7.2.6 Catalytic hydrolysis of TCP

TCP was first dissolved in acetone, and then diluted into 5mM by $H_2O$. Ru(OH)3 and Fe(OH)3 were added into the solution, 20min later, the solution was centrifuged for 10min at 12,000 rpm, the supernatant was collected for UV-VIS measurement.

## 7.3 Results and discussion

### 7.3.1 UV-VIS kinetic characterization of TCP alcoholysis

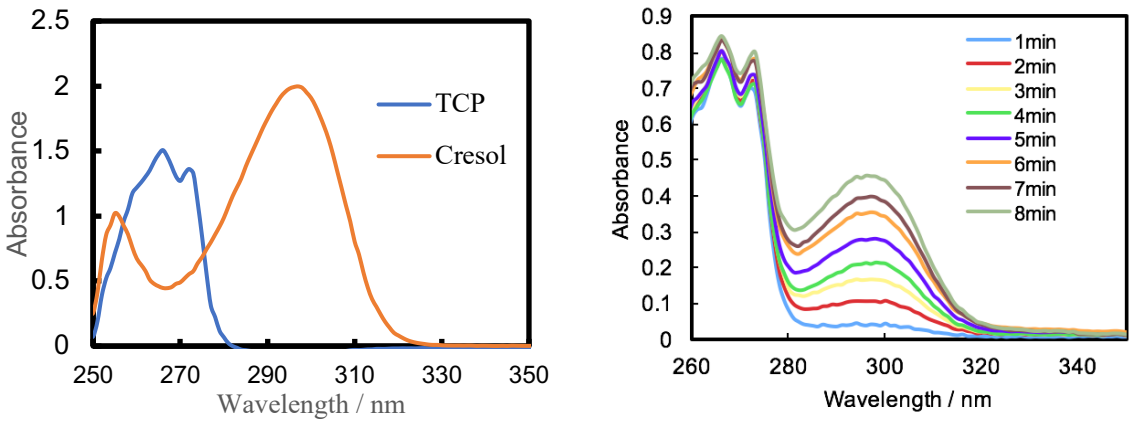


a b

Figure 7.1 UV-VIS spectrum of alcoholysis profile in a) the standard spectrum of TCP and p-cresol b) the dynamic profile of TCP basic alcoholysis at pH 13

Pure standard TCP and p-cresol solution showed that p-cresol has a characteristic absorption peak at 298 nm while TCP doesn't (Fig 7.1a). As TCP solution was placed in a pH 13 solution, the p-cresol peak at 298 nm appeared within the first minute of reaction and increased as function of reaction time, indicating the continuous production of p-cresol (Fig 7.1b). The reaction rate was 48 □M/ min. Therefore, the observation of alcoholysis process of TCP is enabled by UV-VIS characterization.

### 7.3.2 Catalytic alcoholysis of TCP by $Fe(OH)_3$ and $Ru(OH)_3$

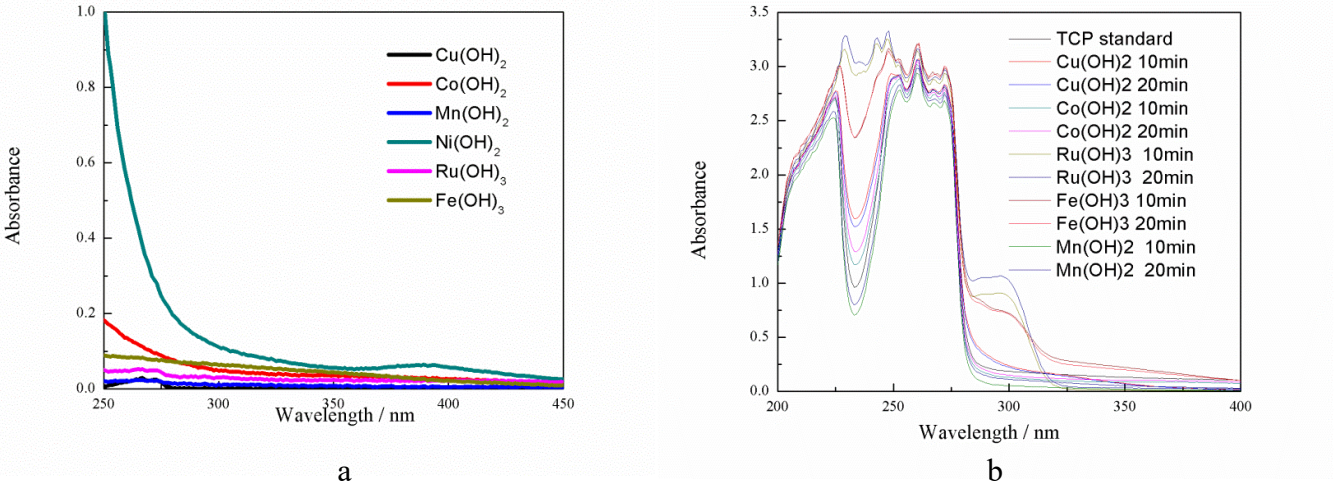


Figure 7.2 UV-VIS spectrum of a) in the absence and b) in the presence of 5 mM TCP in the case of different metal hydroxides

As washing step of various metal hydroxides finished, the supernatant was characterized by UV-VIS. As shown in Fig 7.2a, no peak was observed at the range of 250~450 nm. Afterwards, these thoroughly washed metal hydroxides were mixed with 5 mM TCP in 75% methanol/ 25% $H_2O$. After 10 min of incubation, the TCP solution mixed with $Ru(OH)_3$ and $Fe(OH)_3$ displayed a new characteristic peak at 298 nm belonging to p-cresol as shown in Fig 7.2b, while the standard TCP solution without addition of any metal hydroxide showed no peak at 298 nm. After another 10 min, this peak for $Fe(OH)_3$ remained the same while that for $Ru(OH)_3$ further increased. On the contrast, in the presence of $Cu(OH)_2$, $Co(OH)_2$, and $Mn(OH)_2$, the TCP solution did not display distinct difference with the TCP solution in the absence of these metal hydroxides after either 10 or 20 min. From these results, $Fe(OH)_3$ and $Ru(OH)_3$ exhibited its capability in catalyzing the alcoholysis of TCP. Using the calibration curve of standard p-cresol at 298 nm, the number of cresols produced in 10 min was calculated as 0.8 mM and 0.5mM in the presence of $Ru(OH)_3$ and $Fe(OH)_3$, respectively, which indicated a alcoholysis rate as high as 16% and 10%.

### 7.3.3 Folin-Denis reaction

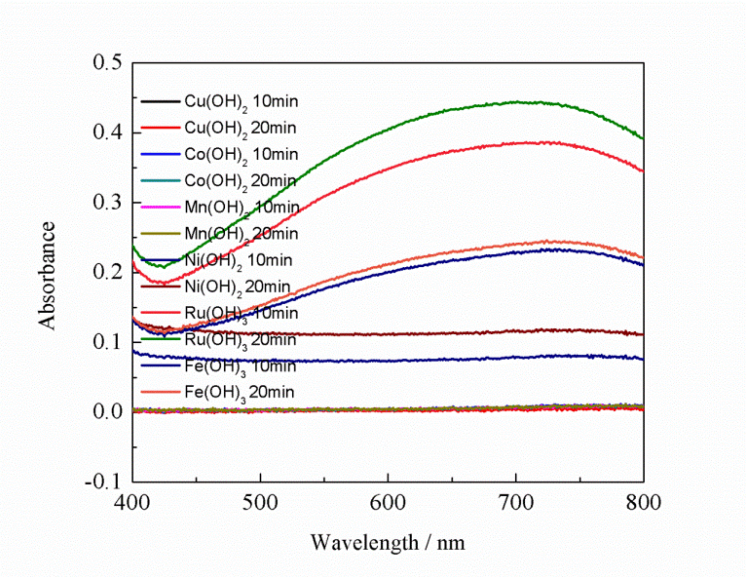


Figure 7.3 UV-VIS spectrum of resulted solutions after reaction with Folin-Denis reagent

To further confirm the production of p-cresols in the presence of $Ru(OH)_3$ and $Fe(OH)_3$, Folin-Denis test was performed on the same production solutions from above in the presence of the metal hydroxides. The UV-VIS spectrums in Figure 7.3 showed that only in the presence of $Ru(OH)_3$ and $Fe(OH)_3$, the TCP solution displayed an absorbance peak at 700 nm, which belongs to a blue chromophore constituted by a phenol-phosphotungstic- phosphomolybdenum complex. Compared with the calibration curves of standard p-cresol solutions, the produced cresol has a concentration of 1.3 mM and 0.7 mM for $Ru(OH)_3$ and $Fe(OH)_3$, respectively. This result validated the production of cresols. The higher value obtained via Folin-Denis method was presumably due to further alcoholysis of TCP in basic conditions during Folin-Denis reaction.

### 7.3.4 GC-MS characterization of TCP alcoholysis

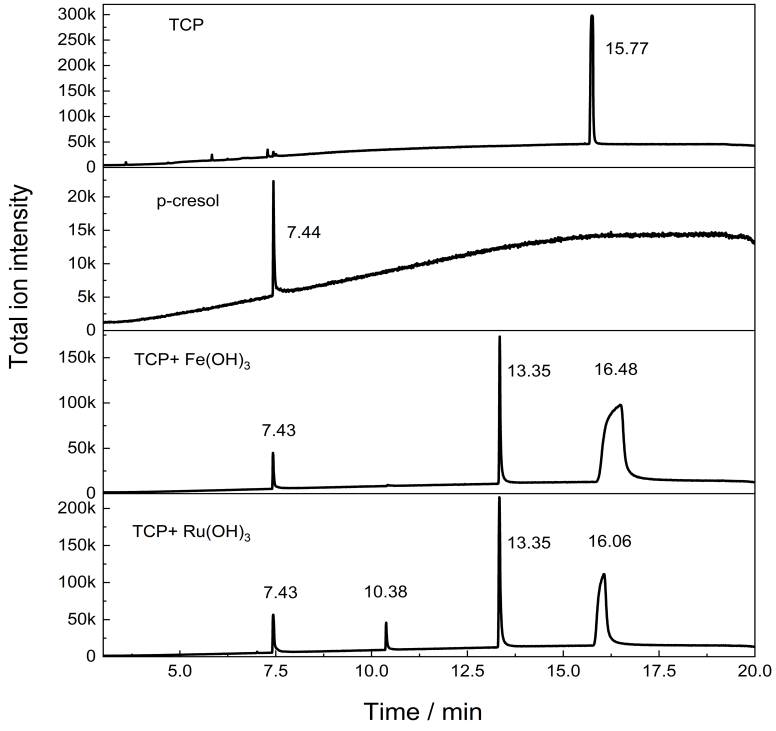


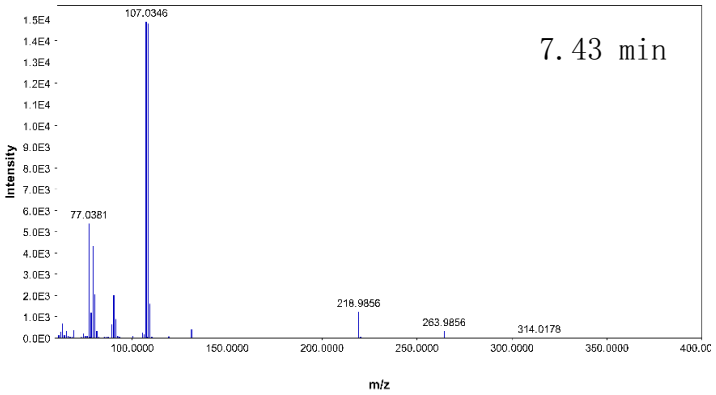


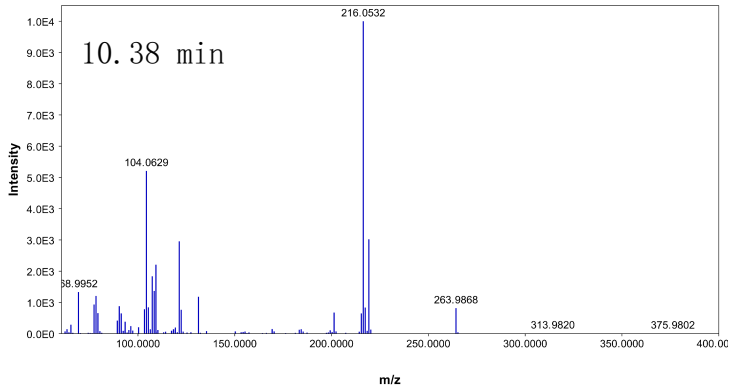

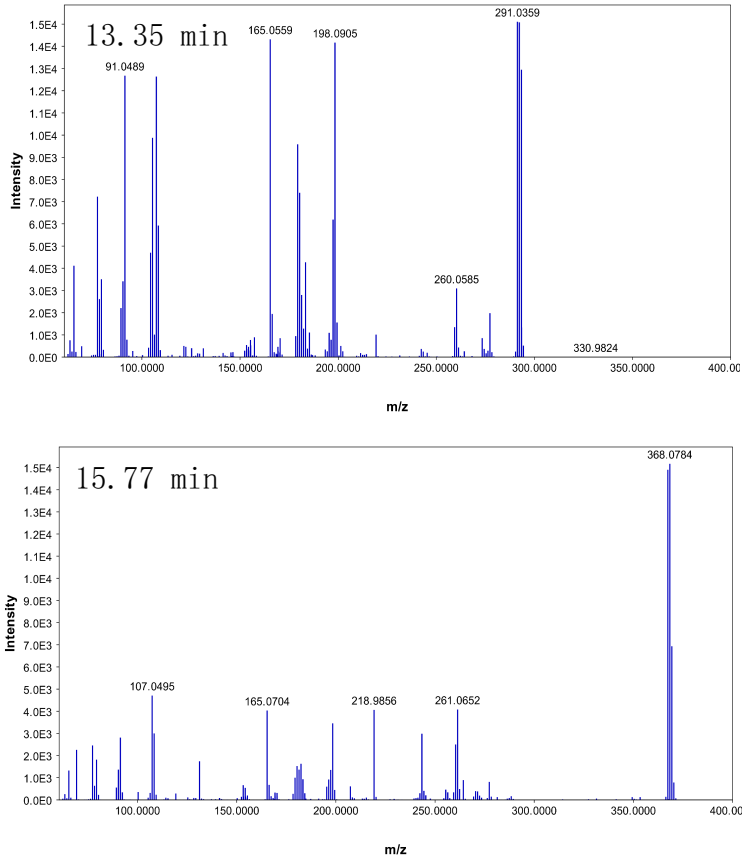


Figure 7.4 GC-MS results for 1mM cresols, 5mM TCP , and its solution after 20 min reaction with $Ru(OH)_3$ and $Fe(OH)_3$ in alcoholysis 75% methanol/ 25% $H_2O$

To further confirm the alcoholysis product p-cresol, the solutions after reaction of 20 min from above experiments were characterized by Gas Chromatography-Mass Spectrometer (GC-MS). The product solutions displayed multiple peaks, in which a mass of 107 was recognized at retention time 7.43 min, mass of 206.1 was recognized at 10.38 min, mass of 291 was recognized at 13.3 min, and mass of 368.1 was recognized at 16 min (Figure 7.4 for Ruthenium hydroxide and iron hydroxide). Through elemental composition analysis, the peak at 7.43 min belongs to p-cresol, the peak at 10.38min belongs to cresyl dimethyl phosphate, the peak at 13.3 min belongs to methyl dicresyl phosphate, the peak at 16 min belongs to tricresyl phosphate. It could be seen that under the catalysis of $Ru(OH)_3$, a portion of TCP experienced alcoholysis and released one molecule of cresol, while another portion of TCP released two molecules of cresols. Under the catalysis of $Fe(OH)_3$, the hydrolyzed TCP released only one molecule of cresol. Above all, the formation of cresols has been further proven as the result of TCP catalytic alcoholysis.

### 7.3.5 GC-MS characterization of TCP hydrolysis

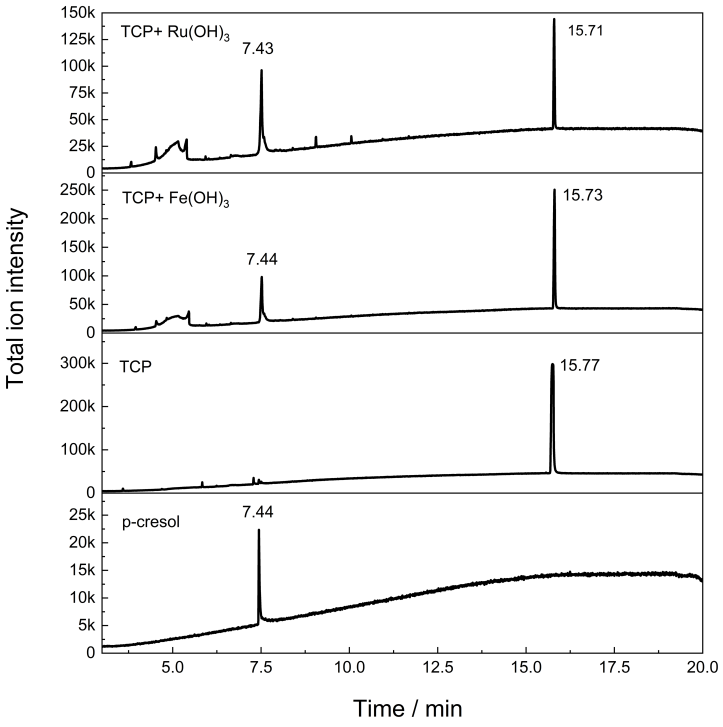


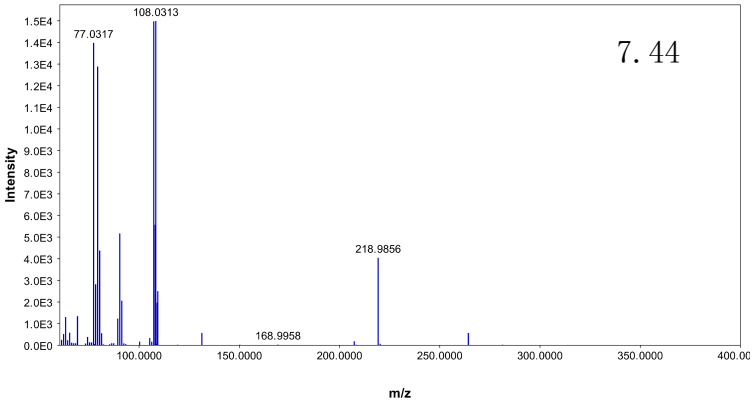

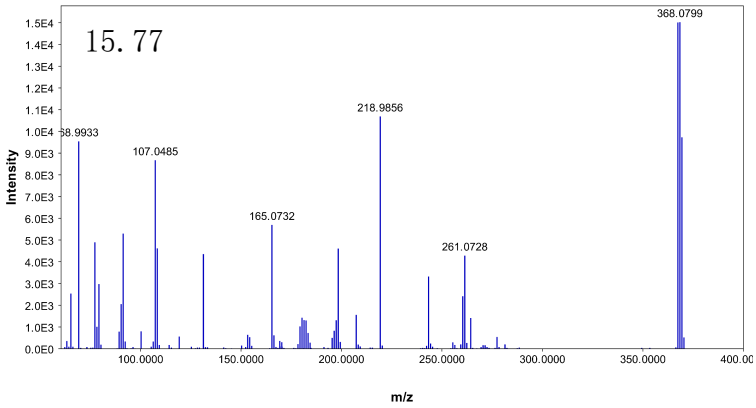


Figure 7.5 GC-MS results for 1mM cresols, 5mM TCP , and its solution after 20 min reaction with $Ru(OH)_3$ and $Fe(OH)_3$ in alcoholysis 75% acetone/ 25% $H_2O$

Followed by the demonstration of catalytic alcoholysis of TCP, its catalytic hydrolysis is also investigated as shown in Fig 7.5. Acetone was used as an alternate of the cosolvent methanol. Fig. shows that, in the presence of Ru(OH)3 and Fe(OH)3, cresols at retention time of 7.4 min were detected. This proves that $Ru(OH)_3$ and $Fe(OH)_3$ are able to catalyze not only the alcoholysis but also the hydrolysis of TCP.

## 7.4 Conclusions

Ru (III) hydroxide and Fe (III) hydroxide were found potentially playing a role as catalysts on decomposition of TCPs via either alcoholysis or hydrolysis. By contrast, Cu (II), Co (II), Mn (II) hydroxide did not display the same effect. The generation of cresols were first validated by the appearance of a peak at 298 nm in UV-VIS spectroscopy, which is the characteristic absorbance peak for cresols. It indicated a alcoholysis rate as high as 16% and 10% for Ru (III), and Fe (III) hydroxide, respectively. The cresols were also able to be detected using Folin-Denis reaction, which only reacts with phenols. This colorimetry indicated a alcoholysis rate as high as 26% and 14% for Ru (III), and Fe (III) hydroxide, respectively, which was higher than the values obtained from UV-VIS. The resultant was analyzed by GC-MS, which further proves the products of alcoholysis of TCP. In addition, the catalytic capability of Ru (III), and Fe (III) hydroxide for the hydrolysis of TCP are demonstrated.

Based on the results observed above, the reaction occurring is proposed as:

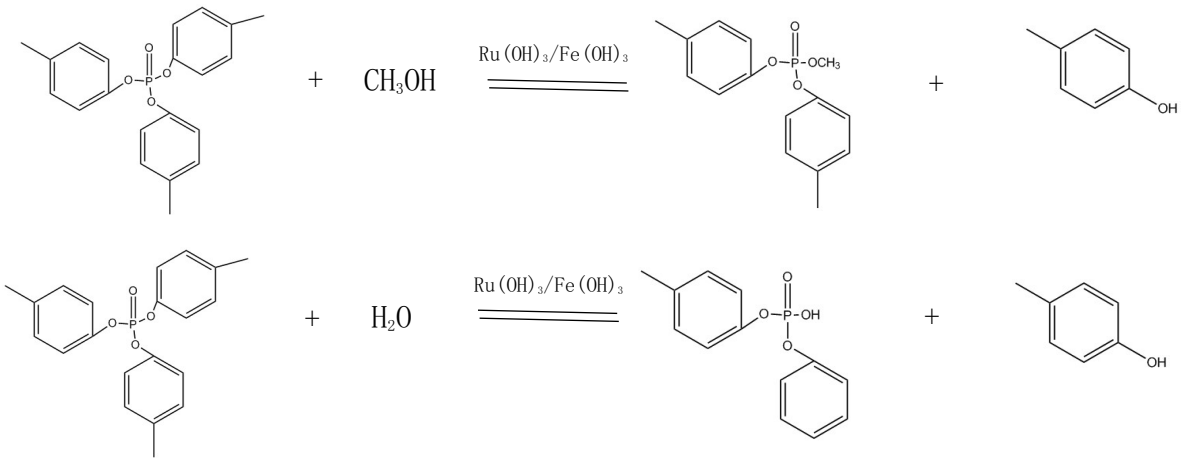

## 8. Overall conclusions

The exposure to toxic chemicals poses severe health risks. The unawareness of the exposure exacerbates the incidence. To assess the exposure, we explored on in-situ monitoring of a neurotoxin in environment, and detection of exposure-sensitive biomarker in blood.

To facilitate the development of biosensors for the biomarkers, and figure out the events and mechanism occurring on the functional interfaces, a Multi-Parametric and Multimodal Spectroscopy (MPMS) analytical system was developed that employs simultaneous and noninterfering measurements of SPR, Light Excited Fluorescence, Surface Plasmon Fluorescence, and three-electrode electrochemistry. The various information gained by combining different spectroscopic methods verified and complemented one another advantageously and provided comprehensive, concise and easy-to-interpret results.

In particular, the system operation was demonstrated by simplified ECPA. Using the sequential mode, it was investigated that the assembly of MB/Quasar-DNA strand resulted in significant synchronous increase of SPR angle, Surface Plasmon/Light Excited fluorescence intensity and characteristic peak current as much as 0.07°, 105 counts (Light Excited Fluorescence), 873 counts (Surface Plasmon Fluorescence), and 26.7 μA respectively. Using the simultaneous mode, the assembly kinetics of MB/Quasar-DNA were also measured and cross-validated by SPR/SPF/Electrochemistry. The linear growth of MB/Quasar-DNA was demonstrated by the increase rate of 3.25 mdeg./ min via SPR, 0.3 μA/min via electrochemical measurement and 3.84 counts/min via fluorescence signal. During the investigation, SPR generated signals upon assembly of each component, Light Excited and Surface Plasmon fluorescence changed only upon assembly of fluorophore-labeled pieces, while the characteristic electrochemical signal was only detected when MB-labeled DNA was assembled. With this system, all steps of interface functionalization dynamics and target recognition can be studied. Which combination of these methods to use in each particular case depends on the objectives of the particular investigation. Combining these techniques together, the MPMS system will improve our fundamental understanding of the dynamics in the formation of biointerfaces and overcome several key limitations of current, widely-used, surface characterization technologies.

In the study of detection of PDGF-BB, the cations present in the buffer solution played vital role in oligonucleotide hybridization efficiency, aptamer-protein interaction and background signals. Higher cation caused higher hybridization efficiency between oligonucleotides, as well as the background signals due to the hydridization between SH-DNA and MB-DNA. In the presence of below 64 mM $MgCl_2$, the affinity between aptamer-protein increased along with the concentrations of $MgCl_2$; above this range, the affinity decreased. As G5 SH-DNA was used, proper experimental conditions could not be found for quantitation of PDGF. As G7 SH-DNA was used instead, a buffer containing 10mM PBS, 276mM NaCl, 5.4mM KCl, 2mM $MgCl_2$ , pH 7.4, displayed proper environment for both oligonucleotide hybridization and aptamer/protein interaction, generating linear current responses with the PDGF concentrations. The success of using G7 SH-DNA also indicated that in high cationic environment, only one molecule of aptamer is able to bind with one molecule of PDGF-BB.

To improve the sampling/electrochemical system for the detection of gaseous TCP, a reusable catalytic alumina column was used. The operational parameters were optimized. This TCP detection system has a sensitivity of 3.6 nA/ ppb and limit of detection of 216 ppb.

Through the validation of results from different detection methods, $Ru(OH)_3$ and $Fe(OH)_3$ are proposed to be capable of efficiently catalyzing the alcoholysis and hydrolysis of TCP, producing cresols at room temperature.

## References


(1) International Labour Organization. *Background Information for Developing an ILO Policy Framework for Hazardous Substances*; Geneva, 2007.

(2) Organisation for Economic Co-operation and Development. *OECD Environmental Outlook for the Chemicals Industry.*; OECD Environmental Outlook; OECD: Paris, 2001.

(3) United Nations Children's Fund. *Understanding the Impacts of Pesticides on Children*; 2018.

(4) Morgan, J. P.; Penovich, P. Jamaica Ginger Paralysis. Forty-Seven-Year Follow-Up. *Arch. Neurol.* **1978**, *35*, 530–532.

(5) Baker, P. E.; Cole, T. B.; Cartwright, M.; Suzuki, S. M.; Thummel, K. E.; Lin, Y. S.; Co, A. L.; Rettie, A. E.; Kim, J. H.; Furlong, C. E. Identifying Safer Anti-Wear Triaryl Phosphate Additives for Jet Engine Lubricants. *Chem. Biol. Interact.* **2013**, *203*, 257–264.

(6) IPCS. *International Programme on Chemical, Environmental Health Criteria 110. Tricresylphosphate*; World Health Organization, 1990.

(7) Winder, C.; Michaelis, S. Crew Effects from Toxic Exposures on Aircraft. In *Air Quality in Airplane Cabins and Similar Enclosed Spaces*; Springer-Verlag: Berlin/Heidelberg; pp 229–248.

(8) Crump, D.; Harrison, P.; Walton, C. Aircraft Cabin Air Sampling Study: Part 1 of the Final Report. **2011**.

(9) Habboush, A. E.; Farroha, S. M.; Khalaf, H. I. Extraction-Gas Chromatographic Method for the Determination of Organophosphorus Compounds as Lubricating Oil Additives. *J. Chromatogr. A* **1995**, *696*, 257–263.

(10) Mutsuga, M.; Kawamura, Y.; Watanabe, Y.; Maitani, T. Determination Method of Tricresyl Phosphate in Polyvinyl Chloride. *Shokuhin Eiseigaku Zasshi.* **2003**, *44*, 26–31.

(11) Denola, G.; Hanhela, P. J.; Mazurek, W. Determination of Tricresyl Phosphate Air Contamination in Aircraft. *Ann. Occup. Hyg.* **2011**, *55*, 710–722.

(12) Snyder, D. T.; Pulliam, C. J.; Ouyang, Z.; Cooks, R. G. Miniature and Fieldable Mass Spectrometers: Recent Advances. *Anal. Chem.* **2016**, *88*, 2–29.

(13) Gilliland, W. M.; Mellors, J. S.; Ramsey, J. M. Coupling Microchip Electrospray Ionization Devices with High Pressure Mass Spectrometry. *Anal. Chem.* **2017**, *89*, 13320–13325.

(14) Bu, X.; Regalado, E. L.; Hamilton, S. E.; Welch, C. J. The Emergence of Low-Cost Compact Mass Spectrometry Detectors for Chromatographic Analysis. *TrAC Trends Anal. Chem.* **2016**, *82*, 22–34.

(15) Mäkinen, M. A.; Anttalainen, O. A.; Sillanpää, M. E. T. Ion Mobility Spectrometry and Its Applications in Detection of Chemical Warfare Agents. *Anal. Chem.* **2010**, *82*, 9594–9600.

(16) Hill, H. H.; Simpson, G. Capabilities and Limitations of Ion Mobility Spectrometry for Field Screening Applications. *F. Anal. Chem. Technol.* **1997**, *1*, 119–134.

(17) Belatik, A.; Hotchandani, S.; Carpentier, R.; Tajmir-Riahi, H.-A.; Gerber, P. Locating the Binding Sites of Pb(II) Ion with Human and Bovine Serum Albumins. *PLoS One* **2012**, *7*, e36723.

(18) Lashkor, M.; Rawson, F. J.; Preece, J. A.; Mendes, P. M. Switching Specific Biomolecular Interactions on Surfaces under Complex Biological Conditions. *Analyst* **2014**, *139*, 5400–5408.

(19) Makarova, A. A.; Grachova, E. V; Neudachina, V. S.; Yashina, L. V; Blüher, A.; Molodtsov, S. L.; Mertig, M.; Ehrlich, H.; Adamchuk, V. K.; Laubschat, C.; et al. Insight into Bio-Metal Interface Formation in Vacuo: Interplay of S-Layer Protein with Copper and Iron. *Sci. Rep.* **2015**, *5*, 8710.

(20) McArthur, S. L.; Mishra, G.; Easton, C. D. Applications of XPS in Biology and Biointerface Analysis. In *Surface Analysis and Techniques in Biology*; Springer International Publishing: Cham, 2014; pp 9–36.

(21) Shen, G.; Anand, M. F. G.; Levicky, R. X-Ray Photoelectron Spectroscopy and Infrared Spectroscopy Study of Maleimide-Activated Supports for Immobilization of Oligodeoxyribonucleotides. *Nucleic Acids Res.* **2004**, *32*, 5973–5980.

(22) Korin, E.; Froumin, N.; Cohen, S. Surface Analysis of Nanocomplexes by X-Ray Photoelectron Spectroscopy (XPS). *ACS Biomater. Sci. Eng.* **2017**, *3*, 882–889.

(23) Zapien, D. C.; Gui, J. Y.; Stern, D. A.; Hubbard, A. T. Surface Electrochemistry and Molecular Orientation: Studies of Pyridyl Hydroquinones Adsorbed at Pt(111) by Cyclic Voltammetry, Auger Electron Spectroscopy and Electron Energy Loss Spectroscopy. *J. Electroanal. Chem.* **1992**, *330*, 469–487.

(24) Ong, J. L.; Lucas, L. C. Auger Electron Spectroscopy and Its Use for the Characterization of Titanium and Hydroxyapatite Surfaces. *Biomaterials* **1998**, *19*, 455–464.

(25) Eberle, A. L.; Mikula, S.; Schalek, R.; Lichtman, J.; Knothe Tate, M. L.; Zeidler, D. High-Resolution, High-Throughput Imaging with a Multibeam Scanning Electron Microscope. *J. Microsc.* **2015**, *259*, 114–120.

(26) *Biological Low-Voltage Scanning Electron Microscopy*; Schatten, H., Pawley, J. B., Eds.; Springer New York: New York, NY, 2008.

(27) Rivière, J. C. *Handbook of Surface and Interface Analysis: Methods for Problem-Solving*; CRC Press, 2009.

(28) Mol, N. J. de.; Fischer, M. J. E. *Surface Plasmon Resonance : Methods and Protocols*; Humana Press:Totowa, NJ, 2010.

(29) Canoa, P.; Simón-Vázquez, R.; Popplewell, J.; González-Fernández, Á. A Quantitative Binding Study of Fibrinogen and Human Serum Albumin to Metal Oxide Nanoparticles by Surface Plasmon Resonance. *Biosens. Bioelectron.* **2015**, *74*, 376–383.

(30) Willets, K. A.; Van Duyne, R. P. Localized Surface Plasmon Resonance Spectroscopy and Sensing. *Annu. Rev. Phys. Chem.* **2007**, *58*, 267–297.

(31) Schasfoort, R. *Handbook of Surface Plasmon Resonance*; Royal Society of Chemistry: Cambridge, 2017.

(32) Homola, J. Surface Plasmon Resonance Sensors for Detection of Chemical and Biological Species. *Chem. Rev.* **2008**, *108*, 462–493.

(33) Pelossof, G.; Tel-Vered, R.; Willner, I. Amplified Surface Plasmon Resonance and Electrochemical Detection of $Pb^{2+}$ Ions Using the $Pb^{2+}$ -Dependent DNAzyme and Hemin/G-Quadruplex as a Label. *Anal. Chem.* **2012**, *84*, 3703–3709.

(34) Maalouf, R.; Fournier-Wirth, C.; Coste, J.; Hanna Chebib; Saïkali, Y.; Vittori, O.; Errachid, A.; Jean-Pierre Cloarec; Martelet, C.; Jaffrezic-Renault, N. Label-Free Detection of Bacteria by Electrochemical Impedance Spectroscopy: Comparison to Surface Plasmon Resonance. *Anal. Chem.* **2007**, *79*, 4879–4886.

(35) Arima, Y.; Teramura, Y.; Takiguchi, H.; Kawano, K.; Kotera, H.; Iwata, H. Surface Plasmon Resonance and Surface Plasmon Field-Enhanced Fluorescence Spectroscopy for Sensitive Detection of Tumor Markers. In *Biosensors and Biodetection*; Humana Press:Totowa, NJ, 2009; pp 3–20.

(36) Roy, S.; Kim, J.-H.; James T. Kellis, J.; Poulose, A. J.; Robertson, C. R.; Gast, A. P. Surface Plasmon Resonance/Surface Plasmon Enhanced Fluorescence: An Optical Technique for the Detection of Multicomponent Macromolecular Adsorption at the Solid/Liquid Interface. *Langmuir* **2002**, *18*, 6319–6323.

(37) Pishko, M. V.; Revzin, A.; Simonian, A. L. Mass Transfer in Amperometric Biosensors Based on Nanocomposite Thin Films of Redox Polymers and Oxidoreductases. *Sensors* **2002**, *2*, 79–90.

(38) Simonian, A. L.; Revzin, A.; Wild, J. R.; Elkind, J.; Pishko, M. V. Characterization of Oxidoreductase–Redox Polymer Electrostatic Film Assembly on Gold by Surface Plasmon Resonance Spectroscopy and Fourier Transform Infrared–External Reflection Spectroscopy. *Anal. Chim. Acta* **2002**, *466*, 201–212.

(39) Zhang, Y.; Arugula, M. A.; Kirsch, J. S.; Yang, X.; Olsen, E.; Simonian, A. L. Layer-by-Layer Assembled Carbon Nanotube-Acetylcholinesterase/Biopolymer Renewable Interfaces: SPR and Electrochemical Characterization. *Langmuir* **2015**, *31*, 1462–1468.

(40) Tawa, K.; Cui, X.; Kintaka, K.; Nishii, J.; Morigaki, K. Sensitive Bioimaging in Microfluidic Channels on the Plasmonic Substrate: Application of an Enhanced Fluorescence Based on the Reverse Coupling Mode. *J. Photochem. Photobiol. A Chem.* **2011**, *221*, 261–267.

(41) Liebermann, T.; Knoll, W. Surface-Plasmon Field-Enhanced Fluorescence Spectroscopy. *Colloids Surfaces A Physicochem. Eng. Asp.* **2000**, *171*, 115–130.

(42) Zhang, J.; Fu, Y.; Chowdhury, M. H.; Lakowicz, J. R. Enhanced Förster Resonance Energy Transfer on Single Metal Particle. 2. Dependence on Donor-Acceptor Separation Distance, Particle Size, and Distance from Metal Surface. *J. Phys. Chem. C. Nanomater. Interfaces* **2007**, *111*, 11784–11792.

(43) Hussain, S. A.; Chakraborty, S. Organoclay Hybrid Films With Improved Functionality. *Clay-Polymer Nanocomposites* **2017**, 273–305.

(44) Yao, D.; Yu, F.; Kim, J.; Scholz, J.; Nielsen, P. E.; Sinner, E.-K.; Knoll, W. Surface Plasmon Field-Enhanced Fluorescence Spectroscopy in PCR Product Analysis by Peptide Nucleic Acid Probes. *Nucleic Acids Res.* **2004**, *32*, e177–e177.

(45) Robelek, R.; Niu, L.; Schmid, E. L.; Knoll, W. Multiplexed Hybridization Detection of Quantum Dot-Conjugated DNA Sequences Using Surface Plasmon Enhanced Fluorescence Microscopy and Spectrometry. *Anal. Chem.* **2004**, *76*, 6160–6165.

(46) Yokota, H.; Saito, K.; Yanagida, T. Single Molecule Imaging of Fluorescently Labeled Proteins on Metal by Surface Plasmons in Aqueous Solution. *Phys. Rev. Lett.* **1998**, *80*, 4606–4609.

(47) Bauch, M.; Toma, K.; Toma, M.; Zhang, Q.; Dostalek, J. Plasmon-Enhanced Fluorescence Biosensors: A Review. *Plasmonics* **2014**, *9*, 781–799.

(48) Dostálek, J.; Kasry, A.; Knoll, W. Long Range Surface Plasmons for Observation of Biomolecular Binding Events at Metallic Surfaces. *Plasmonics* **2007**, *2*, 97–106.

(49) Huang, C. J.; Dostalek, J.; Knoll, W. Optimization of Layer Structure Supporting Long Range Surface Plasmons for Surface Plasmon-Enhanced Fluorescence Spectroscopy Biosensors. *J. Vac. Sci. Technol. B, Nanotechnol. Microelectron. Mater. Process. Meas. Phenom.* **2010**, *28*, 66–72.

(50) Tawa, K.; Cui, X.; Kintaka, K.; Nishii, J.; Morigaki, K. Sensitive Bioimaging in Microfluidic Channels on the Plasmonic Substrate: Application of an Enhanced Fluorescence Based on the Reverse Coupling Mode. *J. Photochem. Photobiol. A Chem.* **2011**, *221*, 261–267.

(51) Tawa, K.; Hori, H.; Kintaka, K.; Kiyosue, K.; Tatsu, Y.; Nishii, J. Optical Microscopic Observation of Fluorescence Enhanced by Grating-Coupled Surface Plasmon Resonance. *Opt. Express* **2008**, *16*, 9781.

(52) Hwang, E.; Smolyaninov, I. I.; Davis, C. C. Surface Plasmon Polariton Enhanced Fluorescence from Quantum Dots on Nanostructured Metal Surfaces. *Nano Lett.* **2010**, *10*, 813–820.

(53) Aroca, R.; Kovacs, G. J.; Jennings, C. A.; Loutfy, R. O.; Vincett, P. S. Fluorescence Enhancement from Langmuir-Blodgett Monolayers on Silver Island Films. *Langmuir* **1988**, *4*, 518–521.

(54) Matveeva, E. G.; Gryczynski, Z.; Lakowicz, J. R. Myoglobin Immunoassay Based on Metal Particle-Enhanced Fluorescence. *J. Immunol. Methods* **2005**, *302*, 26–35.

(55) Lakowicz, J. R. Radiative Decay Engineering 5: Metal-Enhanced Fluorescence and Plasmon Emission. *Anal. Biochem.* **2005**, *337*, 171–194.

(56) Zhang, W.; Ding, F.; Li, W.-D.; Wang, Y.; Hu, J.; Chou, S. Y. Giant and Uniform Fluorescence Enhancement over Large Areas Using Plasmonic Nanodots in 3D Resonant Cavity Nanoantenna by Nanoimprinting. *Nanotechnology* **2012**, *23*, 225301.

(57) Punj, D.; Mivelle, M.; Moparthi, S. B.; van Zanten, T. S.; Rigneault, H.; van Hulst, N. F.; García-Parajó, M. F.; Wenger, J. A Plasmonic 'Antenna-in-Box' Platform for Enhanced Single-Molecule Analysis at Micromolar Concentrations. *Nat. Nanotechnol.* **2013**, *8*, 512–516.

(58) Schmelzeisen, M.; Zhao, Y.; Klapper, M.; Müllen, K.; Kreiter, M. Fluorescence Enhancement from Individual Plasmonic Gap Resonances. *ACS Nano* **2010**, *4*, 3309–3317.

(59) Fu, Y.; Zhang, J.; Lakowicz, J. R.; Matsushige, K.; Makino, K.; Cobley, C. M.; Xia, Y. N. Large Enhancement of Single Molecule Fluorescence by Coupling to Hollow Silver Nanoshells. *Chem. Commun.* **2012**, *48*, 9726.

(60) Mei, Z.; Tang, L. Surface-Plasmon-Coupled Fluorescence Enhancement Based on Ordered Gold Nanorod Array Biochip for Ultrasensitive DNA Analysis. *Anal. Chem.* **2017**, *89*, 633–639.

(61) Kambhampati, D.; Nielsen, P. E.; Knoll, W. Investigating the Kinetics of DNA–DNA and PNA–DNA Interactions Using Surface Plasmon Resonance-Enhanced Fluorescence Spectroscopy. *Biosens. Bioelectron.* **2001**, *16*, 1109–1118.

(62) Zhou, C.; Duan, X.; Liu, N. A Plasmonic Nanorod That Walks on DNA Origami. *Nat. Commun.* **2015**, *6*, 8102.

(63) Peng, H.-I.; Strohsahl, C. M.; Leach, K. E.; Krauss, T. D.; Miller, B. L. Label-Free DNA Detection on Nanostructured Ag Surfaces. *ACS Nano* **2009**, *3*, 2265–2273.

(64) Singh, V.; Nerimetla, R.; Yang, M.; Krishnan, S. Magnetite-Quantum Dot Immunoarray for Plasmon-Coupled-Fluorescence Imaging of Blood Insulin and Glycated Hemoglobin. *ACS Sensors* **2017**, *2*, 909–915.

(65) Scholten, A.; Menges, B.; Juebner, M.; Rothschild, M. A.; Bender, K. A Mixed Alkanethiol Based Immunosensor for Surface Plasmon Field-Enhanced Fluorescence Spectroscopy in Serum. *Analyst* **2013**, *138*, 1705.

(66) Chang, Y.-F.; Yu, J.-S.; Chang, Y.-T.; Su, L.-C.; Wu, C.-C.; Chang, Y.-S.; Lai, C.-S.; Chou, C. The Utility of a High-Throughput Scanning Biosensor in the Detection of the Pancreatic Cancer Marker ULBP2. *Biosens. Bioelectron.* **2013**, *41*, 232–237.

(67) Dragan, A. I.; Albrecht, M. T.; Pavlovic, R.; Keane-Myers, A. M.; Geddes, C. D. Ultra-Fast Pg/Ml Anthrax Toxin (Protective Antigen) Detection Assay Based on Microwave-Accelerated Metal-Enhanced Fluorescence. *Anal. Biochem.* **2012**, *425*, 54–61.

(68) Dostálek, J.; Knoll, W. Biosensors Based on Surface Plasmon-Enhanced Fluorescence Spectroscopy (Review). *Biointerphases* **2008**, *3*, FD12-FD13.

(69) Hong, B.; Sun, A.; Pang, L.; Venkatesh, A. G.; Hall, D.; Fainman, Y. Integration of Faradaic Electrochemical Impedance Spectroscopy into a Scalable Surface Plasmon Biosensor for in Tandem Detection. *Opt. Express* **2015**, *23*, 30237–30249.

(70) Liu, J.; Tian, S.; Tiefenauer, L.; Nielsen, P. E.; Knoll, W. Simultaneously Amplified Electrochemical and Surface Plasmon Optical Detection of DNA Hybridization Based on Ferrocene-Streptavidin Conjugates.

(71) Balasubramanian, S.; Revzin, A.; Simonian, A. Electrochemical Desorption of Proteins from Gold Electrode Surface. *Electroanalysis* **2006**, *18*, 1885–1892.

(72) Vandenryt, T.; Pohl, A.; van Grinsven, B.; Thoelen, R.; De Ceuninck, W.; Wagner, P.; Opitz, J. Combining Electrochemical Impedance Spectroscopy and Surface Plasmon Resonance into One Simultaneous Read-out System for the Detection of Surface Interactions. *Sensors (Basel).* **2013**, *13*, 14650–14661.

(73) Andrae, J.; Gallini, R.; Betsholtz, C. Role of Platelet-Derived Growth Factors in Physiology and Medicine. *Genes Dev.* **2008**, *22*, 1276–1312.

(74) Stayner, L.; Welch, L. S.; Lemen, R. The Worldwide Pandemic of Asbestos-Related Diseases. *Annu. Rev. Public Health* **2013**, *34*, 205–216.

(75) Driscoll, T.; Nelson, D. I.; Steenland, K.; Leigh, J.; Concha-Barrientos, M.; Fingerhut, M.; Prüss-Üstün, A. The Global Burden of Disease Due to Occupational Carcinogens. *Am. J. Ind. Med.* **2005**, *48*, 419–431.

(76) Perkins, T. N.; Shukla, A.; Peeters, P. M.; Steinbacher, J. L.; Landry, C. C.; Lathrop, S. A.; Steele, C.; Reynaert, N. L.; Wouters, E. F. M.; Mossman, B. T. Differences in Gene Expression and Cytokine Production by Crystalline vs. Amorphous Silica in Human Lung Epithelial Cells. *Part. Fibre Toxicol.* **2012**, *9*, 6.

(77) Poinen-Rughooputh, S.; Rughooputh, M. S.; Guo, Y.; Rong, Y.; Chen, W. Occupational Exposure to Silica Dust and Risk of Lung Cancer: An Updated Meta-Analysis of Epidemiological Studies. *BMC Public Health* **2016**, *16*, 1137.

(78) Lo Re, S.; Lecocq, M.; Uwambayinema, F.; Yakoub, Y.; Delos, M.; Demoulin, J.-B.; Lucas, S.; Sparwasser, T.; Renauld, J.-C.; Lison, D.; et al. Platelet-Derived Growth Factor–Producing CD4 + Foxp3+ Regulatory T Lymphocytes Promote Lung Fibrosis. *Am. J. Respir. Crit. Care Med.* **2011**, *184*, 1270–1281.

(79) Zhou, J.; Deng, Y.; Yan, L.; Zhao, H.; Wang, G. Serum Platelet-Derived Growth Factor BB Levels: A Potential Biomarker for the Assessment of Liver Fibrosis in Patients with Chronic Hepatitis B. *Int. J. Infect. Dis.* **2016**, *49*, 94–99.

(80) Brandt-Rauf, P. W.; Smith, S.; Hemminki, K.; Koskinen, H.; Vainio, H.; Niman, H.; Ford, J. Serum Oncoproteins and Growth Factors in Asbestosis and Silicosis Patients. *Int. J. Cancer* **1992**, *50*, 881–885.

(81) Takayama, H.; Miyake, Y.; Nouso, K.; Ikeda, F.; Shiraha, H.; Takaki, A.; Kobashi, H.; Yamamoto, K. Serum Levels of Platelet-Derived Growth Factor-BB and Vascular Endothelial Growth Factor as Prognostic Factors for Patients with Fulminant Hepatic Failure. *J. Gastroenterol. Hepatol.* **2011**, *26*, 116–121.

(82) Zhang, H.; Li, F.; Chen, H.; Ma, Y.; Qi, S.; Chen, X.; Zhou, L. AuNPs Colorimetric Sensor for Detecting Platelet-Derived Growth Factor-BB Based on Isothermal Target-Triggering Strand Displacement Amplification. *Sensors Actuators B Chem.* **2015**, *207*, 748–755.

(83) Li, H.; Zhu, Y.; Dong, S.; Qiang, W.; Sun, L.; Xu, D. Fast Functionalization of Silver Decahedral Nanoparticles with Aptamers for Colorimetric Detection of Human Platelet-Derived Growth Factor-BB. *Anal. Chim. Acta* **2014**, *829*, 48–53.

(84) Ma, X.; Chen, Z.; Zhou, J.; Weng, W.; Zheng, O.; Lin, Z.; Guo, L.; Qiu, B.; Chen, G. Aptamer-Based Portable Biosensor for Platelet-Derived Growth Factor-BB (PDGF-BB) with Personal Glucose Meter Readout. *Biosens. Bioelectron.* **2014**, *55*, 412–416.

(85) Wang, P.; Song, Y.; Zhao, Y.; Fan, A. Hydroxylamine Amplified Gold Nanoparticle-Based Aptameric System for the Highly Selective and Sensitive Detection of Platelet-Derived Growth Factor. *Talanta* **2013**, *103*, 392–397.

(86) Wang, C.-W.; Chang, H.-T. Sensitive Detection of Platelet-Derived Growth Factor through Surface-Enhanced Raman Scattering. *Anal. Chem.* **2014**, *86*, 7606–7611.

(87) Ye, S.; Zhai, X.; Wu, Y.; Kuang, S. Dual-Primer Self-Generation SERS Signal Amplification Assay for PDGF-BB Using Label-Free Aptamer. *Biosens. Bioelectron.* **2016**, *79*, 130–135.

(88) Fredriksson, S.; Gullberg, M.; Jarvius, J.; Olsson, C.; Pietras, K.; Gústafsdóttir, S. M.; Östman, A.; Landegren, U. Protein Detection Using Proximity-Dependent DNA Ligation Assays. *Nat. Biotechnol.* **2002**, *20*, 473–477.

(89) Babu, E.; Singaravadivel, S.; Manojkumar, P.; Krishnasamy, S.; Gnana kumar, G.; Rajagopal, S. Aptamer-Based Label-Free Detection of PDGF Using Ruthenium(II) Complex as Luminescent Probe. *Anal. Bioanal. Chem.* **2013**, *405*, 6891–6895.

(90) Liang, J.; Wei, R.; He, S.; Liu, Y.; Guo, L.; Li, L. A Highly Sensitive and Selective Aptasensor Based on Graphene Oxide Fluorescence Resonance Energy Transfer for the Rapid Determination of Oncoprotein PDGF-BB. *Analyst* **2013**, *138*, 1726.

(91) Gersuk, G. M.; Carmel, R.; Pattengale, P. K. Platelet-Derived Growth Factor Concentrations in Platelet-Poor Plasma and Urine from Patients with Myeloproliferative Disorders. *Blood* **1989**, *74*, 2330–2334.

(92) Yu, Y.; Su, G.; Zhu, H.; Zhu, Q.; Chen, Y.; Xu, B.; Li, Y.; Zhang, W. Proximity Hybridization-Mediated Isothermal Exponential Amplification for Ultrasensitive Electrochemical Protein Detection. *Int. J. Nanomedicine* **2017**, *Volume 12*, 5903–5914.

(93) Huang, K.-J.; Liu, Y.-J.; Zhai, Q.-F. Ultrasensitive Biosensing Platform Based on Layered Vanadium Disulfide–Graphene Composites Coupling with Tetrahedron-Structured DNA Probes and Exonuclease III Assisted Signal Amplification. *J. Mater. Chem. B* **2015**, *3*, 8180–8187.

(94) Song, W.; Li, H.; Liang, H.; Qiang, W.; Xu, D. Disposable Electrochemical Aptasensor Array by Using in Situ DNA Hybridization Inducing Silver Nanoparticles Aggregate for Signal Amplification. *Anal. Chem.* **2014**, *86*, 2775–2783.

(95) Stojek, M.; Adrych, K.; Rojek, L.; Smoczynski, M.; Sledzinski, T.; Szrok, S.; Swierczynski, J. Decreased Serum Platelet Derived Growth Factor BB Levels in Acute and Increased in Chronic Pancreatitis. *World J. Gastroenterol.* **2014**, *20*, 13127.

(96) Kajizuka, M.; Miyachi, T.; Matsuzaki, H.; Iwata, K.; Shinmura, C.; Suzuki, K.; Suda, S.; Tsuchiya, K. J.; Matsumoto, K.; Iwata, Y.; et al. Serum Levels of Platelet-Derived Growth Factor BB Homodimers Are Increased in Male Children with Autism. *Prog. Neuro-Psychopharmacology Biol. Psychiatry* **2010**, *34*, 154–158.

(97) Hu, J.; Wang, T.; Kim, J.; Shannon, C.; Easley, C. J. Quantitation of Femtomolar Protein Levels via Direct Readout with the Electrochemical Proximity Assay. *J. Am. Chem. Soc.* **2012**, *134*, 7066–7072.

(98) Hu, J.; Yu, Y.; Brooks, J. C.; Godwin, L. A.; Somasundaram, S.; Torabinejad, F.; Kim, J.; Shannon, C.; Easley, C. J. A Reusable Electrochemical Proximity Assay for Highly Selective, Real-Time Protein Quantitation in Biological Matrices. *J. Am. Chem. Soc.* **2014**, *136*, 8467–8474.

(99) Ren, K.; Wu, J.; Yan, F.; Ju, H. Ratiometric Electrochemical Proximity Assay for Sensitive One-Step Protein Detection. *Sci. Rep.* **2015**, *4*, 4360.

(100) Wen, G.; Ju, H. Enhanced Photoelectrochemical Proximity Assay for Highly Selective Protein Detection in Biological Matrixes. *Anal. Chem.* **2016**, *88*, 8339–8345.

(101) Wang, Q.; Gan, X.; Zang, R.; Chai, Y.; Yuan, Y.; Yuan, R. An Amplified Electrochemical Proximity Immunoassay for the Total Protein of Nosema Bombycis Based on the Catalytic Activity of Fe3O4NPs towards Methylene Blue. *Biosens. Bioelectron.* **2016**, *81*, 382–387.

(102) Crulhas, B. P.; Hadley, D.; Liu, Y.; Shin, D.-S.; Stybayeva, G.; Imanbekova, M.; Hill, A. E.; Pedrosa, V.; Revzin, A. An Electrochemical Aptasensor for Detection of Bovine Interferon Gamma. *Anal. Methods* **2017**, *9*, 4527–4532.

(103) Tuleuova, N.; Jones, C. N.; Yan, J.; Ramanculov, E.; Yokobayashi, Y.; Revzin, A. Development of an Aptamer Beacon for Detection of Interferon-Gamma. *Anal. Chem.* **2010**, *82*, 1851–1857.

(104) Arugula, M. A.; Simonian, A. Novel Trends in Affinity Biosensors: Current Challenges and Perspectives. *Meas. Sci. Technol.* **2014**, *25*, 032001.

(105) Baszkin, A.; Norde, W. *Physical Chemistry of Biological Interfaces*; M. Dekker, 2000.

(106) Ying, P.; Viana, A. S.; Abrantes, L. M.; Jin, G. Adsorption of Human Serum Albumin onto Gold: A Combined Electrochemical and Ellipsometric Study. *J. Colloid Interface Sci.* **2004**, *279*, 95–99.

(107) Yan-Yeung Luk; Matthew L. Tingey; David J. Hall; Barbara A. Israel; Christopher J. Murphy; Paul J. Bertics; Nicholas L. Abbott. Using Liquid Crystals to Amplify Protein−Receptor Interactions: Design of Surfaces with Nanometer-Scale Topography That Present Histidine-Tagged Protein Receptors†. **2003**, *19*, 1671–1680.

(108) Liu, X.; Zheng, F.; Jürgensen, A.; Perez-Dieste, V.; Petrovykh, D. Y.; Abbott, N. L.; Himpsel, F. J. Self-Assembly of Biomolecules at Surfaces Characterized by NEXAFS. *Can. J. Chem.* **2007**, *85*, 793–800.

(109) Roach, P.; Farrar, D.; Perry, C. C. Interpretation of Protein Adsorption: Surface-Induced Conformational Changes. *J. Am. Chem. Soc.* **2005**, *127*, 8168–8173.

(110) Zhang, Y.; Arugula, M. A.; Wales, M.; Wild, J.; Simonian, A. L. A Novel Layer-by-Layer Assembled Multi-Enzyme/CNT Biosensor for Discriminative Detection between Organophosphorus and Non-Organophosphrus Pesticides. *Biosens. Bioelectron.* **2015**, *67*, 287–295.

(111) Liu, Y.; Tuleouva, N.; Ramanculov, E.; Revzin, A. Aptamer-Based Electrochemical Biosensor for Interferon Gamma Detection. *Anal. Chem.* **2010**, *82*, 8131–8136.

(112) Luong, J. H. T.; Male, K. B.; Glennon, J. D. Biosensor Technology: Technology Push versus Market Pull. *Biotechnol. Adv.* **2008**, *26*, 492–500.

(113) Zeng, X.; Andrade, C. A. S.; Oliveira, M. D. L.; Sun, X.-L. Carbohydrate–Protein Interactions and Their Biosensing Applications. *Anal. Bioanal. Chem.* **2012**, *402*, 3161–3176.

(114) Trilling, A. K.; Harmsen, M. M.; Ruigrok, V. J. B.; Zuilhof, H.; Beekwilder, J. The Effect of Uniform Capture Molecule Orientation on Biosensor Sensitivity: Dependence on Analyte Properties. *Biosens. Bioelectron.* **2013**, *40*, 219–226.

(115) Chen, S.; Liu, L.; Zhou, J.; Jiang, S. Controlling Antibody Orientation on Charged Self-Assembled Monolayers. *Langmuir* **2003**, *19*, 2859–2864.

(116) Sota, H.; Hasegawa, Y.; Iwakura, M. Detection of Conformational Changes in an Immobilized Protein Using Surface Plasmon Resonance. *Anal. Chem.* **1998**, *70*, 2019–2024.

(117) Ley, K.; Christofferson, A.; Penna, M.; Winkler, D.; Maclaughlin, S.; Yarovsky, I. Surface-Water Interface Induces Conformational Changes Critical for Protein Adsorption: Implications for Monolayer Formation of EAS Hydrophobin. *Front. Mol. Biosci.* **2015**, *2*, 64.

(118) Nel, A. E.; Mädler, L.; Velegol, D.; Xia, T.; Hoek, E. M. V; Somasundaran, P.; Klaessig, F.; Castranova, V.; Thompson, M. Understanding Biophysicochemical Interactions at the Nano-Bio Interface. *Nat. Mater.* **2009**, *8*, 543–557.

(119) Campbell, A. S.; Dong, C.; Meng, F.; Hardinger, J.; Perhinschi, G.; Wu, N.; Dinu, C. Z. Enzyme Catalytic Efficiency: A Function of Bio-Nano Interface Reactions. *ACS Appl. Mater. Interfaces* **2014**, *6*, 5393–5403.

(120) Cameron, P. J.; Zhong, X.; Knoll, W. Electrochemically Controlled Surface Plasmon Enhanced Fluorescence Response of Surface Immobilized CdZnSe Quantum Dots. *J. Phys. Chem. C* **2009**, *113*, 6003–6008.

(121) Niu, L.; Knoll, W. Electrochemically Addressable Functionalization and Parallel Readout of a DNA Biosensor Array. *Anal. Chem.* **2007**, *79*, 2695–2702.

(122) Hu, J.; Wang, T.; Kim, J.; Shannon, C.; Easley, C. J. Quantitation of Femtomolar Protein Levels via Direct Readout with the Electrochemical Proximity Assay. *J. Am. Chem. Soc.* **2012**, *134*, 7066–7072.

(123) Jung, L. S.; Campbell, C. T.; Chinowsky, T. M.; Mar, M. N.; Yee, S. S. Quantitative Interpretation of the Response of Surface Plasmon Resonance Sensors to Adsorbed Films. *Langmuir* **1998**, *14*, 5636–5648.

(124) Naimushin, A. N.; Soelberg, S. D.; Nguyen, D. K.; Dunlap, L.; Bartholomew, D.; Elkind, J.; Melendez, J.; Furlong, C. E. Detection of Staphylococcus Aureus Enterotoxin B at Femtomolar Levels with a Miniature Integrated Two-Channel Surface Plasmon Resonance (SPR) Sensor. *Biosens. Bioelectron.* **2002**, *17*, 573–584.

(125) Rupert, D. L. M.; Shelke, G. V.; Emilsson, G.; Claudio, V.; Block, S.; Lässer, C.; Dahlin, A.; Lötvall, J. O.; Bally, M.; Zhdanov, V. P.; et al. Dual-Wavelength Surface Plasmon Resonance for Determining the Size and Concentration of Sub-Populations of Extracellular Vesicles. *Anal. Chem.* **2016**, *88*, 9980–9988.

(126) Selim Elhadj; Gaurav Singh, A.; Saraf*, R. F. Optical Properties of an Immobilized DNA Monolayer from 255 to 700 Nm. *Langmuir* **2004**, *20*, 5539–5543.

(127) Alexander W. Peterson; Lauren K. Wolf; Rosina M. Georgiadis. Hybridization of Mismatched or Partially Matched DNA at Surfaces. *J.Am.Chem.Soc.* **2002**, *124*, 14601–14607.

(128) Tani, A.; Thomson, A. J.; Butt, J. N. Methylene Blue as an Electrochemical Discriminator of Single- and Double-Stranded Oligonucleotides Immobilised on Gold Substrates. *Analyst* **2001**, *126*, 1756–1759.

(129) Tichoniuk, M.; Ligaj, M.; Filipiak, M. Application of DNA Hybridization Biosensor as a Screening Method for the Detection of Genetically Modified Food Components. *Sensors* **2008**, *8*, 2118–2135.

(130) Green, L. S.; Jellinek, D.; Jenison, R.; Östman, A.; Heldin, C.-H.; Janjic, N. Inhibitory DNA Ligands to Platelet-Derived Growth Factor B-Chain. *Biochemistry* **1996**, *35*, 14413–14424.

(131) Wang, C.-W.; Chang, H.-T. Sensitive Detection of Platelet-Derived Growth Factor through Surface-Enhanced Raman Scattering. *Anal. Chem.* **2014**, *86*, 7606–7611.

(132) Naimushin, A. N.; Soelberg, S. D.; Nguyen, D. K.; Dunlap, L.; Bartholomew, D.; Elkind, J.; Melendez, J.; Furlong, C. E. Detection of Staphylococcus Aureus Enterotoxin B at Femtomolar Levels with a Miniature Integrated Two-Channel Surface Plasmon Resonance (SPR) Sensor. *Biosens. Bioelectron.* **2002**, *17*, 573–584.

(133) Jung, L. S.; Campbell, C. T.; Chinowsky, T. M.; Mar, M. N.; Yee, S. S. Quantitative Interpretation of the Response of Surface Plasmon Resonance Sensors to Adsorbed Films. *Langmuir* **1998**, *14*, 5636–5648.

(134) Portable and Remote Electrochemical Sensing System for Detection of Tricresyl Phosphate in Gas Phase. *Sensors Actuators B Chem.* **2012**, *161*, 564–569.

(135) Khare, S. D.; Kipnis, Y.; Greisen, P. J.; Takeuchi, R.; Ashani, Y.; Goldsmith, M.; Song, Y.; Gallaher, J. L.; Silman, I.; Leader, H.; et al. Computational Redesign of a Mononuclear Zinc Metalloenzyme for Organophosphate Hydrolysis. *Nat. Chem. Biol.* **2012**, *8*, 294–300.

(136) Saba, C. S.; Forster, N. H. Reactions of Aromatic Phosphate Esters with Metals and Their Oxides. *Tribol. Lett.* **2002**, *12*, 135–146.

(137) Dannenberg; Pehkonen. Investigation of the Heterogeneously Catalyzed Hydrolysis of Organophosphorus Pesticides. *J. Agric. Food Chem.* **1998**, *46*, 325–334.

(138) Mizuno, N.; Yamaguchi, K. Selective Aerobic Oxidations by Supported Ruthenium Hydroxide Catalysts. *Catal. Today* **2008**, *132*, 18–26.